McGill

Department of Mechanical Engineering

Analysis of Shock Dynamics in Supersonic Intakes

BY

Råbi Tahir

A thesis submitted to McGill University
in partial fulfilment of the requirement for
the degree of Doctor of Philosophy.

Montréal, Québec, Canada.

Contents

Acronyms

CAD computer aided design. 44

CCW Chester, Chisnell, and Whitham. 20, 69, 71, 73, 76, 78, 80–82, 85, 89, 94, 95, 97, 100, 102, 107, 108, 112, 113, 120, 125, 130, 133, 219, 222

CFD computational fluid dynamics. 13, 19, 33, 34, 39, 40, 59, 93–95, 97, 142, 186, 187

DRDC Defence R&D Canada. xxii, 24, 27, 41, 44, 47

IoS index of startablity for one-dimensional flow. 7, 9, 26–28

ISS international space station. 2

IVP initial value problem. 89, 94, 117, 120, 121

LEO low earth orbit. 2, 18

SoL shock on lip. 7, 61

SRS strong reflected shock. 26, 28, 30, 31

WRS weak reflected shock. 26, 28, 30, 31, 179

List of Terms

Asterix (as-te-riks), (*noun*). *An existing software package*[1], *which is used here to solve the quasi-one-dimensional Euler equations.* 68, 93, 94, 97, 100, 105, 108, 115, 126, 127, 130, 133, 186, 187, 191, 201, 217

athodyd *A(ero)+TH(erm)+ODY(namic)+D(uct).* xii

design point *Referring to any particular set of conditions, under which certain desired performance characteristics are attained. First example: the internal flow structure may be suitably prescribed (usually based on a "known flow" from ideal gas theory) for a given design free-stream Mach number,* M_D. *Second example: the external wave structure may be designed to reduce or eliminate flow spillage as* $M_\infty \to M_D$, *usually through wave focusing at the cowl lip.* 12, 19, 27

homentropic $s_x = 0$, *constant entropy along all characteristic directions. Care should be exercised in reading older literature (e.g.,*[2]*), where the term isentropic often refers to the special case of homentropic flow.* 86, 87

hypersonic *Much faster than speed of sound.* 1

inlet *Device that captures air mass and compresses it using ram-effect.* xi

intake *See inlet.* 1, 6, 61

isentropic $s_x \neq 0, s_t + us_x = 0$, *particles maintain a constant entropy along the* C_0 *characteristic direction. Care should be exercised in reading older literature where the term isentropic often refers to the special case of homentropic flow. The terms multisentropic (or multhisentropic) also appear in some older literature; these refer to what is here labelled as isentropic flow.* 87, 122

ramjet *A type of jet engine (athodyd) which uses ram effect for compression of air, thus negating the necessity of any major moving components (no compressor or turbine).* *xii, 2*

scramjet *supersonic combustion ramjet.* *2, 3*

List of Symbols

$A(x)$ Geometrical definition; cross-sectional area of the channel; area of the shock wave. 72, 88

A_∞ Free stream capture area. 7, 24, 32, 37, 88, 168

A_i Inlet/entrance area. 7, 25

A_s Sonic area. 28, 32, 37, 163

A_t Throat area. 28, 32, 37, 163, 165, 168

$A_{(d)}$ Local area downstream of a shock wave. 37, 163, 164

$A_{(u)}$ Local area upstream of a shock wave. 163, 164

$A_{\infty,2}$ Stream area upstream of cowl shock wave. 25, 28, 162, 163, 165

A_K Sonic area downstream of a normal shock wave (Kantrowitz area). 28, 32, 37, 163

C_0 Denotes relations which hold along a particle path. 87, 115, 119, 219, 220

$C_\pm$ Denotes relations which hold along the right- and left-running characteristic waves, respectively. 87, 89, 115, 119, 219–221

$J_\pm$ Denotes characteristic variables associated with the right- and left-running characteristic waves, respectively. See Appendix I for further reference. 115, 221

L Length of the intake. 88

M_D Free stream Mach number under design conditions. xi, 24, 31, 37, 40, 161, 163

M_∞ Free stream Mach number. xi, 4, 6, 10, 13, 26, 28, 31, 32, 37, 40, 161–164

M_i Inlet/entrance Mach number. 6

M_s Shock wave Mach number (always > 1). 72, 88

M_t Throat Mach number. 6, 162, 163

$M_{(d)}$ Local Mach number downstream of a shock wave. 37, 38, 163, 164

$M_{(n)}$ Normal component of the local Mach number upstream of a shock wave. 37, 38

$M_{(u)}$ Local Mach number upstream of a shock wave. 36, 163, 164

$M_{\infty,2}$ Mach number upstream of the curved shock wave. 38, 162, 164

α Local inclination of downstream flow, measured positive counter clockwise, relative to the shock wave. 37, 38

β Square of the normal component of upstream Mach number at a shock wave. 36, 164

$\delta(t)$ Local change in flow inclination across a curved shock wave, measured positive counter clockwise. 38

δ_1 Stream deflection across the first shock wave. 38, 163

δ Local change in flow inclination across a shock wave, measured positive counter clockwise. 35, 36

γ Ratio of specific heats (polytropic index). 28, 32, 36, 37, 163, 164

ϕ Parameter determining the type of oblique shock wave; 0 for weak shock waves, 4π for strong shock waves. 163

$\mathrm{IoS}_{\mathrm{act}}$ Index of Startability (actual). 28, 30

$\theta(t)$ Geometric angle for the curved shock wave, measured positive counter clockwise, relative to the x-axis. 38

θ Aerodynamic shock wave angle, measured positive counter clockwise, relative to upstream flow direction. 36, 37, 164

ξ Pressure ratio across a shock wave. 36, 72

c_∞ Speed of sound in the free stream flow. 89

$f(t)$ Body force per unit mass. 88

m_1 Signed value of local flow Mach number upstream of the shock wave. 79, 88

m_2 Signed value of local flow Mach number downstream of the shock wave. 88

m_∞ Signed value of the free stream flow Mach number. 88, 89

t_0 Parametric coordinate (beginning value at the triple point used in integration along curved shock wave). 35, 36

t_1 Parametric coordinate (ending value at the ramp used in integration along curved shock wave). 35

t_s Parametric coordinate (intermediate value at the sonic point used in integration along curved shock wave). 37

t Time. Also, parametric coordinate used in (time-like) integration along curved shock wave. 35, 37, 38

u_s Shock wave speed in the laboratory frame of reference. 88

Abstract

This work investigates fluid mechanical processes involving movement of shock-waves inside channels. In particular, the prediction and control of shock motion in intakes is of great importance to high-speed flight and future spacecraft engines—it is a fundamental problem whose solution currently enjoys a high degree of interest.

In the first part of the thesis, an analytical, numerical, and experimental study is performed in two-dimensions to assess the quasi-steady flow starting characteristics in an external-compression ramp-type intake. Using the popular model based on common understanding in the field and consistent with well-cited literature, it is shown that the traditional model based on one-dimensional flow across a planar shock is inaccurate. To remedy this, a novel analytical model is presented to predict off-design self-starting behaviour using a curved shock wave. The analytical results are supported by the numerical evidence from CFD simulations as well as by the experimental evidence; taken together, these results constitute overwhelming evidence supporting the arguments presented.

In the second part of the thesis, an analytical and numerical study is performed in the unsteady, quasi-one-dimensional setting to assess the feasibility of predicting shock dynamics inside an intake using a simple, approximate, yet representative model. There is very little widely-available knowledge on impulsive flow starting in the literature, and there is no existing theory for analytically predicting impulsive

flow starting phenomena discussed here.

The well-known Chester-Chisnell-Whitham formulation is extended using a novel model (labelled lifting isentrope); it is effectively a provision for non-uniform, unsteady flow upstream of the shock wave. It is found that a singularity exists in the CCW model, which prevents its application to problems in impulsive flow starting. There is little or no literature on this singularity.

To resolve these issues, a novel approximation (labelled CCW^+) is derived, guided by the time-accurate solution of the full governing equations, and an analogy between the surfaces formed of Riemann variables atop the space-time plane, and an imaginary smooth fabric formed of three coloured threads. CCW^+ is shown to be *regular* and applicable to impulsive flow starting; it admits smooth bi-directional motion of the shock wave—reversal of shock motion occurs naturally if an intake fails to start.

Résumé

Ce travail examine des processus de la mécanique des fluides impliquant le mouvement des ondes de choc a travers des chaînes. En particulier, la prédiction et le contrôle de mouvement du choc dans les entrées d'air ont une grande importance pour le vol ultra-rapide et pour les moteurs des vaisseau spatiaux futurs–c'est un problème fondamental dont la solution attire présentement un haut degré d'intért. Mme si les processus de démarrage et non-démarrage dentrées dair sont considérés bien compris au niveau conceptuel, d'importants détails restent à régler.

Dans la première partie de la thèse une étude analytique, numérique et expérimentale est réalisée. L'étude est bidimensionnelle dans le but dévaluer les caractéristiques de l'écoulement quasi-stationnaire dans une entrée dair de type rampe avec compression externe. à l'aide dun modèle bien-connu basé sur la compréhension commune dans le monde scientifique et selon la littérature de spécialité on montre que le model traditionnel basé sur l'écoulement unidimensionnel sur un plan de choc est inexact.

Pour corriger cette situation un nouveau modèle analytique est présenté pour montrer le démarrage dentrées dair en utilisant une onde de choc courbe. Les résultats analytiques sont bases sur des preuves numériques obtenus des simulations CFD ainsi que par éléments expérimentales. Mises ensemble ces résultats constituent des preuves écrasantes à l'appui les arguments présentés.

Dans la deuxième partie de la thèse une étude analytique et numérique est réalisée sur le sujet de l'écoulement instable, quasi-unidimensionnel. Le but est dévaluer la faisabilité de la prédiction de la dynamique des chocs dans une entrées dair en utilisant un modèle e simple, approximatif mais représentative.

Il ny a pas beaucoup des études et connaissances sur le démarrage impulsive dentrées dair disponibles et il nexiste pas une théorie pour prédire analytiquement les fennomanes de démarrage présentées dans cette étude.

La théorie bien-connue de Chester-Chisnell-Whitham est prolongé en utilisant un nouveau modèle (étiqueté lifting isentrope) qui décrit en fait l'écoulement non-uniforme non-stationnaire en haut de londe de choc. On trouve une singularité dans le modèle CCW qui nous empche dutiliser ce modèle dans le démarrage spontanée de l'écoulement. Il y a très peu dinformation, presque pas du tout, sur cette singularité dans la littérature de spécialité.

Pour résoudre ce problème une nouvelle approximation (étiqueté CCW^{+}) est dérivé, base sur les solutions précises de les équations directrices, sur une analogie entre les surfaces des variables Riemann sur le plan espace-temps, et un tissue imaginaire fait de trios couleurs différentes. On montre que la théorie CCW^{+}est stable, régulière et peut tre appliqué dans le démarrage spontanée de l'écoulement. La théorie CCW^{+}couvre le mouvement uniforme bidirectionnel de londe de choc, le renversement de la direction du choc arrive naturellement si une entrées dair ne parvient pas à démarrer.

Acknowledgements

The work presented herein was financially supported through a most generous gift made by Richard Tomlinson to McGill University. I feel fortunate to have had the opportunity to present the essence of this work directly to Dr. Tomlinson in the form of an annual Tomlinson Talk given at McGill University, in the summer of 2007.

I also wish to extend gratitude to my thesis advisor, Prof. Timofeev, for inviting me to McGill, and for fostering a rather pleasurable and an academically free research setting. In the absence of such freedom, my unripe ideas might have borne no fruit. It is also fair to state that he and I share a common interest in intake flows; it was sparked through our association with Sannu Mölder—a dear friend who proposed to us long ago, to analyze and to reexamine via numerical simulation, some of the early experimental work by several researchers in Canada, especially those at McGill and University of Toronto. It is these investigations which led me to the broader idea of imposing high temporal and spatial gradients at particular boundaries in the computational domain, and harnessing of subsequent unsteady effects to overcome difficulties in the general steady flow.

In terms of direct contributions to this work, and the first part of the dissertation in particular, the following persons at McGill provided essential support in manufacturing of the wind-tunnel model:

- Prof. Higgins provided valuable input at the various "design-team meetings" and also generously availed me of his laboratory facilities, test equipment, and raw materials for the experimental model.

- Hayden Smith & Co. of the design-team helped carry out the engineering design, drawing, and fabrication of the wind-tunnel model.

- Steve Kacani and Eddie Del Campo, of the Physics Department machine shop, provided technical assistance in the manufacturing and assembly of the experimental model.

Lastly, I wish to express my thanks to the following persons at Defence R&D Canada (DRDC) for supporting the wind-tunnel experiments:

- François Lesage granted use of the test facilities, monitored the collaboration on DRDC side, and provided valuable discussions and insightful interpretations for the experimental results.

- Rogério Pimentel set up the optics for the experiment.

- Marco Boivin remedied the deficiencies in the model and made invaluable contributions to the mechanical aspects of the experiment.

- Robert Bélanger carried out the instrumentation and collection of raw data for each experiment.

Chapter 1

Introduction

Mach number is like aborigine counting: one, two, three, four, many; once you reach many, the flow is hypersonic.

H. K. Beckmann

1.1 A Quick Perspective on Hypersonics

The subject of hypersonic propulsion deals with engine/vehicle systems which are capable of developing sufficient power to enable flight-speeds that are conveniently measured in units of km/s. Concepts based on *air-breathing engines* have been of varied interest to researchers since the 1950s[3–7]. An air-breathing engine is a propulsive device that is specifically designed to make use of atmospheric air. Instead of carrying oxygen on-board, as is done in a rocket engine, the air can be captured and compressed using an *air-intake*. The intake performs this function using "ram" compression, an effect which is derived from the speed of the vehicle itself, rather than a mechanical device as used in turbojets[8].

In practise, system designers have found the hypersonic environment to be harsh and unforgiving[3,9–11]; nevertheless, there is much renewed interest in this

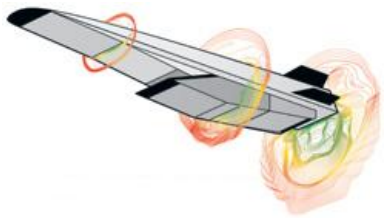

Figure 1.1: Computer simulation of flow around a hypersonic cruise missile. The vehicle forebody forms a large part of the external compression surface of the intake. Taken from[15].

field presently[6], and the recent quests[12,13] stem mostly from tactical advantages gained under military applications (Figure 1.1). These mission areas might include time-critical strike, access to space, and hypersonic global reach[14].

Under commercial applications, the long term economical benefits afforded by such a technology might include: payload delivery[16] to low earth orbits (LEOs), *e.g.*, communication satellites and supplies for the international space station (ISS); suborbital flight for commercial space tourism; and, hypersonic aircraft for intercontinental transport[17]. Some of the technological challenges present in hypersonic air-breathing propulsion are outlined in the following section.

1.1.1 Air Breathing Engines—Technological Challenges

An air breathing propulsion system (*i.e.*, ramjet or scramjet) is typically designed not only to generate enough thrust to overcome the aerodynamic drag on the vehicle for cruise conditions, but also to have sufficient thrust leftover to overcome the vehicle inertia so that it may gain speed and altitude as desired[18,19]. Hence, there exist numerous design challenges and constraints related to the powered high speed flight regime[3,20–24].

Briefly, some of the aforementioned challenges include: the structural configuration, the thermal load management, the airframe-propulsion integration[25–28],

and the related scaling issues[12,29,30]; the addition of fuel to the high-speed airstream[31,32] and the concomitant mixing and ignition issues[33–36]; the interaction between the intake and the combustor and the related unstart issues. Indeed, much of the existing research in hypersonics deals directly with the combustion aspects of the scramjet concept[22,33,37–58]. *The overall efficacy of an air-breathing engine, however, depends greatly on the intake and its ability to capture and compress the incoming air for processing by the remainder of the engine*[59–61]. The basic features and the terminology related to intake starting is explained in the following section.

1.1.2 Intake Starting—Terminology

A major physical challenge in vehicle design is that a large mass of high-speed freestream air is to be captured and much of its kinetic energy is to be converted into internal energy. This conversion of energy is to be carried out efficiently without a great loss in stagnation pressure, and a highly compressed stream of air is to be supplied to the combustion chamber. Hence, the intake is a large and critical component and its design and its operational characteristics directly determine the overall vehicle configuration and integration (Figures 1.1 and 1.2); this, in turn directly relates to many of the aforementioned issues. Hence, it is important to study and understand the fundamental physical processes which govern the design and operation of the intake. *In particular, the establishment of supersonic flow inside the intake is an important first step—it is often referred to as: "flow starting," or "intake starting," or "shock swallowing," or "shock ingestion," or simply as "the starting process."*

In classical texts, the unstarted mode is often labelled as the sub-critical mode; the started mode as supercritical; and the near-transition, metastable, middle

Figure 1.2: Hypersonic cruise missile being tested in a wind tunnel. The vehicle forebody forms a large part of the external compression surface of the intake. Taken from[15]; a video of engine starting is also available on-line *(ibid.)*.

stage is often labelled as the critical mode. The three modes are shown schematically in Figure 1.3. A physical description of these modes (started *vs.* unstarted flow) follows next.

1.2 Started *vs.* Unstarted Flow

To facilitate discussion, here the intake geometry is conceptualized as a simple converging duct with smooth walls, without any perforations or moving parts (Figure 1.3). It is known as the Pitot intake; actual intakes may feature more complex geometry (*e.g.*, Figures 1.1, 1.2, and 1.4), but for the present discussion the Pitot intake sufficiently illustrates the concept.

The earliest recognition of the starting problem traces back to war-time efforts in the 1940s[62,63]. It is since long-established that for a given value of free-stream Mach number ($M_\infty > 1$) there are two distinct flow configurations possible in a convergent geometry: *started* and *unstarted* (see Figures 1.3 and 1.4). A hy-

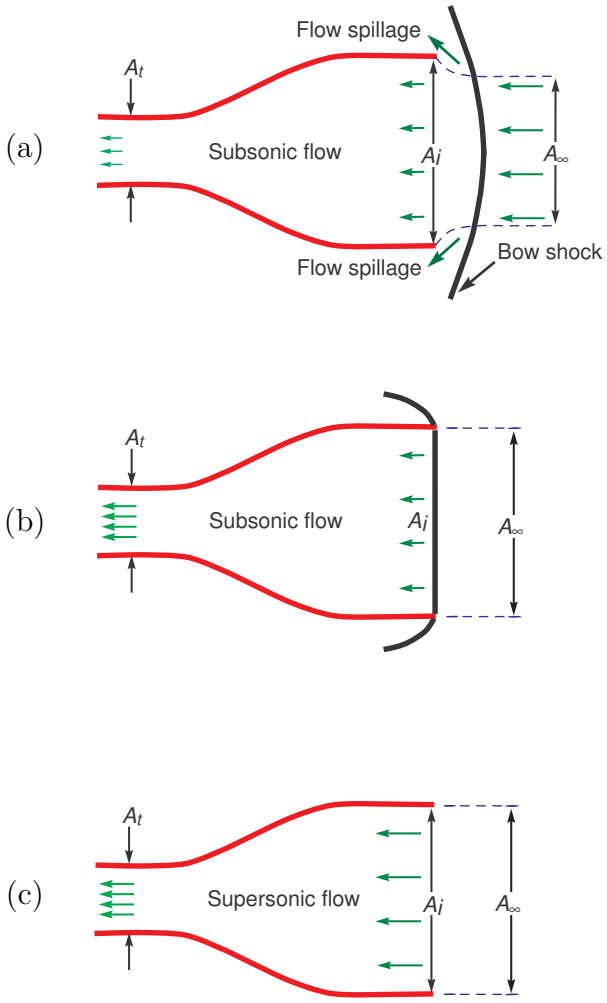

Figure 1.3: Conceptual drawing of the three distinct modes of operation for a duct placed in supersonic flow (Pitot intake): (a) Schematic for an unstarted flow field (subcritical mode). The flow is rapidly decelerated across the shock to subsonic speed. Some of the flow is spilled outward. The rest of the flow enters the channel and is gradually accelerated to sonic state at the throat (choked flow). (b) Shock on lip condition. Kantrowitz-Donaldson transition-condition states that in this critical mode, all of the decelerated subsonic flow across the shock can pass through the choked throat. (c) Started, supercritical mode, throat may not be chocked ($A_t/A_\infty \geq A_s/A_\infty$), otherwise the flow will revert to unstarted mode.

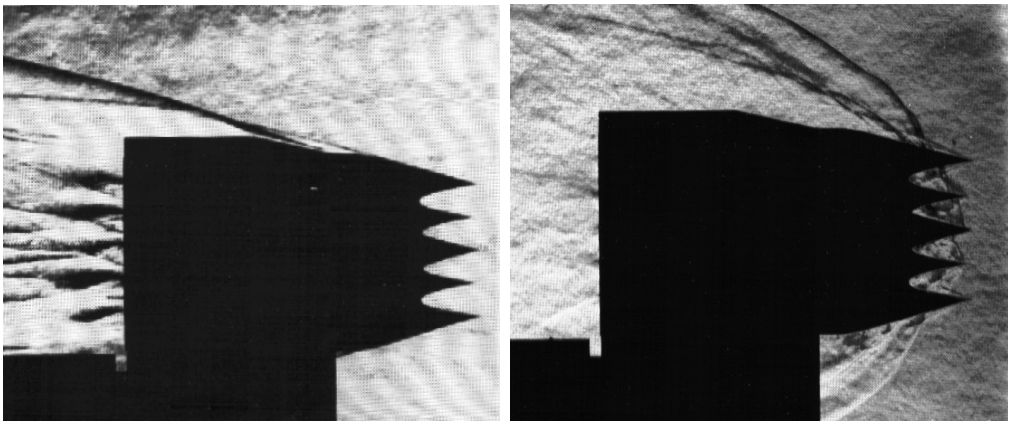

(a) (b)

Figure 1.4: Experimental results illustrating (a) started and (b) unstarted flow configuration. The bow wave and other flow features are made visible using the schlieren imaging technique (light refraction occurs due to the presence of density gradients in the flow). Courtesy of Prof. S. Mölder.

personic intake is said to be *started* when all of the incoming flow is captured ($M_\infty >> 1, M_i >> 1, M_t \geq 1$); in this mode, large air mass is captured (Figures 1.3c and 1.4a), which is a desirable condition. Conversely, the intake is said to be *unstarted* if much of the incoming flow is spilled; this spillage typically occurs aft of a bow shock, as shown in Figures 1.3a and 1.4b, while the outflow is choked ($M_\infty >> 1, M_i < 1, M_t = 1$); in this mode, large air mass is spilled, and the remaining amount carries significant losses with it which are associated with passage across a bow shock. *Thus, gaining a fundamental understanding of the inlet starting process is highly desirable and it amounts to analysis of the shock swallowing process.*

1.2.1 Classical Operability Limits

The classical theory for predicting starting and unstarting behaviour of fully-enclosed, converging ducts is established in[62,64]. This theory is based on a remark-

ably simple yet representative shock on lip (SoL) condition with the assumption of *quasi one-dimensional, quasi-steady, homentropic flow* downstream of the bow shock (Figure 1.3). The critical or the SoL condition is attained as $A_\infty \to A_i$.

This theory is graphically presented in Figure 1.5, which shows three distinct regions in the area-ratio, Mach number plane: area-ratios above the Kantrowitz-Donaldson limit (curve labelled 1–3k–6k) span a region where flow is not choked, the shock is swallowed, and inlet starting takes place; area-ratios lying below the isentropic compression limit (curve labelled 1–3s–6s) span a region where flow is choked, the shock is regurgitated, and unstarting takes place; the *middle* region between these two curves permits stable started operation (once started, the flow remains unchoked). That is to say: in this middle region, if the flow is unstarted then shock swallowing does not occur and the flow remains unstarted, but if a started inlet is somehow brought into this region (*e.g.*, using variable geometry) then it does not revert to unstarted configuration.

To satisfy compression requirements, inlets of practical interest lie close to the isentrope (curve labelled 1–3s–6s). For example, consider a *fixed-geometry* converging duct without mass spillage: referring to Figure 1.5, the smallest area-ratio that can be started under *quasi-steady* conditions is an order of magnitude larger than that which is desired for hypersonic cruise conditions (shaded region).

1.2.1.1 Terminology and Idiosyncrasies

Some parts of this work make reference to a so called index of startablity for one-dimensional flow (IoS)[65]. The basic idea behind this is simple: to divide the (area-ratio *vs.* Mach number) parameter space linearly between the classical limit on self-starting (Kantrowitz-Donaldson) and the classical limit on operability (isentrope). This division is made such that IoS $= 1$ corresponds to curve (1–3k–

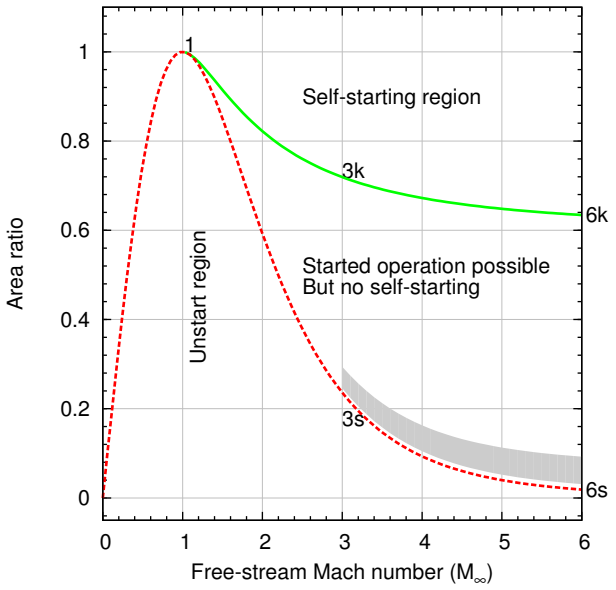

Figure 1.5: Area ratio required for diffusion to sonic speed from a given free stream Mach number. Curve (1–3k–6k) is for the shock on lip (SoL) condition in a Pitot intake where a shock is located exactly at the entrance plane ($A_\infty = A_i$), followed by steady homentropic flow inside the channel. Curve (1–3s–6s) is for no-shock case, *i.e.*, with homentropic flow everywhere; it establishes an ideal operational limit under steady flow conditions in the absence of viscous and body-forces. Note that most practical intakes fall in the region between these two curves, where the intake fails to start under steady flow conditions. Also compare with Figure C.1 on Page 176. Plot is valid for ($\gamma = 7/5$).

$6k$) and IoS = 0 corresponds to curve (1–3s–6s). This definition is reviewed in greater detail in Appendix C, along with a plot showing curves for various constant values of the IoS function on Page 176.

1.2.2 Problem Statement—Need for Further Analysis

While the process of intake starting and unstarting is considered well understood at a conceptual level, significant details remain to be resolved[60]. The situation is well-captured in this plain sentiment: Intake starting information is difficult to obtain without an experimental test[61]. Indeed, some variation exists in the very definition of what constitutes started flow; in practise, even the basic determination and classification of results (started *vs.* unstarted) may pose a challenge in itself[60,66,67]. *Hence, the phenomenological understanding seems to be lacking insofar as applications/extensions of the existing theory to actual intakes appear to be greatly limited in practise.*

1.3 Review of Known Techniques

Various possibilities and methods exist to permit intake starting and to ensure predictable and controlled flow[59,63,65,68–77]. *An attempt is made to classify the basic approaches below, however it is not surprising that most practical designs incorporate and combine features from one or more of the basic techniques.* These basic approaches are reviewed in greater detail below.

The widely known methods for intake starting are all designed with the assumption of *quasi-steady* flow conditions for both the free-stream flow, as well as the flow inside the intake. These techniques include: variable geometry, overspeeding, overboard spillage, and perforated diffusers. It is possible to design a

vehicle employing one or more of these techniques simultaneously.

Alternate approaches—and, these are less widely discussed—make use of *unsteady* flow features to overcome the classical quasi-steady operability limits on flow starting outlined in §1.2.1. Here, one may imagine suddenly *jumping* into the *middle* region of Figure 1.5. The transition from a *steady unstarted* configuration to a *steady started* configuration is thus achieved, albeit without meeting the geometric constraints stemming from the Kantrowitz-Donaldson limit.

1.3.1 Steady Flows

1.3.1.1 Overspeeding

Perhaps the most well known method is the so called overspeeding technique[68]. Referring to Figure 1.5, a vehicle (featuring an intake of a particular area-ratio) is accelerated until the free-stream Mach number is increased past the Kantrowitz-Donaldson limit which corresponds to the particular area-ratio (*i.e.*, until curve labelled 1–3k–6k is crossed). Once the flow is started, the vehicle can be safely decelerated and brought back into the middle region, where it can operate most efficiently, close to (but above) the isentrope. This approach does not work for hypersonic inlets (featuring small area ratios, designed to operate at high Mach numbers), because the Kantrowitz-Donaldson function exhibits a plateau at those speeds (curve labelled 1–3k–6k cannot be crossed in this fashion for small area ratios). But for relatively low Mach number applications (*e.g.*, $M_\infty \sim 1.6$), this general approach is both simple and practical.

Figure 1.6: SR-71B Blackbird with translating centerbody in the intake. Taken on December 1994 from an in-flight refuelling tanker. SR-71B was the trainer version of the SR-71. Notice the dual cockpit to allow the instructor to fly the airplane. NASA Photo EC94-42883-4.

1.3.1.2 Variable Geometry

Another method used to start an intake involves temporarily changing its geometry[69–71] such that it satisfies the aforementioned limits. The small area ratio intake is transformed into one with a larger area ratio (*i.e.*, until curve labelled 1–3k–6k is crossed). The change can be effectuated by opening up the exit or by closing down the entrance.

Seminal work on variable geometry intakes includes various experimental studies performed in the late 1950's. Use of translating centerbodies and cone inlets, similar to the SR-71 Black Bird (Figure 1.6) and the Russian MiG-21 fighters (Figure 1.7) is examined in[78,79]; performance of truly variable geometry inlets is reported in[75,80].

For simple intake geometries, variable area ratio may be easy to implement. However, the weight penalty and mechanical complexity of a variable geometry

Figure 1.7: Translating nose cone intake of the Russian MiG-21 (in use from the mid 1950's). At low speeds ($M_\infty < 1.5$) it is fully retracted; between speeds of ($1.5 < M_\infty < 1.9$) it is in the middle position; and at higher speeds ($M_\infty > 1.9$) it is in the maximum forward position. Source: Wikimedia Commons.

system can also make this option unattractive. This especially holds true for expendable vehicles, such as the light-weight missiles[12]. The variable geometry can also incorporate external compression surfaces which will be discussed further in §1.3.1.4; in this manner, multiple design points* can be incorporated, or at worst, the combined approach can be used to improve the off-design performance (Figure 1.7).

1.3.1.3 Perforated Diffusers

Another approach is to allow for mass spillage through holes/slots/porosity in the walls of the intake. This approach effectively increases the total exit flow area to that which is required by the Kantrowitz-Donaldson function for self starting. Once the intake is started, the perforations may be closed and the intake should remain started (provided that exit flow does not choke during the closing process).

*For definition, see the List of Terms.

Early experimental studies on perforated diffuser form several classical reports[63,72–74] on the subject of intake starting. More recent developments incorporating improved theoretical/analytical models, as well as numerical and computational fluid dynamics (CFD) verifications of the analytical results are reported in[65,81,82]. These advancements[82] promise considerable improvement in design (hole sizing and location) over the classical results. At low Mach numbers ($M_\infty \sim 2$), the aforementioned classical experiments[63,72] successfully demonstrated very high efficiency perforated diffusers. Recent experimental tests performed using a semi-stream-traced and shape-blended, perforated diffuser are reported in[76]. In practise, due to the complexity of the flow geometry and lack of available data, the sizing, number, and location of perforations required to start the intake are determined empirically, *ibid.*

While closing of perforation was not performed in any of the studies cited above, it is believed that for a hypersonic vehicle, once the flow is started, closing of the perforations is a must. For a hypersonic cruise vehicle, if the perforations are sized according to quasi-steady flow conditions, perhaps as much as 95% of mass may need to be spilled-through during the starting process[81]. In the started mode however, the increased value of streamwise momentum of the core flow leads to a dramatic reduction in spillage; this is the so called smart-hole effect.

As with variable geometry, regulatory mechanisms (*e.g.*, flaps, doors, valves, *etc.*) for closing of the perforations lead to further structural and airframe-propulsion integration challenges. The additional mechanical complexity of the engine and the concomitant weight penalty is a disadvantage, especially for expendable vehicles[12]. However, these constraints may be alleviated and the approach made more effective by combining it with one or more of the other techniques (particularly overboard spillage). This is effectively the mechanism employed in[76]

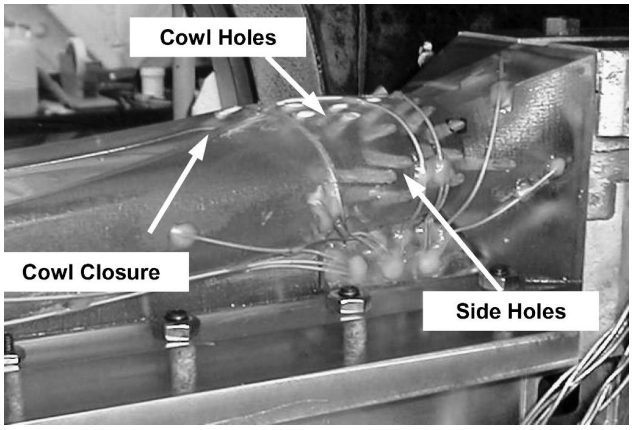

Figure 1.8: The famous "REST" inlet with spillage holes, taken from[76]. The basic design falls under the stream traced wave-rider concept, but it is shown here as an example combining the use of perforations to assist flow starting.

for lowering the Mach number at which the intake self starts (Fig: 1.8).

1.3.1.4 Mixed Internal/External Compression Geometry—The Wave-rider Intakes

A commonly employed approach is that of combining internal contraction with an external compression geometry in a single unified design. This design practice is almost universally employed in modern vehicle concepts. It reflects the fact that starting is made easier by incorporating a built-in spillage mechanism into the design. It also reduces the effective contraction in the unstarted mode as the flow is not physically bounded on all sides (Figure 1.9).

In the started mode, the external surface is used to precompress the flow before it enters the fully enclosed "internal contraction" section. In the unstarted mode, the external unbound geometry permits "overboard spillage" to take place upstream of the internal contraction.

Once the flow is started, the supersonic nature of the flow dictates that small

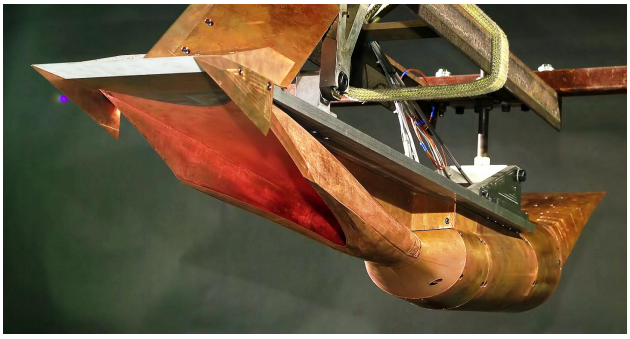

Figure 1.9: The famous "REST" inlet, taken from[16]. The basic design methodology gives a stream traced intake suitable for a wave-rider; it is shown here to emphasize large provision for subsonic spillage to assist flow starting.

disturbances generated at the intake do not perturb the upstream/incoming flow. Hence, from the engine-design viewpoint, the same stream/mass capture is maintained as in the case of a fully enclosed (bounded flow) geometry.

The external compression surface can be either fixed or variable in geometry. This surface is usually formed by the underside (aerodynamically shaped belly) of the vehicle, giving the "wave-rider" family of hypersonic vehicles[83] their characteristic look (Figures 1.1 and 1.2). Numerous designs exist depending on the vehicle application. For the two-dimensional case, the common ramp-type geometries include the two-shock (Appendix A) and the Prandtl-Meyer intakes (Appendix B). The axisymmetric analogues of the two planar cases include the conical forebody[84,85] and the Oswatitsch spike intake[86,87]. Figures 1.6 and 1.7 show classical designs based on these concepts.

For the three-dimensional case, stream-traced* geometries are also used[67]. Possible disadvantages or at least some uncertainties about these include the effect of yaw and angle of attack on flow stability.

*The resulting geometry is carved out, usually based on a cardinal streamline, from a fully enclosed, symmetric, known internal flow (Figure 1.10).

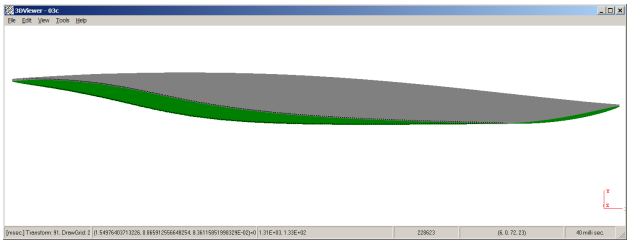

Figure 1.10: An example of a doubly curved stream traced inlet based on Busemann flow. Flow would be from left to right; inside surface is partially visible and is rendered in green. Note the large provision for flow spillage in the unstarted mode. (Own work.)

From the flow starting viewpoint, the behaviour of aforementioned intakes (both in two- and three-dimensional geometries) is quite different from the quasi-one-dimensional model (Figure 1.5). In general, their starting characteristics are notoriously difficult to estimate[60,61] and can only be ascertained through experiments[76].

1.3.2 Essentially Unsteady Flows

In addition to the works based on classical quasi-steady limits, there is also some data available for unsteady flow starting. Conclusive experimental evidence[10] exists indicating that flow starting can occur spontaneously in very low area ratio intakes, *e.g.*, when tested in gun-tunnel experiments[88]; hence, a separate set of limits on unsteady flow starting may exist[77].

While advancements in accurate numerical solution of the unsteady form of governing equations (unsteady Euler equations) has lead to a greater understanding of the transient evolution of complex wave structure during the starting process, there is little or no theoretical treatment available describing the essentially unsteady starting phenomena.

Computer simulations[77] where some level of controlled unsteadiness is prescribed show that a separate set of limits may exist for inlet starting under un-

steady flow regimes. The physical nature of these limits is not precisely understood owing to the lack of available analysis; a distinct paucity of theoretical or experimental studies exists, especially in comparison with the various approaches based on quasi-steady flow, as mentioned above.

1.3.2.1 Highly Accelerative Motion

For example, one situation may be that of a vehicle/intake undergoing relatively high acceleration (non-negligible volumetric force term in the governing equations). Computer simulations and scale analysis[77] have shown that the critical acceleration required to start an inlet can be rather large (from 1,000 g's to 10,000 g's depending on the intake area ratio). *However, fundamental knowledge about the unsteady shock motion during the critical stages of acceleration is not known.*

1.3.2.2 Membrane Rupture

Another plausible situation may be that which results from the rupture of a thin/frangible membrane, mounted at the entrance plane of the inlet. The rupture process must occur rapidly enough to cause sufficiently high localized spatial gradients, which subsequently lead to significant unsteadiness in the general flow. The unsteady flow is not subject to the steady-state starting limitations, and may be useful for intake starting. Various samples of such unsteady behaviour in inlets are demonstrated in[77].

1.3.2.3 Gun Tunnel Tests

On the experimental side, impulsive flow starting has been widely observed and reported[10]; this is particularly true of shock tube and gun tunnel tests. While these tests constitute an economical and effective method of investigation, it only

allows for short duration testing* of geometries to determine their performance characteristics (typically in the started mode). Hence, these studies do not directly provide a separate starting technique to be used in flight as such.

1.3.2.4 Ram Accelerator Tests

Tests conducted in an evacuated tube (barrel), inside which, a projectile (scale model of intake/vehicle body) is rapidly accelerated to high velocities must also contain started flows. In this concept, the high speed projectile then pierces a diaphragm and enters a section of the barrel containing premixed combustible gas. The flow configuration surrounding the projectile is setup to give rise to a stable (attached) detonation wave at the projectile shoulder, thus enabling further acceleration of an otherwise unpowered projectile. Applications of this concept include high velocity projectiles, including ballistic launch and insertion of small payloads into LEO.

1.4 Roadmap

The remainder disquisition is organized in two separate parts: the first part deals with the quasi-steady flow starting process in mixed-compression ramp intakes; the second part deals with with a fundamental theoretical issue in the shock dynamics which occur during the impulsive starting/unstarting processes. *The rationale and the original contributions made in the respective parts are outlined below.*

*Typical run times are measured in tens of milliseconds.

1.4.1 Off-design Starting in Mixed Compression Intakes

1.4.1.1 Rationale

For relatively simple geometries, the on-design* starting characteristics can be obtained as a straight-forward† extension of the Kantrowitz-Donaldson theory. *However, even for these relatively simple flow geometries, the off-design starting characteristics are not known*; the very same difficulty arises in the operability analysis of mixed compression intakes used in wave-riders, including the stream-traced intakes which arguably hold the most promise for steady-flow applications. Hence, it seems appropriate to further examine the off-design starting condition for the ramp intakes.

1.4.1.2 Contributions

A novel analytical model is proposed in the first part of the thesis to predict off-design self-starting behaviour; its application is demonstrated for a particular two-shock ramp intake. The calculations are compared with the CFD result which lend credence to the assumptions made in the analysis. *Finally, significant circumstantial evidence is obtained experimentally, further supporting the conclusions reached analytically.*

1.4.2 Singularity in Shock Dynamics

1.4.2.1 Rationale

As already mentioned, the precise nature and the physical mechanism(s) involved in establishing the limits on unsteady flow starting are not known. However, at

*See design point in the list of terms.
†These results are included in Appendix A and Appendix B for completeness.

an intuitive and conceptual* level, the final outcome of the "unsteady processes" or "involved phenomena" must lead either to a started†, or an unstarted flow‡. The in-between unsteady states are thus related by the dynamic motion, inside the duct, of that transient bow shock. The above description of unsteady shock motion naturally suggests a direct application or an extension of the classical shock dynamics theory[89–91] to intake starting; such an attempt is made in the present work. However, it turns out that the shock motion, as predicted by the Chester, Chisnell, and Whitham (CCW) approximation, manifests a mathematically singular behaviour. *The physical relevance of this singularity is not known or properly understood in the present context.*

1.4.2.2 Contributions

The above issues surrounding the singularity are discussed, and a novel formulation addressing them is presented in the second part of this work. Application of the resulting ideas is demonstrated for a particular geometry, undergoing accelerative motion, as an example. *The resulting formulation is also shown to be applicable to other more classical problems of shock dynamics.*

*Used in the sense of unsteady, quasi-one-dimensional flow.
†If bow shock is swallowed, steady state leads to Figure 1.3c.
‡If bow shock is regurgitated, steady-state leads to Figure 1.3a

Part I

Off-design Starting in Mixed Compression Intakes

Chapter 2

Off-design Mixed Compression Ramp Intakes

What most experimenters take for granted before they begin their experiments is infinitely more interesting than any results to which their experiments lead.

Norbert Wiener

2.1 Introduction

This chapter follows the rationale from §1.4.1.1. As reviewed earlier in §1.3.1.4, the two- and three-dimensional mixed-compression intakes are said to behave quite differently from the quasi-one-dimensional model of Figure 1.5. As such, the analytical operability limits do not correspond well with the experimental results. For the two-dimensional case, the common mixed-compression ramp intakes include the two-shock intakes. These intakes are based on a well-defined geometry and a rational design point for analysis of flow starting.

An analytical, numerical, and experimental study was thus performed to model flow starting inside a ramp intake. The experimental tests were conducted in the

Valcartier trisonic wind-tunnel facility of DRDC[92], at three different free-stream Mach numbers, M3, M3.5, and M4, using the nozzle blocks for the highest available Mach numbers. The intake geometry was designed based on a two-shock concept, with the assumption of perfect cancellation of the internal shocks at a design free-stream Mach number of three ($M_D = 3$). The intake area ratio was designed such that it straddled the expected self-starting curve near M3.5. To explain these subtle points further, and to facilitate discussion, the conceptual mechanism for flow starting in a typical ramp intake is examined next.

2.2 Conceptual Mechanism for Starting

Consider the geometry of a mixed-compression intake, such as the one shown in Figure 2.1, which features overboard spillage in the unstarted mode. As the free-stream Mach number is increased, the bow shock approaches the leading edge of the intake (Figure 2.1a). As the Mach number is increased further, the shock wave becomes attached at the leading edge in the aft portion (Figure 2.1b). The outboard flow also adjusts to the changing conditions around the main body as the mass flow through the throat remains choked. The capture area (A_∞) also increases gradually with the increasing free-stream Mach number. The changing flow configuration accommodates subsonic spillage mechanism in the cowl region. While the intake remains unstarted, this spillage mechanism enables the remaining flow, which cannot be ingested through the choked exit, to spill around the cowl (Figure 2.1c).

In a sense, the overboard spillage mechanism resembles the behaviour of a variable size perforation located near the entrance of the inlet. While the flow is unstarted, a bow shock is situated upstream of the inlet cowl, and subsonic

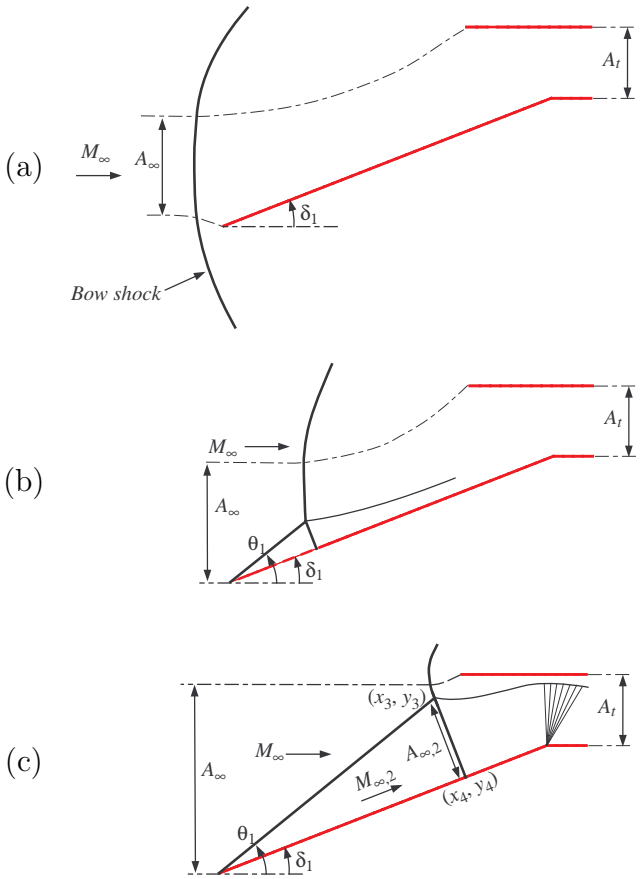

Figure 2.1: Schematic drawing of flow spillage in a mixed-compression ramp intake during the starting process.

spillage takes place downstream of that shock. In the scenario, where the bow shock is located at the cowl plane (or is swallowed), no overboard spillage occurs upstream of the cowl leading edge ($A_{\infty,2}$=A_i in the sense of Figure 1.3b on Page 5). Indeed, during the starting process, as the shock approaches the cowl, the entire wave complex around the cowl lip acts as a smart hole (Figure 2.1a–c).

2.2.1 Traditional Approach

Based on the above description, it seems natural to extend the classical one-dimensional Kantrowitz-Donaldson model to account for the overboard spillage. Hence, the multidimensional starting problem is treated in the literature, almost universally, by assuming a quasi-one-dimensional flow downstream of the cowl lip and a simple "internal contraction" is compared with the classical Kantrowitz limit computed using a "mass-averaged" Mach number upstream of the cowl shock[10,76]. Experimental and numerical studies in the literature widely report using this estimation technique[61,76,93–99], but the degree of success with which one can predict starting, is reported to vary from model to model and from wind-tunnel to wind-tunnel[60,61,76].

2.2.2 On-design Startability (2S-Intakes)

For clarity of presentation, formulae used for determining the on-design self-startability of a two-shock inlet are included separately in Appendix A. Here, it suffices to include the useful results in graphical form (Figure 2.2). It is interesting to note that under the definition of the IoS function, the startability of a two-shock inlet for the weak reflected shock (WRS) design is well approximated by IoS $\simeq 0.6$, while the startability of the strong reflected shock (SRS) design is well described by IoS $\simeq 0.35$. The IoS $\simeq 0.25$ curve provides a good approximation for the supersonic operational limit of an on-design two-shock inlet. These approximations especially hold well at low to moderately high values of free-stream Mach numbers ($1 < M_\infty < 4$).

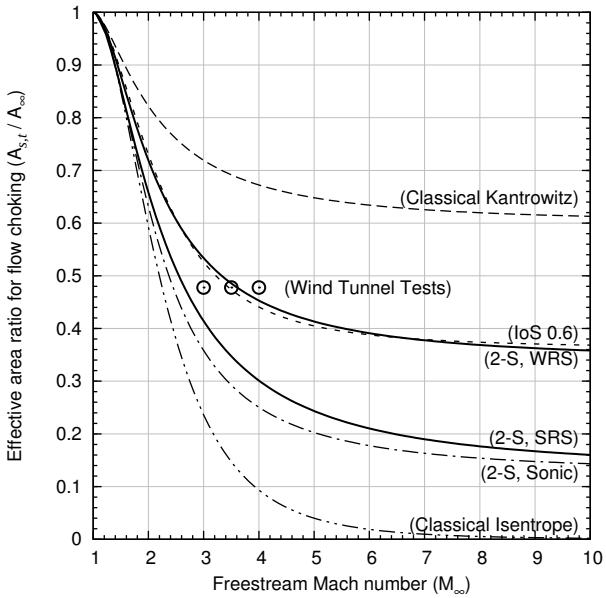

Figure 2.2: Self-starting ability of two-shock inlets compared with classical operability limits. Self-starting of an on-design two-shock inlet with weak reflected shock (WRS) design-point is well approximated by the IoS $\simeq 0.6$ curve. The self-starting curve for the strong reflected shock (SRS) design indicates dramatic improvement over the (WRS) design. Operability limit of a two-shock inlet with sonic-design ($M_t = 1$) is also plotted. The M3IoS0.5 design point is shown at M3, M3.5, and M4 in relation to the (WRS) self-starting curve. Plot is valid for $\gamma = 7/5$.

2.3 Selection Basis for Experimental Tests

With the above considerations, it now seems possible to determine the area ratio suitable for experimental testing in the DRDC tunnel. The experimental setup was designed as part of a broader research program[100], with the aim to establish experimental capability for testing membrane rupture (§1.3.2.2). Also, as indicated in §2.1, the available nozzle blocks allow testing at M3, M3.5, and M4. Hence, based on these considerations, we note that the M3IoS0.5 (Figure 2.2) design point is suitable. It is not self-starting at the M3 test condition, as this point lies below the self-starting curve approximated by IoS $\simeq 0.6$. Indeed, this approxi-

mation (interpretation of the self-starting curve) suggests that, under quasi-steady flow conditions, the M3IoS0.5 point is self-starting at $M_\infty \simeq 3.62$. One may then generate a hypothesis based on this approximation, that the intake would be self-starting only at the M4 and not at the M3 or M3.5 test conditions; we will return to this hypothesis later on.

2.3.1 Actual IoS of On-design Ramp Intakes

While the relative merits of overboard spillage in aiding flow starting are evident from the above stated IoS values, it is more convenient to redefine (C.1) specifically for the two-shock inlet geometry. Hence a new function (IoS_{act}) is proposed, and it is constructed using the starting model as described in Appendix A, so that on-design self-starting would occur precisely at $\text{IoS}_{\text{act}} = 1$. Referring to the geometry of Figure A.1b,

$$\begin{aligned} \text{IoS}_{\text{act}} &= f(\gamma, M_\infty, A_t/A_{\infty,2}) \\ &= \max\left(0, \min\left(1, \frac{A_t/A_{\infty,2} - A_s/A_{\infty,2}}{A_K/A_{\infty,2} - A_s/A_{\infty,2}}\right)\right). \end{aligned} \tag{2.1}$$

Figure 2.3 shows a plot of (2.1) for a range of free-stream Mach numbers. Under this new definition, the IoS value lies in the range [0:1], where a value of unity signifies self-starting characteristics. As can be seen, for a given free-stream Mach number, with the SRS design, a lower area ratio is permissible while maintaining self-starting characteristics. For example, the WRS design (Figure 2.3a) permits an intake with $A_t/A_\infty \simeq 0.36$ to self-start at $M_\infty = 10$, whereas the SRS design (Figure 2.3b) allows the same area ratio to be started at $M_\infty \simeq 3$.

As expected, the iso-contours for $\text{IoS}_{\text{act}} = 1$, as rendered in the area-Mach number plane of Figure 2.3, agree with the self-starting curves shown in Figure 2.2,

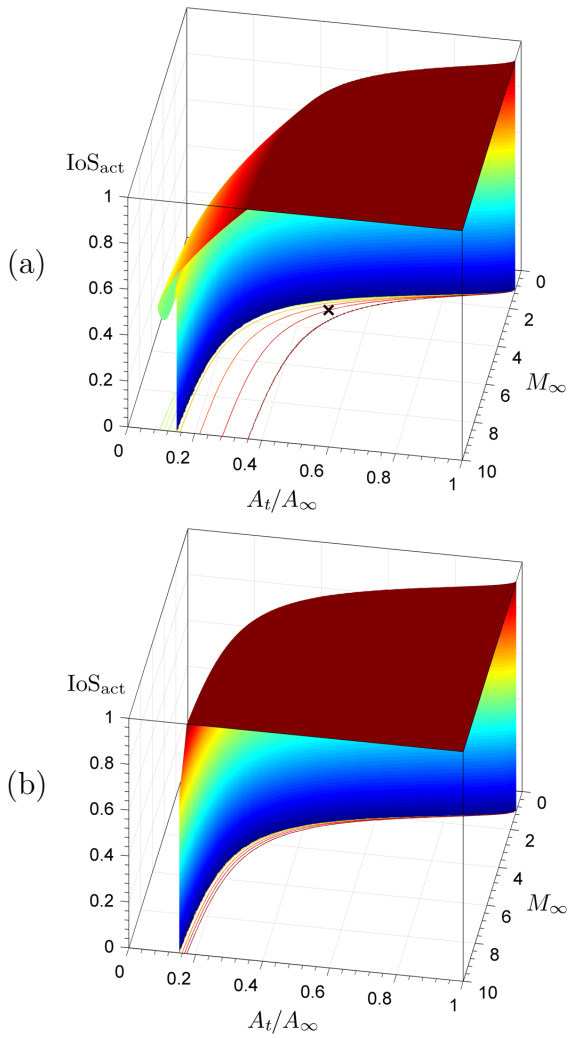

Figure 2.3: Self-starting ability of two-shock inlets: Weak reflected shock (a); Strong reflected shock (b). Isolines for the IoS values are rendered in the $(M_\infty, A_t/A_\infty)$-plane, at IoS $= \{1, 0.9, ..., 0.5\}$. These figures are mainly intended to demonstrate the highly non-linear and non-monotone nature of the starting boundaries, as evident by the "kink" in surface (a), and the "steepness" in (b); in other words, the rendered iso-contours are non-monotonic for IoS$_{\text{act}} \simeq 0.7$ and values below that, as shown in (a); similarly, the compact nature of the contours in the $(M_\infty,\ A_t/A_\infty)$-plane, as shown in (b), indicates that the start-no-start boundary is very sharp for the SRS configuration space. These effects are most-easily captured in the shown surface plots, and offer better understanding of the starting characteristics than the curves shown in Figure 2.2; indeed, the design point of the wind-tunnel model lies near the IoS$_{\text{act}} \simeq 0.9$ curve, as denoted by the "x" in the top figure.

for both the WRS and the SRS design concepts. The design point of the example geometry used here, and also selected for wind tunnel tests, lies on the $\text{IoS}_{\text{act}} \simeq 0.9$ curve, as denoted by the "x" in Figure 2.3a.

2.3.2 Relation to Stream Traced Geometries

In comparing Figures 2.3 and 1.5, it is evident that the new curves (particularly, the $\text{IoS}_{\text{act}} = 1$ curves for self-starting) lie below the original Kantrowitz-Donaldson function (IoS = 1). The distance between these curves points out the degree to which the overboard spillage aids flow starting when compared with a fully enclosed duct. Indeed, a fully enclosed planar intake can be constructed based on this geometry (using symmetry about the upper wall), and in the present idealized context, its starting characteristics would then match the original Kantrowitz-Donaldson curve. *While the performance of the two intakes would be identical once the flow is started, their behaviour in the unstarted flow would be dramatically different.*

The improved starting characteristics shown in Figure 2.3 suggest that other geometries likely benefit to a similar degree. It might also be advantageous to construct stream traced geometries which provide maximal external spillage in the unstarted mode, without sacrificing performance in the started mode.

While the potential advantages of overboard spillage are clear from this analysis, some important factors need further consideration. Such factors likely include flow instability and sensitivity to yaw and angle of attack, *etc.* The sensitivity point seems particularly relevant when considering the non-linear compact nature of the curves in Figure 2.3b. These complexities have not further been considered here.

At hypersonic speeds, the self-starting characteristics exhibit strong Mach

number independence; in this sense, the two-shock geometries carry limited potential and relatively small contraction ratios (~ 6) are possible at best. Stream traced geometries with weaker forebody shocks or more efficient (isentropic) compression processes combined with SRS may posses significantly better self-starting characteristics (*e.g.*, Appendix B).

2.4 Self-starting at Off-design Condition

In the discussions so far, the flow behaviour has only been illustrated near the on-design self-starting conditions. However, recall from section 2.3 that for a 2S-WRS, the (M3IoS0.5) design point is not self-starting. *Naturally then, the question arises: at what value of off-design Mach number would the above inlet self-start? And, more generally, is it possible to obtain a reasonably accurate model for predicting self-starting at off-design conditions?*

2.4.1 Analytical Model

An attempt will now be made to answer the above questions, and to seek an approximate analytical model describing the starting behaviour of the (M3IoS0.5) design point. In particular, judging from Figure 2.2 and Figure 2.3a, the self-starting design point for $M_\infty \simeq 3.62$ gives an area ratio close to the area-ratio for the present (M3IoS0.5) design. However, as hinted earlier, the hypothesis that the model should not start at M3.5 requires further testing; *i.e.*, from that figure alone, it is not sufficiently clear as to how the actual flow would behave because that particular starting curve is valid only for $M_\infty = M_D$, an assumption which no longer holds in the present case.

Following the traditional approach (§2.2.1), the critical conditions at which the

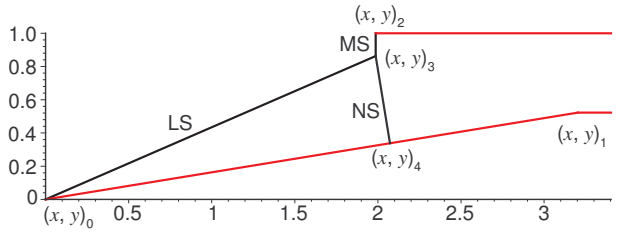

Figure 2.4: First analytical model for self-starting at off-design Mach number with a straight-segment shock (NS); (M3IoS0.5) design, operating at $M_\infty = 3.55$. LS–leading-edge shock; MS–Mach stem; and, NS–normal shock.

(M3IoS0.5) model should self-start may be estimated using the "simple" model of Figure 2.4. This condition may also be stated mathematically, as follows:

$$0 = -A_t + (y_2 - y_3)\frac{A_K}{A_\infty}(\gamma, M_\infty) + \int_{\text{NS}} \mathrm{d}A_s \tag{2.2}$$

Here, the first term accounts for the throat area, the second term accounts for the Kantrowitz area contribution at the short Mach stem (modelled as a straight normal shock), and the last term represents integration over the NS shock segment for the sonic area downstream of the segment; effectively, it is the Kantrowitz area for this shock wave. To obtain the critical value of Mach number for a given geometry, (2.2) can be solved for M_∞.

A value of $M_\infty = 3.55$ was thus obtained for Mach number at which the (M3IoS0.5) intake should self-start according to this simple model. This prediction further enforces the hypothesis* that the (M3IoS0.5) intake should show started flow at the M4 test condition only.

To better judge the validity of this last assertion, a set of high resolution numerical simulations was carried out next.

*Recall the interpretation of the self-startability curve from §2.3, and the discussions surrounding Figure 2.2 and Figure 2.3a.

2.4.2 Simulation Model

An existing CFD package[101] was used to carry out a series of simulations to determine the critical Mach number for self-starting. These simulations were exclusively carried out using the inviscid, perfect gas model. The simplification in modelling of the physics was justified in the present context for several reasons. In particular, the main aim here was to improve the present conceptual and analytical level of modelling which is also based on the perfect gas assumption. Hence, the first step should be improvement of the analytical/conceptual model within the inviscid framework—until it is truly representative of the underlying multidimensional flow phenomena inherently present in the ramp intakes.

These computations were carried out using five levels of refinement. It means that tiny mesh-cells (32x smaller compared to the background mesh) were automatically inserted in areas containing shock waves and slip layers; this well-known technique enables better resolution and capturing of the locally high spatial gradients[102]. Based on previous experience with similar flows, depending on the background mesh size,* typically three to five levels of refinement provide adequate to high levels of engineering accuracy, respectively. This was confirmed through a grid convergence study for the critical-condition result (at three significant figures in the value of critical Mach number for starting).

The free-stream Mach number was gently increased until the incipient starting point was reached. Steady-state solution was occasionally established in the process, to rule out unsteady flow effects. One such solution, near the incipient starting condition, is shown in Figure 2.5.

The critical value of Mach number for self-starting of this model was thus

*Background mesh size typically depends on local geometric features; in this way, specifying a global grid step size of 1–3% of the characteristic length scale ($h \simeq 0.01 L_{\text{char}}$), with a cell-to-cell volume-ratio of 1.6 may be considered to yield sufficiently accurate results.

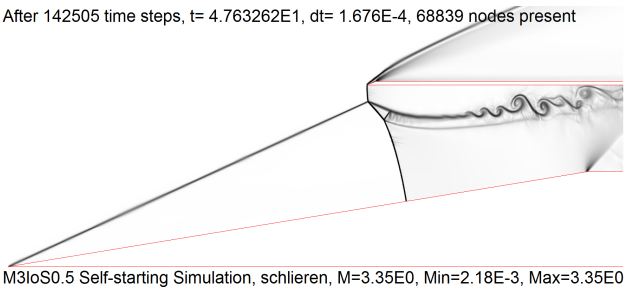

Figure 2.5: Incipient starting condition (nearly started flow) for the (M3IoS0.5) design; self-starting condition at $M_\infty = 3.35$ is shown.

determined to be $M_\infty = 3.35$ (compared to a value of 3.62 from Figure 2.2, and a value of 3.55 from the simple analytical model of §2.4.1). Comparison between Figures 2.5 and 2.4 shows that the curved shock waves are a key feature present in this flow. The multidimensional difference between the two models was deemed to be the main source of the disparity in self-starting prediction.

2.4.3 Analytical Model—Revisited

In the above context, with ideal conditions used in both models, the analytical prediction (3.55) is deemed to be significantly higher than the CFD result (3.35). To remedy this discrepancy, we can try to eliminate some of the assumptions made in the simple model. Firstly, this model assumes two straight segmented shocks: one for the Mach stem (MS) and the other for the "normal" reflected shock (NS). Physical flow only requires that the Mach stem be perpendicular at the upper wall, while the reflected "normal" shock be perpendicular at the ramp. The flow downstream of this assumed wave structure was treated as subsonic (true, as both shocks were normal to the flow at all points). Physical flow does not necessarily abide by this requirement. Furthermore, a more realistic physical requirement is that the pressures match (on either side of the slip layer) downstream of the triple

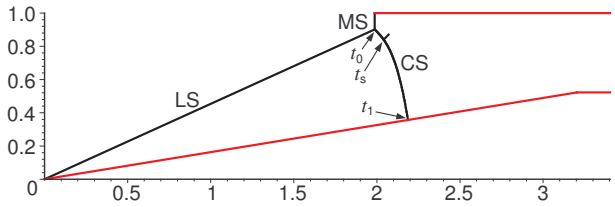

Figure 2.6: Second analytical model for self-starting at off-design Mach number with curved reflected shock; (M3IoS0.5) design, operating at $M_\infty = 3.378$. LS–leading-edge shock; MS–Mach stem; and, CS–curved shock.

point. Indeed, this condition was relaxed in the above analysis.

The key differences may then be attributed to the fact that the actual Mach stem and the actual reflected shock form curved structures, and that the total pressure (and concomitantly, the mass flux) across these curved shock segments may be higher than that which is required in the simple analytical model (with the two straight-segment shocks).

To improve the aforementioned prediction, an analytical model for the curved reflected shock was first obtained, as shown in Figure 2.6. The new model was obtained by applying the classical three shock theory of von Neumann at the triple point (t_0), *i.e.*, in the near vicinity of the triple point, both the pressure and the flow inclination across the Mach stem, were required to match the respective values across the two oblique shocks[103]. Furthermore, a zero curvature constraint was imposed at the triple point for the curved shock (CS), and, this shock was required to be normal at the ramp (t_1).

For ease of integration along the curved shock, the (x, y)-coordinates for the curved shock were obtained in parametric form $(x(t), y(t))$, with the free parameter ($t \in [0, 1]$) attaining a value of zero at the triple point, and a value of unity at the ramp, as shown in Figure 2.6.

At the triple point, the flow deflection $\delta(t_0)$ was obtained by solving the fol-

lowing algebraic form, which effectively requires the difference in pressures, on either side of the slip stream, to be zero:

$$\begin{aligned} 0 = p_\infty \, \xi \left(\gamma, M_\infty, \theta \left(\gamma, M_\infty, \delta(t_0), 0\right)\right) \\ - p_{\infty,2} \, \xi \left(\gamma, M_{\infty,2}, \theta \left(\gamma, M_{\infty,2}, \delta(t_0) + \delta_1, 4\pi\right)\right). \end{aligned} \tag{2.3}$$

Here, the composite function, ξ, gives the local pressure ratio across a shock wave[104]:

$$\begin{aligned} \xi &= \xi \left(\gamma, M_{(u)}, \theta\right) \\ &= \frac{2\gamma\beta - (\gamma - 1)}{\gamma + 1}, \end{aligned} \tag{2.4}$$

with β as defined in (A.10), and θ as given by (A.12).

Hence, for a given value of free-stream Mach number, (2.3) can be readily solved for the initial flow deflection, $\delta(t_0)$, near the triple point. The curved reflected shock can then be obtained as a cubic form ($y(t) = \Sigma_i c_i (x(t))^i$), by solving its constraint system, $0 = f_2(c_i, x_4)$, for the four coefficients, $(c_i, i = 0 \ldots 3)$, and the x-coordinate ($x_4 = x(1)$), where it impinges on the ramp:

$$f_2 = \begin{bmatrix} c_0 + c_1 x_3 + c_2 x_3^2 + c_3 x_3^3 - y_3 \\ c_0 + c_1 x_4 + c_2 x_4^2 + c_3 x_4^3 - x_4 \tan \delta_1 \\ c_1 + 2c_2 x_3 + 3c_3 x_3^2 - \tan(\theta(0)) \\ c_1 + 2c_2 x_4 + 3c_3 x_4^2 + \operatorname{cotan}(\delta_1) \\ c_2 + 3c_3 x_3 \end{bmatrix} \tag{2.5}$$

Here, the point $(x_3, y_3) = (x(0), y(0))$ is found from the intersection of the straight Mach stem (an assumption) with the incident, leading-edge shock. However, as

with the slip layer deflection, the angle of this leading-edge shock, θ_1 is a function of M_∞, which is not known a priori (we are in fact searching for the value of M_∞ at which the inlet will self-start). In practice, this is easily remedied with a few iterations over the free-stream Mach number; the overall procedure is thus started with an initial guess value of M_∞=M_D in the following equation,

$$0 = -A_t + (y_2 - y_3)\frac{A_K}{A_\infty}(\gamma, M_\infty) + \int_{\mathrm{CS}} \mathrm{d}A_s \tag{2.6}$$

This condition follows directly from quasi steady flow assumption; it simply states that the the net sum of mass fluxes across the control surfaces is zero. The first term denotes the throat area, the second term accounts for the Kantrowitz area contribution at the short Mach stem (modelled as a straight normal shock), and the last term represents integration over the curved shock segment. The general expression for this integral is given below. It is suitable for curved shocks occurring in ramp intakes.

The CS integral was split into two separate parts, one for the supersonic branch, $t \in [0, t_s]$, and the other for the subsonic branch, $t \in (t_s, 1]$:

$$\begin{aligned}\int_{\mathrm{CS}} \mathrm{d}A_s &= \int_0^{t_s} \frac{\mathrm{d}s}{\mathrm{d}t} \sin(-\alpha) \frac{A_K}{A_{(d)}}\big(\gamma, M_{(d)}\big)\mathrm{d}t \\ &+ \int_{t_s}^{1} \frac{\mathrm{d}s}{\mathrm{d}t} \frac{A_K}{A_{(n)}}\big(\gamma, M_{(n)}\big)\mathrm{d}t \end{aligned} \tag{2.7}$$

Here, $\mathrm{d}s/\mathrm{d}t$ as plotted in Figure 2.7, is the rate at which the local shock area (arc length) changes with respect to the integration parameter, t:

$$\frac{\mathrm{d}}{\mathrm{d}t}s(t) = \sqrt{\left(\frac{\mathrm{d}}{\mathrm{d}t}x(t)\right)^2 + \left(\frac{\mathrm{d}}{\mathrm{d}t}y(t)\right)^2} \tag{2.8}$$

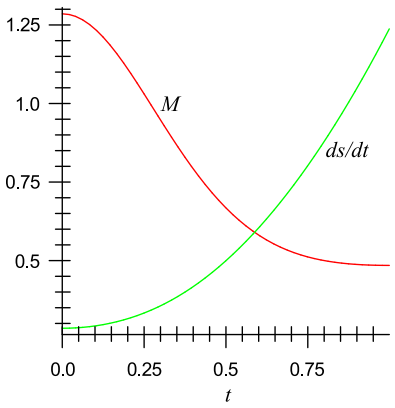

Figure 2.7: $M(t)$—local Mach number downstream of the shock. ds/dt—rate at which the local shock area (arc length) changes with respect to the integration parameter, t.

The angle, α (plotted in Figure 2.8), describes the local inclination, relative to the shock, of the infinitesimal stream-tube for which the Kantrowitz area is being integrated:

$$\alpha(t) \equiv \theta(t) - \delta_1 - \delta(t)) \tag{2.9}$$

Here, $\theta(t)$ (plotted in Figure 2.8) is obtained in parametric form using the following identity:

$$\theta(t) \equiv \arctan\left(\frac{\mathrm{d}y/\mathrm{d}t}{\mathrm{d}x/\mathrm{d}t}\right), \tag{2.10}$$

The aerodynamic shock angle is represented in (2.9) by the sub-expression $(\theta(t) - \delta_1)$, and $\delta(t)$ is the local change in flow inclination across the curved shock.

For the subsonic branch, the normal component of the Mach number upstream of the curved reflected shock is given by $M_{(n)} = M_{\infty,2}\sin(\delta_1 - \theta(t))$, with $M_{\infty,2}$ obtained using (A.9). The Mach number downstream of the curved reflected shock $M_{(d)}$ (plotted in Figure 2.7) is also given by (A.9).

Here, as a check, the value of $M_{(d)}(t)$ for $t = 0$ must correspond to the triple point solution. Similarly, $M_{(d)}(1)$ must correspond to the value behind the normal

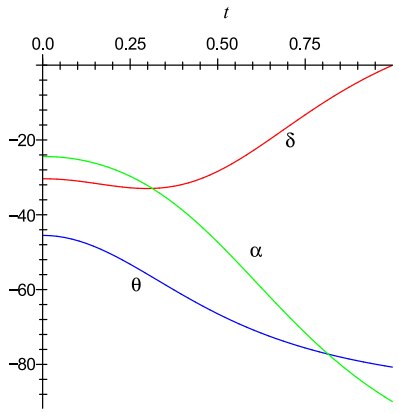

Figure 2.8: $\alpha(t)$—local inclination (degrees) of the infinitesimal stream-tube for which the Kantrowitz area is being integrated, as measured relative to the shock; $\theta(t)$—angle of the curved reflected shock, as measured relative to the x-axis. Note, this angle differs from the aerodynamic shock angle obtained from (A.12), by an amount $delta_1$. $\delta(t)$—local change in flow inclination across the shock.

shock wave impinging at the ramp. Also note that, in general the Mach number distribution along the cowl shock wave may be highly non-uniform, even with uniform flow upstream of it. *Hence, use of a single averaged value with a straight segment shock may not properly capture the physical essence of multidimensional effects, and it may also explain the discrepancies reported in literature.*

To obtain the critical value of Mach number, (2.6) is solved for M_∞, by iteration; a value of 3.378 was thus obtained for Mach number at which the (M3IoS0.5) inlet should self-start according to this revised analytical model. This prediction was deemed to be a significant improvement over the earlier model, as it compared well with the ideal flow CFD result (3.35).

Note that the actual shock profile, as obtained from the above model, is drawn in Figure 2.6; the result compares well against the solution obtained from the CFD simulation as shown in Figure 2.5.

Based on these comparisons, the curved shock model with the stated assump-

tions was deemed to be valid within the present scope. We note that it was also possible to apply a more sophisticated approach which modelled the curvature of the Mach stem; however, given the small size of the stem (which depends on M_∞-M_D difference), and the level of accuracy already attained with the above simpler model, the additional complexity and concomitant effort was deemed unnecessary. Lastly, a higher order model may be required if the starting Mach number value, M_∞, deviates greatly from the design value, M_D. In this connection, it may be necessary to obtain two separate shock profiles for the supersonic and subsonic parts; the rest of the analysis and the integration procedure should still hold.

2.4.4 Simulation Model for the Tunnel Start-up

The analysis presented above relied on a rather simplified situation, namely, that the initial flow development follows a quasi-steady process, such as would result from a gradual unblocking of an initially blocked exit. However, the actual flow in a wind-tunnel involves starting of the nozzle, and depending on the design of the tunnel, this process can be classified ranging anywhere from quasi-steady to mildly unsteady. In the case of pulse facilities, this process may even be classified as highly unsteady.

A simulation was thus performed to judge the effect of unsteadiness present during the wind-tunnel startup process. This point is relevant only for the M3 tests, because the intake is self starting at M3.5 and M4, as discussed in the previous sections.

Figure 2.9 shows the CFD model for the wind-tunnel nozzle and the test section, along with the M3IoS0.5 inlet model placed inside it.

In this simulation, the far upstream condition was modelled using a pressure boundary at an infinite reservoir. This provided a good approximation for the

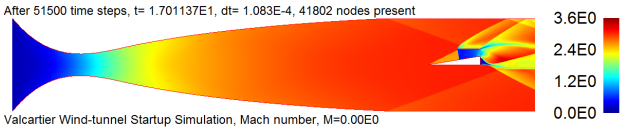

Figure 2.9: SolverII simulation of wind-tunnel: Mach number distribution in the nozzle and upstream of the model is shown.

DRDC trisonic facility[92], which draws from a bag containing 950 cubic meters of air at 1 atm, at room temperature, 300 K. The nozzle was based on a deLaval design matched to the actual tunnel dimensions (with test section 0.6 m in height). The condition downstream of the test section was also modelled as an infinite reservoir, but at a pressure of 1×10^{-5} atm.

Figure 2.10 shows the nozzle shock entering the test section following the nozzle starting process. The flow upstream of this shock is steady having a free-stream Mach number value of three.

Figure 2.11 shows a sequence of frames from the above simulation, immediately following the nozzle startup. The subsequent process verifies the conceptual stages shown in Figure 2.1.

For the M3IoS0.5 case, in the inviscid simulation shown here, a section of the nozzle shock can be seen traversing along the ramp. Eventually, it settles as a bow wave, just upstream of the cowl lip; this process took $\simeq$10 ms. Figure 2.12 shows the uniform steady upstream flow with an unstarted inlet in a Mach three flow. This result demonstrates that the unsteady effects present during the tunnel startup should not lead to intake starting at M3.

Lastly, steady flow results for the three Mach numbers are shown in Figures 2.12, 2.13, and 2.14.

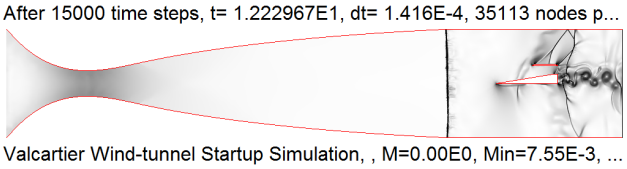

Figure 2.10: Numerical simulation of the wind-tunnel start-up. A started nozzle can be seen with the normal shock approaching the inlet. The flow features are made prominent by using a contrast-enhancement filter over the density gradient field (pseudo-schlieren with circular knife-edge).

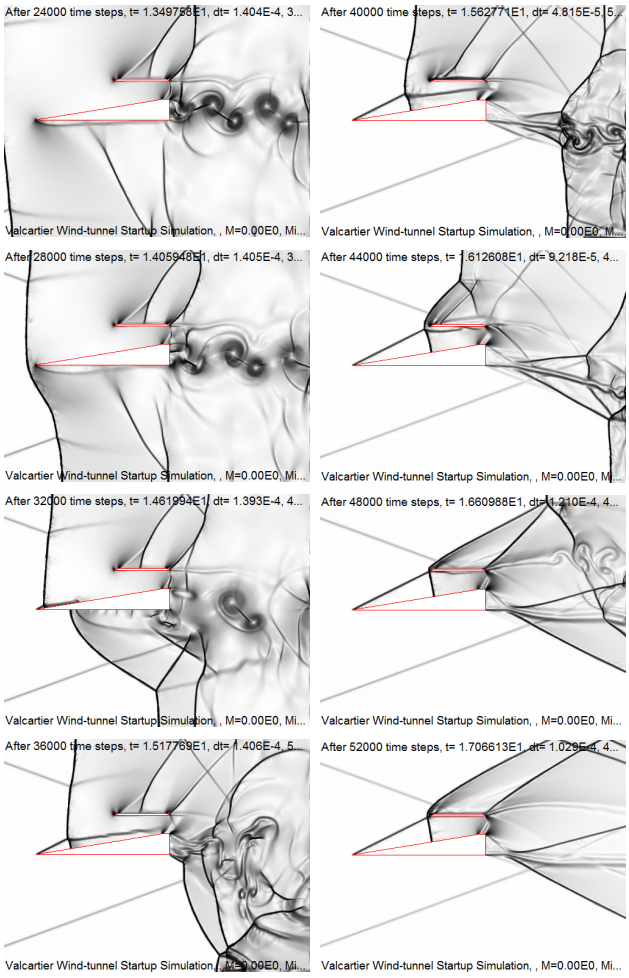

Figure 2.11: Numerical simulation of the tunnel star-up (with enlarged view of the model from Figure 2.10). Motion of the shock as it travels along the ramp is shown. Stable shock location upstream of the cowl lip is shown in the last frame. Relative time, as compared to first frame: $t - t_0 = [0, 2.28, 4.18, 6.46, 7.98, 9.88, 11.8, 13.7]$ ms.

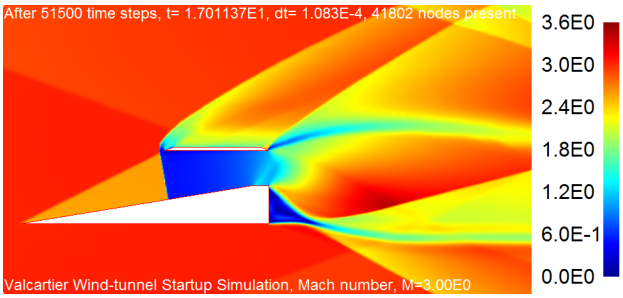

Figure 2.12: Unstarted flow in an inlet (M3IoS0.5) operating at free-stream Mach number of 3.0 (enlarged view of the model from Figure 2.9). Mach number distribution is shown.

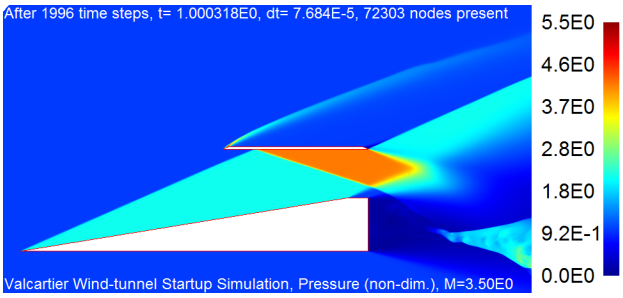

Figure 2.13: Started flow in an inlet (M3IoS0.5) operating at free-stream Mach number of 3.5. Static pressure normalized by free-stream conditions is shown (value on ramp $\simeq 2.15$, and $\simeq 4.16$ at the top wall behind the reflected shock.)

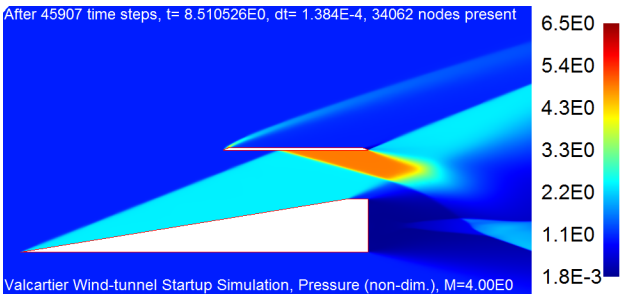

Figure 2.14: Started flow in an inlet (M3IoS0.5) operating at free-stream Mach number of 4.0. Static pressure normalized by free-stream conditions is shown (value on ramp $\simeq 2.35$, and $\simeq 4.90$ at the top wall behind reflected shock.)

2.4.5 Wind Tunnel Model

Based on the above analytical and numerical considerations, a computer aided design (CAD) model (Figure 2.15) was created and manufactured for testing in the DRDC trisonic wind-tunnel at M3, M3.5, and M4, coinciding with the available nozzle blocks. As already indicated, this particular experimental setup was designed as part of a broader research program[100], with the aim to establish experimental capability for testing membrane rupture (§1.3.2.2). In the present context, the aim was to (1) establish the off-design starting characteristics under quasi-steady conditions and (2) to determine the effect of wind tunnel unsteadiness on the starting process. To satisfy the second test requirement, the model was equipped with a pneumatically actuated, and electronically preprogrammed back door (Figure 2.16).

A sectioned view of this CAD model is shown in Figure 2.15. The model contained 43 pressure taps; 15 of these were staggered along the main ramp, at one inch spacing, as shown in Figure 2.15. A fan-like distribution of taps (3×4) was drilled in each side-wall (tap needles are visible in Figure 2.16). The pressure data was collected using a scanning transducer module (model: ESP-32, s/n: 32821, calibrated with a worst case accuracy of ±0.15 %FS over a range of ±5 psi). The data reduction and post-processing was performed using available software[105].

2.5 Experimental Results

Several experimental tests were performed to examine the net effect of wind tunnel flow unsteadiness on inlet starting. The unsteady flow is produced naturally as part of the initial tunnel startup process.

The model was tested at M3, M3.5, and M4 with corresponding Reynolds

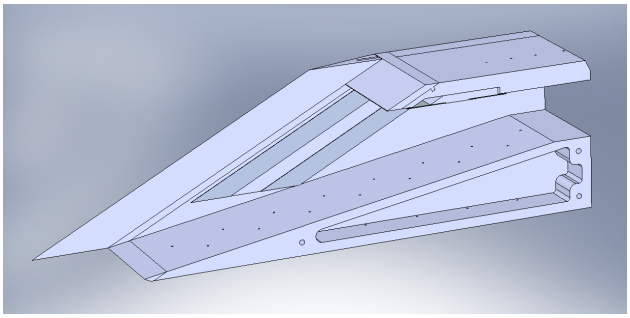

Figure 2.15: Sectioned view of the CAD model. The pressure tap holes are enlarged to enhance the view (actual diameter of the drilled holes was 0.020 inches).

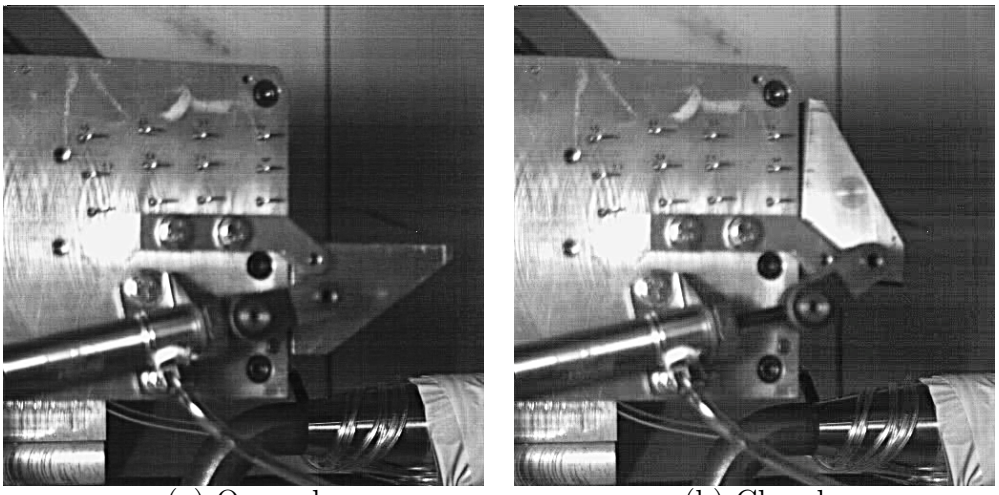

(a) Opened (b) Closed

Figure 2.16: A four-bar "back door" mechanism fitted on the aft side of the model as mounted in the test section. Images are taken from a high speed video footage of the open/close/open cycle: (a) open configuration; (b) closed configuration, holding internal air pressure at M3.5.

numbers of Re7.8, Re6.0, and Re4.7 (in millions per meter). The model size was determined based on blockage considerations at M3 (test-section 0.6×0.6 m^2), with a free-stream capture of 4.75×4.5 in^2, and an overall length of $\simeq 17$ in.

Figure 2.17a shows a sequence of frames sampled at Mach 3 after steady flow was established in the test section. The first frame shows an unstarted inlet with the back door fully open. The back-door was then closed midway through the run (the middle frame) and then opened again (the last frame). Figure 2.18 shows the same process in the form of an animation.* This colour encoded spatial mapping of the four-dimensional data ($p(x, y, z, t)$) allows one to easily recognize global presence of shock waves; *i.e.*, sudden changes in colour occur in a neighbourhood. In this way, presence of a bow-like wave at the ramp with high pressures at the top wall enables one to readily classify the flow as unstarted. When the back door is closed (middle frames), the pressure in the enclosed section jumps (everywhere) to a high value (stagnation pressure aft of the bow shock).

Referring to Figure 2.18, it is seen that the level of unsteadiness, as produced in this test, was insufficient to overcome the steady-state limitation on flow starting at the Mach 3 design-point. The inlet was unstarted after tunnel startup (Figure 2.17a); this ruled out any measurable effects from the initial tunnel transience/unsteadiness, on the final outcome. Referring to Figure 2.18, a close/open cycle of the back door also showed the same result. This M3 test was repeated several times, and the results were found to be consistent, always leading to an unstarted inlet.

Similar tests conducted at M3.5 and at M4 always resulted in a started intake, as shown in Figures 2.17b and 2.17c, respectively. The corresponding animations

*The author favours this format of presentation because of its compactness—arguably, it is also more readily grasped than the traditional plot form. Reader interested in the latter form may refer to Appendix D, pp. 179.

are shown in Figure 2.19 and Figure 2.20. Restarting of the inlet after a mechanically imposed unstart is generally considered to be definitive proof that the inlet will self-start at similar conditions[106].

2.6 Summary

An analytical, numerical and experimental study was performed to understand the flow starting process in a planar, mixed-compression ramp intake.

A novel analytical model was proposed to predict off-design self-starting behaviour; its application was demonstrated for a particular two-shock ramp intake. The calculations were compared with the CFD result lending credence to the assumptions made in the analysis. The proposed method was compared with the traditional models of quasi-steady starting in ramp intakes and agreed more favourably with observations made in the computer simulations.

In the numerical simulations, the self-starting behaviour of the intake was studied at three different Mach numbers using a caloric, inviscid gas model.

Experimentally, the obvious differences in flow configuration at the three Mach numbers were explained in terms of self-starting characteristics. It was observed that the intake self-started at M4, and M3.5, but did not do so at M3. However, the M3.5 case was found to be very close to the self-starting limit (as intended). These results supported the analytical arguments.

It was found that the level of unsteadiness, present during the startup process of the DRDC trisonic wind tunnel, did not have a measurable effect on the intake starting outcome.

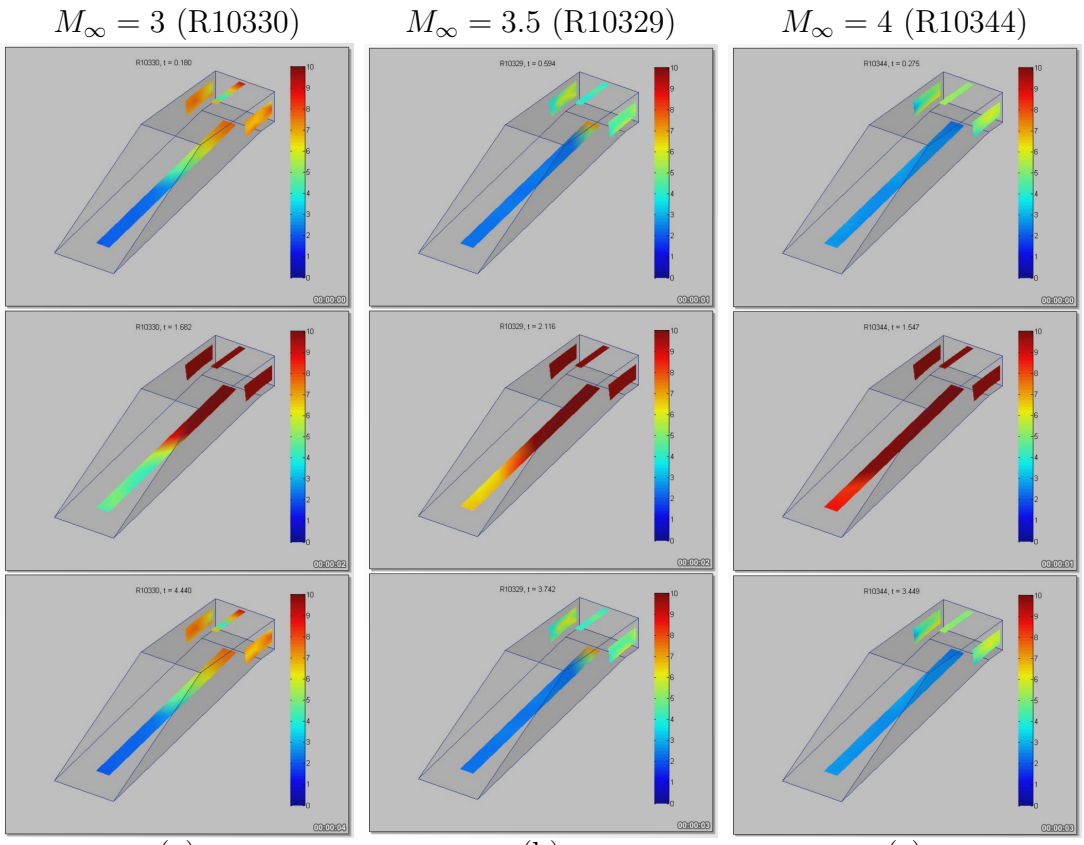

Figure 2.17: Wind-tunnel experiments with back door. Pressure field is reconstructed from discrete readings at the pressure taps. Dark blue signifies low values; deep red indicates high values. Left column: $M_\infty = 3$ (R10330). Middle column: $M_\infty = 3.5$ (R10329). Right column: $M_\infty = 4$ (R10344). Top row: steady result after tunnel startup and *before* door closing. Middle row: state *during* the closed-door operation. Bottom row: steady result *after* door opening. Also see Figure 2.18, Figure 2.19, and Figure 2.20.

M3 experimental data, click here

Figure 2.18: Wind-tunnel experiment at M3 with back door (R10330). Movie shows the normalized pressure field ($p_\infty = 1$), reconstructed from discrete readings at pressure taps shown in Figure 2.15 and Figure 2.16.

M3.5 experimental data, click here

Figure 2.19: Wind-tunnel experiment at M3.5 with back door (R10329). Movie shows the normalized pressure field ($p_\infty = 1$), reconstructed from discrete readings at pressure taps shown in Figure 2.15 and Figure 2.16.

M4 experimental data, click here

Figure 2.20: Wind-tunnel experiment at M4 with back door (R10344). Movie shows the normalized pressure field ($p_\infty = 1$), reconstructed from discrete readings at pressure taps shown in Figure 2.15 and Figure 2.16.

Part II

Singularity in Shock Dynamics

Chapter 3

Shock Wave Propagation

The theory of propagation of shock waves is one of a small class of mathematical topics whose basic problems are easy to explain but hard to resolve.

Peter D. Lax.

3.1 Physical Scenario

In the investigations which follow, we are primarily concerned with the motion of a shock wave, say, inside a channel of non-uniform cross-section. The distinction between shock dynamics and the broader category of fluid dynamics may be considered as one based on the degree of approximation. The broader subject of fluid dynamics deals with the motion of fluid particles or elements and their behaviour in a global sense, including the dynamics of any shock waves that may occur in that fluid. The narrower field of shock dynamics is concerned with "problems where the non-linear geometrical effects play the biggest role and the interactions with the flow behind are not responsible for the major changes in the shock motion" [91]. The dynamic behaviour of a shock wave may itself be quite complex and can lead to highly non-linear phenomena, especially as it relates to wave propaga-

tion through regions of non-uniform flow or through sufficiently large variations in cross sectional area of the channel.

3.1.1 Connection to Starting/Unstarting

As an example, consider the motion of a *right-facing*[*] shock wave entering and traversing a channel; now imagine that this flow evolves under the influence of some transient force, beginning with the initial configuration as shown in Figure 3.1a. Also, suppose that during the early stages of the process, the wave enters and continues its leftward motion in the channel (Figure 3.1b). Subsequently then, depending on the balance of internal and external forces, the dynamic behaviour of the wave may, in general, lead to one of three possibilities: (1) the wave continues leftward (b–d_I–e_I–f_I); (2) the wave slows down and becomes stationary in a metastable sense (c); or, (3) the wave slows down, becomes stationary momentarily (c) and reverses its motion, backward out of the channel (d_{II}–e_{II}–f_{II}).

A schematic of the corresponding wave motion/trajectory is best shown in a *space-time*[†] plot; the reader should briefly glance at Figure 3.2. It shows how the evolutionary process terminates once the transient behaviour subsides ($t \to \infty$). In the steady flow state, the left branch of Figure 3.1 corresponds to Figure 3.2a, and it describes the shock swallowing process (in the sense of flow starting). Similarly, the right branch of Figure 3.1 and its corresponding space-time plot (Figure 3.2c), describe the unstarting[‡] process. The middle plot of Figure 3.2 represents a metastable state possibly occurring between the two possible steady

[*]See the note at the end of §I.9.1 on Page 225.

[†]Also called the x-t plot, or just the wave diagram.

[‡]More precisely, these figures depict failure to start. Unstarting typically refers to a similar process and shock motion, except that the transition initially proceeds from a *fully started* flow state.

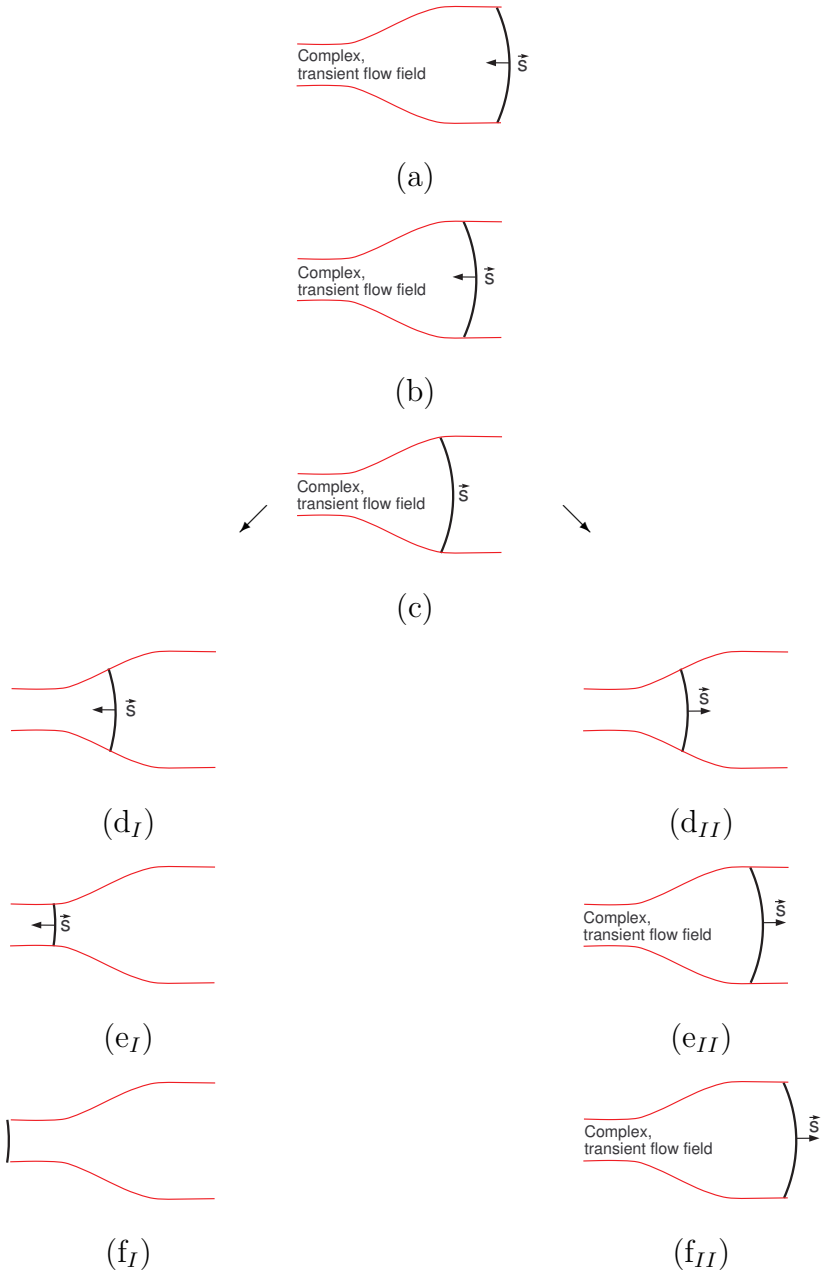

Figure 3.1: Conceptual drawing of the shock swallowing process, leading to either a started flow-field (the left branch), or, slowing down and reversal of the shock motion, leading to an unstarted flow-field (the right branch).

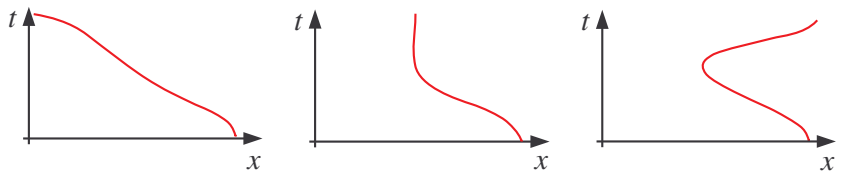

(a) (b) (c)

Figure 3.2: Conceptual space-time diagrams depicting three different possible outcomes following dynamic behaviour of the shock wave. The curve describes the wave trajectory, *i.e.*, its location as a function of time. The inverse slope of the curve is the wave velocity. In (a) the wave enters from the right and exits at the left. In (b) the wave enters from the right, slows down, and becomes near-stationary somewhere in the middle of the channel. In (c) the wave enters from the right, slows down, momentarily becomes stationary, and then speeds up and exits on the right.

state outcomes; it may be anticipated that this state is most likely reached for the critical value of some parameter affecting the final outcome (*e.g.*, critical value of acceleration required for impulsive flow starting). If the parameter attains a super-critical value, configuration (a) is reached; if the parameter attains a sub-critical value, configuration (c) results in the steady state.

The above description helps us in establishing the connection between impulsive flow starting, the nonlinear problems surrounding the shock motion, and the subject of shock dynamics. The modelling of these physical phenomena can be carried out at different levels of approximation. The major assumptions and their justifications are provided in the following section.

3.1.2 Basic Assumptions and Modelling

In what follows, the fluid medium (air) will be approximated as a perfect continuum. Furthermore, where the fluid state undergoes a process exhibiting locally discontinuous behaviour, the domain of interest will be considered geometrically divisible into individual regions, each exhibiting locally smooth behaviour; the

neighbouring regions formed in this way will be delineated and connected by a special boundary representing the discontinuity.

The considered fluid motion is governed by independent conservation laws for mass, momentum, and energy; mathematically, the Navier-Stokes equations written in integral form (also called the weak formulation) are then applicable. In order to study the essence of the primary phenomenon of interest—in this case the transient behaviour of a shock wave—some further assumptions are made regarding the absence of multidimensional effects and absence of diffusive phenomena. Neglecting these phenomena, the entire flow is described by the quasi-one-dimensional Euler equations. Here, the quasi-one-dimensional description follows from neglecting multi-dimensional effects, and the Euler equations follow from neglecting heat conduction and viscous effects.

Geometrically, this description is exact if the cross-sectional area of the channel (and the concomitant flow geometry) follows a symmetric form*. The description is also accurate when the local geometrical curvature is negligible in relation to the global flow geometry. Hence, the categorization embodied within the quasi-one-dimensional Euler equations is applicable in many physical situations, of both steady and unsteady flows. These equations play a particularly important role in the analysis of problems in shock dynamics.

In spite of the aforementioned simplifications, a general solution to the Euler equations is not available[107,108]. It is not surprising therefore that we have to resort to approximate methods[91]. Indeed, even the solutions obtained using the brute force approach of CFD are only approximate to a sense.

Mathematically, the set of three equations (for the three conservation laws)

*Three types of geometries belong exactly to this class: uniform sections with planar symmetry, wedge frustum with cylindrical symmetry, and a conical frustum with spherical symmetry.

forms a coupled non-linear hyperbolic system. For reasons of convenience, depending on the context, this system appears in various (mostly equivalent) forms* in the literature. Here it is sufficient to note that in the shock dynamics literature either the non-conservative form or the characteristic/compatibility relations are the most common starting point (§I.8.2 on Page 220). Simplification of these equations, in certain special cases, enables analytical (exact) solutions; some example scenarios illustrating the physical concepts are described next.

3.2 Review of Known Solutions

In order to facilitate discussion, it is convenient to explain the basic ingredients of this work and the relevant terminology by first reviewing some of the elementary problems closely related to the present case. It is helpful to list the classical simplifications where the above equations do admit analytic solution/treatment. The known solutions typically fall under one of four special classes:

1. quasi-steady phenomena admitting stationary-solutions in the quasi-one-dimensional sense;

2. special initial/boundary conditions leading to *simple wave* solutions in the planar case;

3. homentropic solutions in the planar case;

4. sufficiently symmetric flows exhibiting similarity solutions in the planar, cylindrical, and axisymmetric cases.

*In the fluid dynamics literature, common descriptions include: weak form, strong form, and various non-conservative forms (Appendix I).

3.2.1 Steady-state Example

In the context of intake-related flows, a stationary bow wave standing slightly upstream of an unstarted intake may be considered a special solution belonging to the first class (see Figure 1.3a on Page 5). In fact, this situation serves as an example of shock statics rather than shock dynamics. As already noted (§1.2.1), the classical report by Kantrowitz and Donaldson describes this steady-state solution, which is borne well by experimental evidence[62]. This steady-state result is troublesome in one sense, because it establishes a severe limitation on maximum permissible area contraction which may easily lead to shock swallowing (flow starting).

The Kantrowitz-Donaldson limit (Figure 1.5) describes the behaviour of a Pitot intake under the SoL condition, assuming steady homentropic flow downstream of the shock.* Note that most practical intakes fall in the region between the two curves shown in Figure 1.5, where the intake fails to start under steady flow conditions. Indeed, in practise the steady-state limit on starting is the rule rather than the exception. *It is for this reason that the analysis of unsteady (impulsive) flow starting and a basic understanding of the concomitant shock dynamics phenomenon is of interest.*

3.2.2 Simple Wave Example

Examples of solutions belonging to the second special class include the purely one dimensional motion of a gas next to a moving piston (Figure 3.3). The resulting flow has a special feature such that the disturbances originate from one side only†.

*In this case, $(\partial_t() = 0,\ s_x = 0)$; applicable governing equations are listed in §I.6 on Page 217.

†Prior to the reflection of the wave from the opposite wall, the piston face is the only source of disturbance.

The classical solution then consists of a *simple wave* with constancy of two of the three Riemann variables in the region[2] Art. 29. Intuitively we can imagine that the same situation arises whenever disturbances originate only on one side and propagate inside a semi-infinite cylinder of constant cross-sectional area initially containing uniform, quiescent gas (Figure 3.3). Similar solution also exists for the compression case, except the waves eventually merge* to form a shock wave[109–112] (an interesting historical account is also provided by Courant and Friedrichs[2] Art. 51, pp. 118).

In the case of non-uniform area, new disturbances are continually generated from both sides, *i.e.*, equations (I.76), on Page 219, are non-homogeneous; hence, it follows that a purely one-dimensional simple wave does not exist in the more general case of quasi-one-dimensional flow. However, if the reflected disturbances are weak (*i.e.*, in the absence of significant accumulation over large area variations) then an approximate analogy might be possible. *Use of such an analogy is made later on in the formulation of an approximate theory for shock dynamics.*

3.2.3 Homentropic Solutions

Examples of the homentropic situation include the reflection of a rarefaction wave from an end wall, *e.g.*, as occurs in the classical shock-tube problem (Figure 3.4). During the reflection process, near the left wall there are disturbances emerging from both sides and their interaction leads to a *non-simple* region. The exact solution for this case (for polytropic gases) is known due to Riemann[2] Art. 38. However, this solution procedure does not apply to the general case of non-homentropic flows or to those with geometrical variation. In fact, even for the non-centered

*Incidentally, the P-M compression intake (Appendix B, Figure B.1a) is based on a two-dimensional analogue of this case, with the cowl lip placed at the point of wave coalescence.

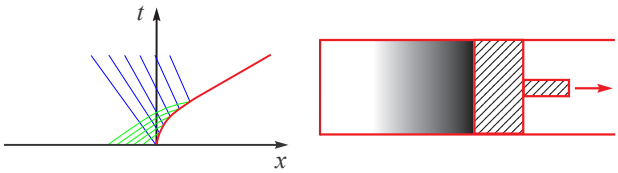

Figure 3.3: Simple wave arising as a result of piston withdrawal. Space-time plot illustrating two families of characteristic curves; *Note that in the present disquisition, green colour designates C_+ family; C_- family is drawn in blue; and piston/particle paths are shown in red.* The simple wave solution is applicable only for sufficiently small time durations, *i.e.*, until reflection of the rarefaction wave occurs at the left wall. Prior to reflection, no disturbances are generated at the far left, and a simple wave presents itself as a fan (infinite set) formed of (infinitesimally weak) individual disturbances originating at the piston face. The constant slope of the individual segments, in the x-t plot, indicates the constant signal propagation speed $((\Delta x_i/\Delta t_i) = (u_i - c_i))$ for the individual disturbances.

rarefaction in homentropic, planar flow case, Courant and Friedrichs suggest that method of finite differences is more tractable! Hence, it follows that if area changes are encountered or if the flow is non-homentropic (both of these conditions are present in the case of intake starting) then even the most simple extensions of the examples discussed here—which may seem very easy to explain—become increasingly difficult to resolve analytically.

The above statements may be used to judge the analytical difficulties which one would encounter in analyzing the flow starting process in supersonic intakes. In that particular case the relevant spatial distributions (of entropy and area) are both non-uniform (A_x and s_x terms in (I.82) on Page 220).

3.2.4 Self-Similar Solutions

The study of self-similar solutions appears to be a branch in its own right; an excellent discussion can be found in Zel'dovich and Raizer[113] pp. 792. Some sample scenarios discussed in the shock dynamics literature are presented here. Take for

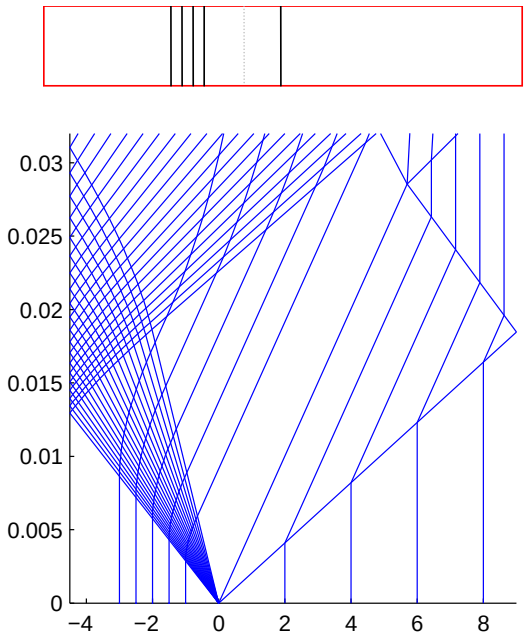

Figure 3.4: Shock tube example—A membrane located at $x = 0$ initially divides the tube into two sections. The left (driver) section is at a higher pressure than the right (driven) section. At $t = 0$ the membrane is *suddenly* removed and a *centered* rarefaction wave thus travels leftward. The *non-simple region* results when the individual (left-facing) waves reach and reflect from the wall (manifest as right facing, curved segments). In the interaction region (curved segments), overlapping disturbances are thus generated, originating from either side. Outside the interaction region, a right facing simple wave results (straight segments again). Finally, the entire flow on the left remains homentropic because the fluid particles originating in the driver section all carry the same level of entropy until such large time as when they pass through the non-uniform shock wave (*i.e.*, $t > 0.031$ in this particular example).

example, the above case of initial flow in a shock tube which is a special case of the generalized Riemann problem; in the absence of end-wall effects (infinite domain), the flow is entirely self-similar. If the waves are initially generated and they move apart indefinitely at constant speeds, in constant area geometry, then no interaction takes place between them, and the self-similar solution scales with time indefinitely.

Whitham[91] points out that an entirely different class of exact solutions is based on special similarity transforms, such that the flow quantities take on the form $t^m f(x/t^n)$ for some constants m and n. These similarity solutions are based on the special simplifying feature that the transformed partial differential equations reduce to ordinary differential equations with independent variable (x/t^n). The blast wave produced as a result of an intense explosion, in connection to the atomic bomb research, was apparently analyzed (*ibid.*) independently in this manner by Taylor[114,115], Sedov, and von Neumann.

Another example, closely related to shock dynamics, is that occurring in the shock implosion scenario (Figures 3.5 and 3.6) where a strong shock wave converges toward an axis of symmetry with quiescent gas ahead of the wave. An exact limiting* solution of this problem is known due to Guderley[116]. Guderley found the pressure at the shock and its velocity related as: $p_2 \propto x^{-2(1-n)/n}$ and $u_s \propto x^{-(1-n)/n}$ with $n \simeq 0.197\,294$ and $n \simeq 0.394\,364$ for cylindrical and spherical shocks in air, respectively. The quoted values are the refined result as found by Butler using an "electronic"† computer (ca. 1954). From a historic viewpoint, the procedural determination of the similarity exponent itself has demanded attention, including Sedov (ca. 1959), Stanyukovich (ca. 1960), and Zeldovich and

*Strictly speaking, the similarity solution only holds in the limit $M_s \to \infty$

†At the time, the term computer was used as a title for a skilled person dedicated to performing laborious calculations by hand.

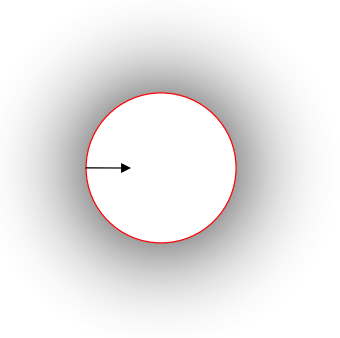

Figure 3.5: Shock implosion problem—A cylindrical (or spherical) wave converges toward its axis (or point) of symmetry, becoming stronger until it collapses at the centre. The wave has singular strength at the centre, and reflects as an outgoing wave which becomes weaker with passage of time.

Raizer (ca. 1967)[113]. In 1974, Yousaf[117] provided the result correct to 12 decimal places. Lazarus (ca. 1982) provides intuitive arguments for seeking self-similar solutions and examines the possibility of similarity solutions with more than one discontinuity[118]. Most recently, Hafner[119] provided the exponent for the implosion case to 30 decimal places!

Inspired by the above results, other closely related solutions have also been devised successfully by various researchers. Jones[120] and later Sakurai[121] considered the problem where a planar shock wave propagates into a non-uniform density field; Sakurai considered a power law distribution ($\rho_1 \propto x^\alpha$, for some constant α) and found the shock velocity relation as: $u_s \propto x^{-\lambda}$, for various values of density distribution parameter α; *e.g.*, with $\alpha = 1$, he found that $\lambda \simeq 0.202\,140$ for a shock wave in air.

Except for the successful cases cited above, broader similarity solutions do not exist in general, because not all shock motions necessarily contain a sufficiently high level of symmetry. Even for the shock implosion problem, the exact solution

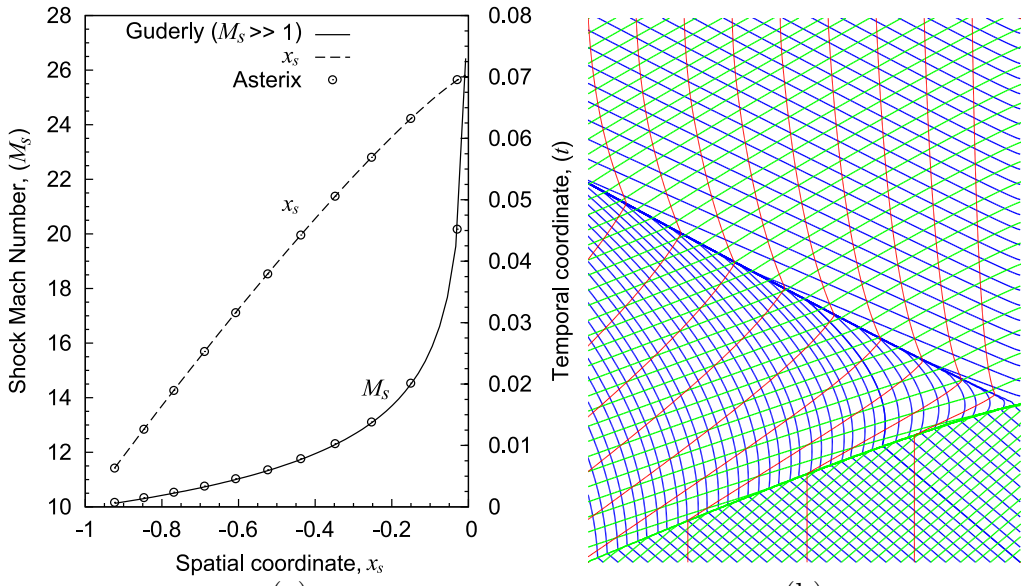

(a) (b)

Figure 3.6: Shock implosion problem. Solution on the left is for initial shock Mach number, $M_s \simeq 10$. Note that in (a) the shock Mach number can be read as a function of its location $M_s = M_s(x_s)$. The shock location can be read as a function of time $x_s = x_s(t)$. The CFD mesh used for this case in Asterix[1] contained 1000 cells, and judging by the comparison, this appears to provide sufficient resolution both for the solution as well as for the extraction of shock trajectory (and the states across it) from that solution. Also note that Guderley's similarity solution is exact/accurate only for $M_s >> 1$, which is why $M_s \simeq 10$ is used here. Comparison between Asterix and the approximate theory of this work will be made for both strong and weak shock waves later on. (b) shows the wave diagram for this problem obtained using the Asterix solution with initial $M_s \simeq 2$. For $M_s = 10$, the result is similar, except the diagram appears squeezed in the vertical/temporal dimension, which makes it difficult to illustrates the following points: (i) The incident shock wave is a right-facing wave (for $x_s \leq 0$, in the hydraulic sense), hence it is formed by the agglomeration of C_+ waves (green); (ii) The reflected wave is left-facing, hence it is formed by the coalescence of C_- waves (blue). Ahead of the incident wave, particle paths (red) appear as vertical lines, because the gas there is quiescent; these particles maintain their location until such time as when the shock arrives. Behind the reflected wave, the flow tends to quiescence in the limit as $t \to \infty$.

only holds true in the limit of strong shocks ($M_s \to \infty$). In the general case of intake flows, neither the geometry, nor the time variant boundary conditions can be considered treatable in the above sense of similarity solutions. Nevertheless, the above known solutions are useful in other practical problems,* but here the simple final expression of Guderley provides a guide or check against the other solution methods (guide for approximate shock dynamics, and check for Asterix[1]). A classical theory in approximate shock dynamics is reviewed in the following chapter, but first it is helpful to summarize the essential points of the present chapter.

3.3 Summary

In studying shock dynamics, one is primarily interested in the shock motion (as opposed to the fluid dynamics). Then, the aforementioned scenarios occurring in intake flows (§3.1.1) may be viewed as special cases of the general phenomena occurring in shock dynamics.

The difficulties in obtaining uniformly valid solutions to the problems in shock dynamics are multi-fold: Firstly, the shock wave motion is subject to *geometric effects* as the wave traverses a channel formed of *non-uniform area* ($A_x \neq 0$). Secondly, the shock strength changes are accompanied by *non-homentropic effects* ($s_x \neq 0$) *downstream* of the wave; the shock wave then readjusts to the disturbances generated downstream of it, leading to a nonlinear interaction between the two[91]. Thirdly, the medium in which the wave travels may in general be non-uniform, *e.g.*, if there are density, pressure, or velocity gradients present in

*Hafner[119] notes that the practical applications relevant to the subject of converging shocks, range from nuclear weapons to inertial confinement fusion, and from synthetic production of diamonds to free-of-contact, in situ destruction of renal calculi.

the fluid *upstream* of the wave. *All of the above effects are present in the intake starting/unstarting phenomena.*

While the exact/general solution to problems in shock dynamics is not known, there exists a well known approximate theory based on the celebrated works of Chester[89], Chisnell[90], and Whitham[122]. The basic Chester-Chisnell-Whitham (CCW) formulation is reviewed next in the following chapter.

Chapter 4

Approximate Shock Dynamics

Make everything as simple as possible, but not simpler.

Albert Einstein

4.1 The CCW Approximation

As motivated in the previous chapter, an exact/general solution to problems in shock dynamics is not known. But, there is a well known approximate theory based on the celebrated works of Chester[89], Chisnell[90] and Whitham[122], which provides analytical treatment of many classical problems in shock dynamics first studied in the 1940s and '50s (§3.2.4). In essence, the CCW approximation provides a relation for the dependence of shock Mach number on the area of the shock wave (or the tube in which the wave travels, in the hydraulic sense). Whitham[91] pp. 270 gives this formula as:

$$\frac{1}{A}\frac{dA}{dM_s} = -g(M_s) \tag{4.1}$$

where, $A(x)$ and M_s are the area and shock Mach number, respectively. $g(M_s)$ is a well behaved monotonically decreasing function given by[91] pp. 269:

$$g(M_s) = \frac{M_s}{M_s^2 - 1}\left(1 + \frac{2}{\gamma + 1}\frac{1 - \mu^2}{\mu}\right)\left(1 + 2\mu + \frac{1}{M_s^2}\right) \tag{4.2}$$

where the quantity μ is the Mach number of the shock relative to the flow behind it, as given by (I.117). We will make reference to the above $g(M_s)$ function later on in connection to (5.9) of the present work. An equivalent relation, obtained by linearizing the governing equations, is given in Chisnell's article[90] pp. 290:

$$-\frac{1}{A}\frac{dA}{d\xi} = \frac{1}{\gamma\,\xi} + \frac{1}{\xi - 1} - \frac{\gamma + 1}{2\{(\gamma + 1)\xi + (\gamma - 1)\}} \tag{4.3}$$

$$+ \left[\frac{2}{\gamma\xi\{(\gamma - 1)\xi + (\gamma + 1)\}}\right]^{\frac{1}{2}} \tag{4.4}$$

$$\times \left[1 - \frac{(\gamma + 1)(\xi - 1)}{2\{(\gamma + 1)\xi + (\gamma - 1)\}} + \frac{(\gamma - 1)\xi + (\gamma + 1)}{2(\xi - 1)}\right] \tag{4.5}$$

where $\xi = f(\gamma, M_s)$ is the pressure ratio across the shock wave given by (I.90). The above equation also appears elsewhere, including a reference text on the subject of shock dynamics[123] pp. 27.

As already hinted, Chester[89] pp. 1298 had already obtained an equivalent result by "linearizing the problem on the basis of small variations in area along the length of the tube" building on his own analysis in an earlier article[124]. In effect, he found the expression for variation in pressure ($\delta\,\xi$) after the shock passage, when the tube consists of two cylinders of slightly different area (δA) connected by a smooth transition section. Hence, in Chester's formulation of the problem, no disturbances exist in the flow behind the shock wave; this is the so called "freely propagating shock wave" description[123] pp. 28. In Chester's small perturbation

analysis, it is consistent to apply uniform conditions at the unperturbed shock location (*i.e.*, in the first cylinder), since the errors introduced in this way would be second order[91] pp. 270. The shock then passes into the second cylinder where the area and hence the shock strength are also uniform. The transition section between the two cylinders also contains linearized wave propagation along $x-(u_2 \pm c_2)t = const$, *i.e.*, the characteristics have been approximated by straight lines. It is this crucial step which leads to a sign change of the area variation term. In this analysis, the situation is rightfully analogous to the sonic flow (choking) which in steady flow occurs only at the throat. We will return to this discussion below in connection to Friedman's work[125].

Following Hayes'[126] labelling, the general approach given above is now widely known as the CCW theory in the literature. But the CCW theory, as such, was popularized by Whitham[122] who offered its derivation as a simple and beautiful, "characteristic rule" which agreed with the earlier formulae obtained by Chester[89] and by Chisnell[90] using different approaches. The resulting approximations provided remarkably accurate solutions for the shock implosion problem and as a result, the Guderley solution served as a benchmark case in the approximate shock dynamics literature for some time; most early works in the field discuss/compare approximate results with this known solution. Aside from the work on the shock implosion problem, there exists a large amount of literature on the general subject of approximate shock dynamics; the seminal papers, and perhaps the most cited works on the subject, can be found in the annals of the Journal of Fluid Mechanics. All of the literature relevant to the present work, refers directly to Whitham's "characteristic rule."

4.2 Whitham's Characteristic Rule

The characteristic rule states[122] pp. 340:

> First the appropriate equations of motion for the flow are written in characteristic form. For example, for a non-uniform tube we have
>
> $$dp + \rho c du + \frac{\rho c^2 u}{u + c} \frac{dA}{A} = 0$$
>
> on a positive characteristic $dx/dt = u + c$, where p, ρ, u, and c denote the pressure, density, particle velocity, and sound speed, respectively. Then the above characteristic relation is applied (quite illogically it may seem) to the flow quantities at the shock wave. But these quantities are all known in terms of the shock strength from the Rankine-Hugoniot shock relations. Thus on substitution in the characteristic equation, an equation for the variation of the shock strength is obtained. This gives a first-order equation for M_s as a function of A which can be integrated immediately.

In effect what is suggested in the above passage is to replace (p, ρ, u, c) by (p_2, ρ_2, u_2, c_2) downstream of the shock. For a right facing shock wave, the C_+ relation should be used. For a left facing shock wave, the C_- relation should be used. The state "2" quantities should be connected to the state "1" quantities through Rankine-Hugoniot jump conditions (§I.9 on Page 222). After some algebraic manipulations, the procedure yields an expression of the form $dM/f(M) \sim dA/A$ as given by (4.1). Admittedly, the beauty of the characteristic rule lies not in the novelty of the final expression, but in the simple, yet effective manner in which Whitham derived it; (*quite illogically it may seem*, in his own words[122]).

In concluding his general remarks, Whitham notes: "it should be said that the discussions in this paper still fall short of a full understanding of all the questions involved; it is still not completely clear to what extent the unexpected accuracy of the results in some cases should be ascribed to coincidence." A similar sentiment is also expressed much later on in his book[91] pp. 272, where Whitham notes that after the quick derivation (referring to the characteristic rule) occurred to him, he had hoped for a full analysis of the approximation based directly on the governing equations, and that so far it had not been completed!

However, the above $A(M_s)$ relation proved almost trivial to extend to a variety of other cases, as discussed below. And, because the final formula agreed with the earlier results obtained by Chester and Chisnell, which had worked so well for the shock implosion problem, taken together these results garnered much attention. So much so that a separate line of investigations can be traced in literature; in the quest to achieve higher levels of accuracy, a steady stream of articles appears since the 1960's. These latter papers deal mainly with justifications and attempts at perfecting the basic technique, especially for application to physical scenarios which it was not initially intended to address.

4.3 Modifications and Corrections

In integrating Chester's solution, Chisnell initially made the same assumption regarding "freely propagating shock wave"; he then attempted to include the modifying effects resulting from the elementary interactions between the backward ("reflected," or C_- and C_0) waves and the area variation downstream of the shock wave. These interactions lead to ("re-reflected," or C_+) disturbances, which Chester incorporated as correction or modification in the original description. He

found that the net effect of these re-reflections *i.e.*, the *total* modification to CCW was almost negligible for the implosion problem. It is also generally accepted that the correction procedure (especially, higher than first order, *i.e.*, beyond the first re-reflection) renders the CCW impractical; the procedure would be akin to applying the method of characteristics by hand. It may be said that the success of the CCW is attributable to the simplicity of the characteristic rule, rather than the rules of the characteristics. Nevertheless, the works dealing with corrections and extensions help understand the limitations of Whitham's rule and also enable treatment of broader problems. These works are summarized next.

4.3.1 Sonic Flow Singularity

From the outset, a minor question existed on a possible discrepancy between Whitham's characteristic rule and the original description of the flow by Chester. In Chester's formulation, the case of sonic flow $u_2 = c_2$ leads to a singularity* (which he likens to the familiar flow choking process). Yet the same difficulty does not prevent successful application of Whitham's characteristic rule in the implosion problem, where the sonic situation arises for $M_s \simeq 2$ for air ($\gamma = 1.4$).

On Whitham's suggestion, Friedman[125] studied the problem and found a "non-linear" correction to the linearized solution of Chester. Chester was aware of this issue and actually gave an extended account of the scenario leading to the singular behaviour. However, the original analysis by Chester, as well as the subsequent treatment by Friedman, both deal only with the singularity in the negative characteristic (*i.e.*, $u_2 - c_2 = 0$, which is immaterial for the characteristic rule)†. In fact, the above omissions appear as deliberate acts with self-criticism[89]

*More precisely, the linearized equations contain a possibly singular term $(c_2^2 - u_2^2)$ in the denominator of the area coefficient term.

†Refer to (I.80) and recall that for a right facing shock wave, it is the positive characteristic

pp. 1300 and hence, the present historical account must not be construed as an indication of mathematical error made by these authors. In reality, the flows which were examined at the time did not contain moving gas ahead of the shock wave, and with that simplification it would have been difficult to anticipate the case ($u_2 + c_2 = 0$).

Not surprisingly then, Friedman found out that the characteristic rule, as obtained by Whitham, remains unaltered as a result of his non-linear treatment of the backward disturbances in Chester's solution. Hence, the above analyses do not address the possible singularity present in the "characteristic rule" which we will consider. In fact, both authors note that it would be impossible! It will be shown in the following chapters that there actually exists an infinitely large set of conditions which would lead to singular behaviour of the characteristic rule. Furthermore, these singularities should not be considered as those belonging to the 0/0 family, which are typically associated with flow choking as encountered in steady-flow situations at the throat (where $dA = 0$).

4.3.2 Incorporating Boundary Conditions

Rosaciszewski[127] provides a generalization to include downstream boundary conditions and also provides formulae for treating flows in ducts with porous walls. Under common assumptions with relevant simplifications, he concludes that his method reduces to Whitham's characteristic rule. The main contribution then appears to be the integration of two neighbouring C_+ characteristics to determine the net variation along the shock direction. According to[117] the integration of two neighbouring characteristics was also considered by Oshima (1965) (his results also appear in an appendix to Ref.[128]). The integration is performed start-

which plays the important role in Whitham's rule.

ing from a downstream boundary where the flow conditions are prescribed. In the present scenario, the flow between the wave and the downstream boundary is not known/modelled sufficiently. Even with the higher order corrections offered, the final expressions in[127] agree with Whitham's result, which exhibits singular behaviour in the present case.

4.3.3 Non-uniform Upstream Medium

The non-uniform medium upstream of the shock may be classified into three separate categories: The first (classical, most well known) case is that of a quiescent gas with static density variations. The second (less classical, but still well known) case is that of moving gas, albeit with steady state prescribed as a known solution upstream of the shock wave. The third case (considered in the present work) arises due to both spatial and temporal variations in the flow upstream of the shock wave. The literature dealing with the first two cases is reviewed in the following subsections. The third case is considered in the following chapter.

4.3.3.1 Quiescent Gas

Hayes[126] considers the shock propagation in a medium with exponentially varying density, and refers to Sakurai's work[121], who had studied a power-law distribution. Hayes also obtains a similarity solution for his problem and compares the result with CCW. He notes that in contrast to the shock implosion problem (where the results are "so excellent as to be uncanny"), for the exponential density distribution the similarity exponent from CCW approximation is in error by about 15%. With Sakurai's power-law[121] the error is somewhat less (about 10%).

4.3.3.2 Non-quiescent Gas, Steady Flow

The case of a shock wave propagating in a channel with non-uniform area and with steady upstream flow pre-established in the channel is discussed in a reference* text by Han and Yin. Their derivation follows Whitham's characteristic rule to the letter, *i.e.*, they begin by substituting the parameters downstream of the shock (state 2) into the C_+ characteristic relation. The novel idea is to employ the *steady homentropic relations* for the conditions upstream of the wave (state 1). Their final result is as follows[123] pp. 167:

$$\begin{aligned} dM_s &= G_1 dm_1 \\ \frac{dA}{A} &= \frac{m_1^2 - 1}{1 + \dfrac{\gamma - 1}{2} m_1^2} \cdot \frac{dm_1}{m_1} \end{aligned} \tag{4.6}$$

where, m_1 is the upstream flow Mach number, and,

$$G_1 = \left[\frac{\dfrac{m_1}{T} + \left(\dfrac{\gamma - 1}{2} \right) \dfrac{m_1 m_2}{T} - \dfrac{m_2}{S} - \left(\dfrac{m_1^2 - 1}{m_1} \right) \dfrac{1}{T} \left(\dfrac{m_2}{m_2 + 1} \right)}{\dfrac{2m_2}{(\gamma + 1)S} \cdot \left(1 + \dfrac{1}{M_s^2} \right) + \dfrac{4M_s}{2\gamma M_s^2 - (\gamma - 1)}} \right] \tag{4.7}$$

and,

$$\begin{aligned} T &= 1 + \frac{(\gamma - 1)}{2} m_1^2 \\ S &= \frac{2(M_s^2 - 1)}{(\gamma + 1) M_s} + m_1 \end{aligned}$$

The above equation for dM_s will be compared later on with the more general result of this work (5.8) on Page 92. It will also be discussed in another connection

*Ref. [123] may be considered *the* reference text on the subject of shock dynamics as of 2008.

in §5.4.8 on Page 105. In the following section we return to the discussion of quiescent gas ahead of the shock wave. A set of corrections for both uniform and non-uniform upstream states was found in the literature and these are reviewed next.

4.3.4 Yousaf's Corrections Based on Similarity Solutions

A remarkable series of articles appears during the 1970's and '80s written by a Canadian mathematician at the Laurentian University in Sudbury, Ontario. Yousaf appears to have been directly influenced by (and collaborated with) Chisnell. In the first paper of the series (ca. 1974), Yousaf[117] gives a thorough treatment of the shock implosion problem, presenting an exact formulation of the strength of the disturbance overtaking the shock. He states: "The similarity solution is used to find the five interaction terms at all points of the flow. This work confirms that when the strength of the overtaking disturbance is known the CCW approximation may be modified to become an exact theory."

As hinted in the previous chapter, it is in the course of this investigation that Yousaf finds the Guderley/Butler exponent to 12 decimal places; he then incorporates non-local information from the similarity solution into the CCW formulation. In this way he determines the correction to be made to CCW, so that in the limit for strong shock waves, the solution agrees (to all 12 decimal places) with Guderley's exact solution.

Using the same approach, in the second paper (ca. 1978), Yousaf[129] successfully addresses the larger discrepancy ($\simeq 10\%$) reported by Sakurai between CCW and his similarity solution. For the strong shock case, the CCW is corrected to match the exact similarity solution. In a followup article coauthored with Yousaf, Chisnell provides an approximate but somewhat more "tractable" analyitical ap-

proach. He states: "the simple treatment of the overtaking wave thus provides a significant improvement to the freely propagating description of the shock motion."

In the third paper (ca. 1982), Yousaf[130] addresses the discrepancy for the Sedov problem (an explosion in a medium of uniform density). He notes that the error in the propagation parameter is $\simeq 70\%$. Using, again, the similarity solution, he finds the correction to be applied to CCW.

In the fourth paper (ca. 1985), Yousaf[131] applies CCW to the problem where the shock propagates into a medium with an exponential density distribution. Recall from previous chapter that Hayes[126] found a similarity solution to this problem. Once again, using the available similarity solution Yousaf finds the correction to be made to CCW so as to render the latter "exact" for the case of a strong shock. He later provides an approximate method addressing the same problem[132].

In the final article (ca. 1988), printed posthumously, Yousaf[133] returns to the Sedov problem, starting with the results given in the original three page article[130]. He expands the original discussion and analyses the various interactions occurring downstream of the shock wave produced by an intense explosion. Based on the above articles, his main conclusion is that where there is a mutual cancellation of the interacting waves, the CCW theory is accurate. In particular, Yousaf reports that the interaction which has most influence in the strong explosion problem is that of C_+ with the C_0.

In summary, it may be said that with his mathematical ability Yousaf virtually lends the CCW theory the only bona fide set of corrections reported in the literature. As hinted above, his unique approach involves incorporating nonlocal information from the exact similarity solutions into the approximate CCW theory.

In effect, he analyses the interactions among the various waves downstream of the shock, as well as their interactions with the area change. The net effect on the shock is then determined by finding the exact strength of the "modifying disturbance" at the shock. However, this description should not be taken as a magical solution that is universally practical and applicable to the arbitrary case. It is mainly useful in the limit of strong shocks where similarity solutions are available. In his own words, "of course, the problem of finding correction to other problems remains." *Hence in general CCW remains, and should be considered as, in what follows, an approximate theory.*

4.4 Summary

The basic approach in the CCW approximation theory leads to a differential relation of the form $dM/f(M) \sim dA/A$ as given by (4.1). For the simplest case of uniform, quiescent gas ahead of the shock, a closed form solution (integrated result) is available due to Chisnell. The approximation discards information generated downstream of the shock, either as a result of boundary conditions, or due to interaction of the disturbances with each other and with the area change. This is described in the literature as the "freely propagating shock wave."

The original CCW model also does not take into account any variation of parameters in the upstream flow, which may be classified broadly as either steady (spatial variations) or unsteady (spatial and temporal variations). The former case has been discussed by various researchers including Sakurai, Hayes, Yousaf, and Han and Yin; their corresponding extensions to the respective cases are well known. For instance, the case of non-uniform (quiescent) gas upstream of the shock wave falls under the first category; a typical scenario then includes density

variation upstream of the shock wave as treated by Hayes, Sakurai, and Yousaf. A higher extension including non-uniform moving gas (steady flow) ahead of the shock wave is provided by Han and Yin and it also falls in the first category; a typical scenario then includes shock propagating into an existing steady homentropic stream in a variable area channel.

The present work further extends the above cases to include both spatial and temporal variations upstream of the shock wave. This extension is required in the study of unsteady intake flows, where the upstream (inflow) boundary condition may in general be time-variant. These extensions are considered next in the following chapter.

Chapter 5

CCW with Lifting Isentrope

It can scarcely be denied that the supreme goal of all theory is to make the irreducible basic elements as simple and as few as possible without having to surrender the adequate representation of a single datum of experience.

Albert Einstein

5.1 Review of Ideas

This chapter builds further on the concepts already presented in the preceding two chapters; the key elements which were discussed, include: (1) the basic notion of shock dynamics, (2) connection between shock dynamics and unsteady flow phenomena in intakes, (3) the classical CCW approximation for shock dynamics, (4) the known extensions and generalization of the basic CCW theory, and (5) the idea of using an exact or approximately known solution as a guide to extend the model. Compounding in this manner, the basic CCW model is extended to the case of unsteady non-uniform flow upstream of the shock wave.

For the sake of completeness, the relevant assumptions within the CCW framework are as follows:

(i) The problem mainly concerns shock propagation in a channel featuring smooth area variation (either converging or diverging). The shock is considered to be freely propagating, independent of any interactions among the disturbances which are generated downstream of it.

(ii) Initially, before the shock enters the channel, there may be some nonuniform flow inside the channel; in what follows, this flow is considered homentropic. At first sight, it may also appear in the theoretical developments below that the treatment is limited to quasi-steady flows; this is strictly not true, as will be established later on in the analysis. Once that condition is relaxed, it will be shown that it may also be the case that the parameters upstream of the shock are changing *rapidly* due to time-varying boundary conditions. Such would be the case if, say, the channel was subjected to accelerative forces causing its rapid motion (Figures 3.1 and 3.2 illustrate the physical scenario on Page 57).

(iii) In the present context, the upstream boundary condition and the initial shock strength must also be given (*i.e.*, specified as part of the problem statement).

From the preceding chapter, we know that the above problem is amenable to some analysis, following the theoretical framework by Whitham outlined on Page 74. Such an analysis will be carried out in the next section, however to facilitate discussion, it is convenient to offer some clarifications first.

5.1.1 Necessary Idiosyncrasies and Terminology

The shock motions which are considered here may generally be quite complex; for example, a right facing wave does not necessarily travel rightward! To avoid confusion, a few important notes should thus be made. Without any further loss of generality, we may limit the discussion to a right-facing shock wave, *i.e.*, *all shock waves considered here are right-facing.* In derivations where convenient,

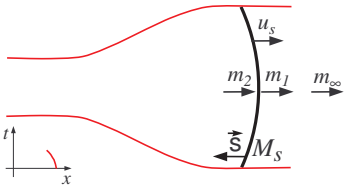

Figure 5.1: Problem definition. The small case letters denoting local flow Mach numbers m_1, m_2, and m_∞ indicate that these are *signed* quantities. In this picture, all three quantities carry a negative sign since the conceptual flow as depicted here is leftward. Also, in the inset wave diagram as shown, the shock is moving leftward and $u_s < 0$. Nevertheless, it is a right-facing wave because the flow enters the shock wave from the right, and hence, where applicable the upper sign should be used in the general equations (§I.8, §I.9.1).

the appropriate symmetry will be preserved*. Furthermore, in the lab frame of reference, the right-facing shock wave may be moving either to the left or to the right†. Also note, where no confusion exists in the context, the "±" signs are incorporated to indicate relations for $C_\pm$ (§I.8); in applying the characteristic rule (§4.2) the same sign convention holds for the right- and the left-facing shock waves, respectively.

We distinguish between the terms: *homentropic* and *isentropic*. The former implies conservation of entropy along all characteristics in regions of smooth flow, $C_\pm$ as well as C_0. The latter implies conservation of entropy along C_0 only. In either case, if a characteristic crosses a shock wave, the discontinuous jump in entropy value must be taken into account using the Rankine-Hugoniot relations (§I.9). The problem statement is defined next.

*In general, to obtain expressions for a left-facing shock, one may simply reverse the signs of m_1 and m_2.

†For further details see the note at the end of §I.9.1 on Page 225.

5.2 Problem Definition

Referring to Figure 5.1, the problem statement defines area $A(x)$ of the geometry, the initial states, *i.e.*, shock Mach number $M_s(x)$ at $x = x_i$ or $x = L$, the *signed* Mach numbers, m_1 upstream of the shock, and in the free stream $m_\infty(t)$, and the free stream speed of sound c_∞.

5.2.1 Relation to Previous Works

In the final formulae which are obtained below, any of the special parameters may be set to their trivial values if a simpler problem is to be studied. For instance, setting $m_1 = 0$ and $m_\infty = 0$ with fixed boundary conditions $\partial_t(m_\infty) = 0$, should recover the original relations by Whitham (4.1) on Page 71. For a right-facing wave m_2 and u_s will then be positive quantities. Similarly, the formulae obtained below will be equivalent* to the Han and Yin result (4.6) on Page 79, if we specify $\partial_t(m_\infty) = 0$ with $m_\infty = const$ and $A_\infty = const$, so that m_1 is automatically determined as $m_1 = f(m_\infty, A_1/A_\infty)$. These statements are offered in anticipation of the results which will follow, and to explain similarities and differences from previous works; these statements will be further clarified as we proceed.

5.2.2 Accelerative Motion

To accommodate accelerative motion, a body force term, $f(t)$, representing mass-specific force directed along x-axis is included in the model; its usage is optional, and formally independent of any specifications about $m_\infty(t)$ or the upstream boundary condition. In the physical context of present work, however, these two

*Although apparently very different, under common set of assumptions, the expression are equivalent.

quantities are coupled because any acceleration of the intake body must also lead to changes in m_∞. The functional relation is: $\partial_t(m_\infty) = f/c_\infty$.

The extension to the classical CCW model is presented next.

5.3 Applying Whitham's Characteristic Rule

With the above assumptions, following Whitham's arguments, we may begin with the appropriate characteristic relation (I.78) taken from Appendix I. To describe the shock dynamics we apply the C_+ relation to flow immediately behind the shock wave:

$$C_\pm : \qquad \frac{1}{c_2}\mathbf{D}_\sigma\left(u_2\right) \pm \frac{1}{\gamma p_2}\mathbf{D}_\sigma\left(p_2\right) \pm \frac{m_2}{m_2 \pm 1}\frac{\mathbf{D}_\sigma\left(A\right)}{A} = \frac{f}{c_2}. \tag{5.1}$$

Here, the area differential is to be evaluated using $\mathbf{D}_\sigma\left(A\right) = u_s\partial_x(A)$. In essence, we are seeking a differential relation to be integrated as an initial value problem (IVP) along the shock wave trajectory. In this case, the $\mathbf{D}_\sigma\left(\right)$ operator clarifies the intent, and once that step is taken, this formalism may be dropped safely in favour of the more usual notation without causing any confusion. Henceforth, in dealing with an already specified unique direction, it is unnecessary to indicate the direction each time. The above equation is customarily written in the following form, which makes it easier to compare with the results found in literature[123] Han and Yin, pp. 65.

$$C_\pm : \qquad \frac{1}{c_2}\frac{du_2}{dt} \pm \frac{1}{\gamma p_2}\frac{dp_2}{dt} \pm \frac{m_2}{m_2 \pm 1}\frac{1}{A}\frac{dA}{dt} = \frac{f}{c_2}. \tag{5.2}$$

The goal now is to substitute shock Mach number M_s in this expression where appropriate/possible, so that a differential expression of the form $d_t(M_s) =$

$f(M_s)/A\ d_t(A)$ is sought. In the derivation below, the lone body-force term on the right hand side is left intact, as it need not be simplified any further; the same applies also to the coefficient for the area variation (last term on the left hand side). The left hand side of the equation then consists of two remaining terms, each of which must now be linked to parameters upstream of the shock. For calculation purposes, the state "2" can be obtained by applying the Rankine Hugoniot relations (§I.9 on Page 222). The change in flow speed across the shock wave is given by (I.108), and the *signed* Mach number downstream of the shock is given by (I.115).

Returning to the main relation (5.2), by differentiating (I.108), the first term can be written using shock Mach number and changes in state "1" as follows:

$$\frac{1}{c_2}\frac{du_2}{dt} = \frac{1}{c_2}\frac{du_1}{dt} + \frac{(u_2 - u_1)}{c_2}\left[\frac{1}{c_1}\frac{dc_1}{dt} + \frac{M_s^2+1}{M_s^2-1}\frac{1}{M_s}\frac{dM_s}{dt}\right], \tag{5.3}$$

where,

$$\frac{1}{c_2}\frac{du_1}{dt} = m_1\frac{c_1}{c_2}\frac{1}{c_1}\frac{dc_1}{dt} + \frac{c_1}{c_2}\frac{dm_1}{dt}. \tag{5.4}$$

Note that once the approximations inherent in the characteristic rule are made (5.1), the above relations are exact. In the Han and Yin model (§4.6) the non-uniform flow upstream of the shock is *fully steady* and evaluation of the above terms in (5.4) does not pose any further challenge. In the present case, the flow upstream of the shock is both *non-uniform* and *unsteady*. This is the point of departure from the Han and Yin result (§4.6 on Page 79).

5.3.1 Lifting Isentrope

An exact closed form solution to this problem is not known. While it is possible to solve the entire flow computationally, doing so would be against the spirit of

the shock dynamics approach. Hence, an approximation must be made at this point to proceed further. As a first step, in the derivation below, we may attempt to use the steady-state relations (§I.6), but *with variable free stream stagnation properties*. Roughly speaking, the variation in time is approximated by splitting the temporal and spatial operators, such that the free stream velocity is *first* lifted in time, and *then* the quasi-steady spatial distribution is computed; hence, the label "lifting isentrope" seems appropriate for such a model. Strictly speaking the description is valid only in the quasi-steady situation when the temporal variation in m_∞ is small. Then, at first glance it may appear to be a poor approximation for application to impulsive flows where $f = c_\infty\, \partial_t(m_\infty)$ can be large $f/c_\infty >> 1$ (in terms of non-dimensional time). Fortunately, it turns out *not* to be the case; in fact the approach gives surprisingly accurate results (see Appendix G).

Consistent with the *lifting isentrope* model, we begin by differentiating (I.90) for non-constant p_1, and differentiating Eqs. (I.71), (I.72), and (I.75), for *non-constant stagnation state* (*i.e.*, variable total pressure and temperature evaluated using variable m_∞ and constant T_∞). Combining the differential expressions, the second term in (5.2) can be written as:

$$\frac{1}{\gamma p_2}\frac{dp_2}{dt} = \frac{2}{\gamma-1}\frac{1}{c_1}\frac{dc_1}{dt} + \frac{4M_s}{(\gamma+1)}\frac{p_1}{p_2}\frac{dM_s}{dt} \tag{5.5}$$

where,

$$\frac{2}{\gamma-1}\frac{1}{c_1}\frac{dc_1}{dt} = \frac{T_\infty}{T_t}m_\infty\frac{dm_\infty}{dt} - \frac{T_1}{T_t}m_1\frac{dm_1}{dt} \tag{5.6}$$

and,

$$\frac{dm_1}{dt} = \lim_{\epsilon\to 0}\frac{\dfrac{1}{A}\dfrac{dA}{dt} + \left(m_\infty - \dfrac{1}{m_\infty+\epsilon}\right)\dfrac{T_\infty}{T_t}\dfrac{dm_\infty}{dt}}{\left(m_1 - \dfrac{1}{m_1+\epsilon}\right)\dfrac{T_1}{T_t}} \tag{5.7}$$

Note that it is possible to rewrite the last expression without the ϵ terms, albeit with a caveat to use separate expressions for various physical scenarios to avoid trouble when $m_\infty = 0$ or $m_1 = 0$. Here, a more uniform approach is preferred so that in the numerical computations ϵ is simply treated as a small number (*e.g.*, 1×10^{-99}). It effectively enables computations of the classical test scenarios without any need for extra algorithmic logic. The *local* ratio of static to total temperature, T_i/T_t, is given by (I.70).

With the foregoing expressions, we can isolate for $d_t(M_s)$ as follows:

$$\frac{dM_s}{dt} = \frac{1}{G}\left(-\chi_1 \frac{dA}{dt} - \chi_3 \frac{dm_\infty}{dt} + \chi_4 \frac{dm_1}{dt} + \chi_5 f\right), \tag{5.8}$$

where, the G function is given by:

$$G = \frac{2}{\gamma+1}\left[\frac{c_1}{c_2}\left(1 + \frac{1}{M_s^2}\right) \pm 2\frac{p_1}{p_2} M_s\right]. \tag{5.9}$$

It is assuring to note that in the absence of the newer terms, namely the χ multiplicands for ($d_t\, m_\infty$, $d_t\, m_1$, and f), the g function by Whitham (4.2) on Page 72 is identical in value once (5.9) is multiplied by χ_1. Comparison with the result of Han and Yin also shows the equivalence of the two expressions (by setting $f = 0$, $d_t\, m_\infty = 0$ in (5.8).

The χ_i coefficients are given by:

$$\chi_1 = \pm \frac{m_2}{m_2 \pm 1}\frac{1}{A} \tag{5.10}$$

$$\chi_2 = \frac{\gamma - 1}{2} m_2 \pm 1 \tag{5.11}$$

$$\chi_3 = \chi_2 \frac{T_\infty m_\infty}{T_t} \tag{5.12}$$

$$\chi_4 = \chi_2 \frac{T_1 m_1}{T_t} - \frac{c_1}{c_2} \tag{5.13}$$

$$\chi_5 = \frac{1}{c_2} \tag{5.14}$$

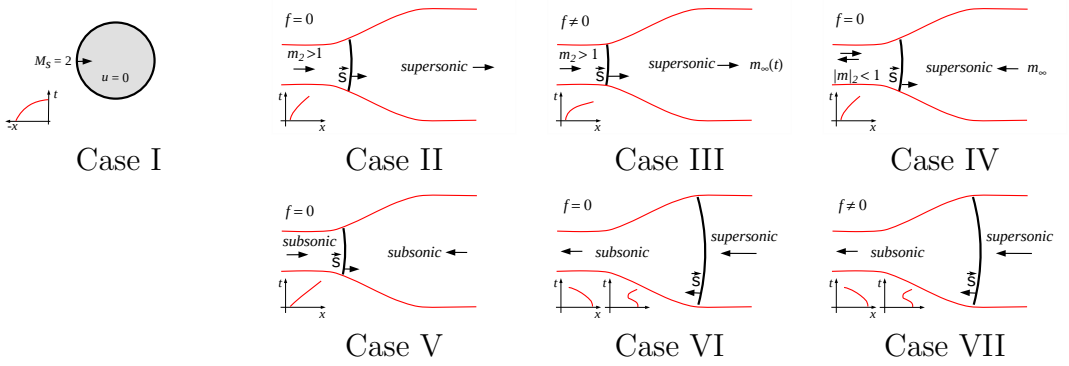

Figure 5.2: Various sample scenarios used below to illustrate application of the generalized shock dynamics theory.

The χ_i terms are reminiscent of Shapiro's elegant idea of separating the *influence coefficients*[68] associated with various physical effects present in compressible flow in a channel. *Of course, here one would make reference to the local shock Mach number instead of the local flow Mach number.* Some typical results obtained using (5.8) are illustrated next.

5.4 Example Scenarios

Favourable comparisons with accurate solution of the governing equations (CFD) can provide some confidence in the proper derivation of the above equations and in the validity of the assumptions used therein. To this extent, seven cases are illustrated in Figure 5.2; in what follows, these examples scenarios will be used to demonstrate general application of the theory.

In the various cases discussed below, the initial state is first established in a given geometry using Asterix[1] and the computation is saved once a steady state solution is obtained. In general, the non-trivial ($m_1 \neq 0$) saved state is then used as initial condition in the problem where a shock enters the channel either

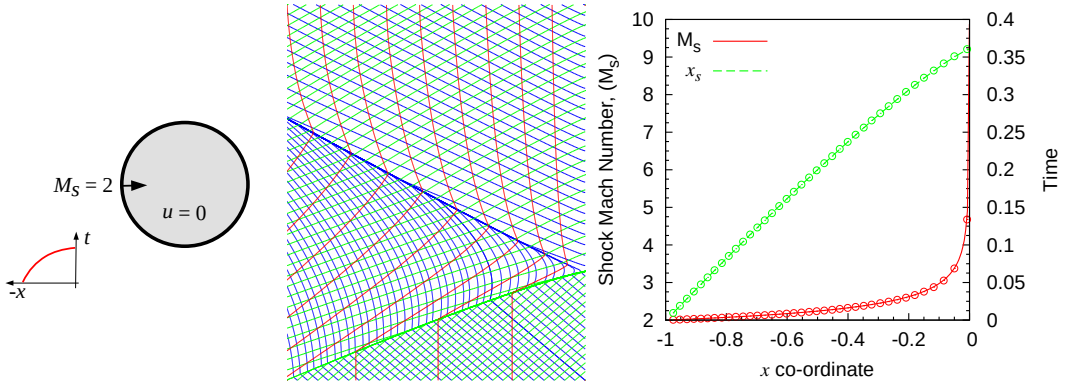

Figure 5.3: Case I: shock implosion problem (§3.2.4). (a) Schematic diagram shows cylindrical geometry, uniform, quiescent gas ahead of the shock wave, $\gamma = 1.4$. (b) Space-time diagram. (c) Comparison between CCW (5.8) (solid) and Asterix (circles). The agreement is considered excellent.

from the left or the right. Comparison is then made by integrating (5.8) for the IVP, starting with a common initial state which is specified as part of the problem statement. In what follows, "circles" denote CFD solution obtained using Asterix, and the solid lines describe the results of (5.8).

5.4.1 Case I

Figure 5.3 shows results for the implosion problem described in §3.2.4. Excellent agreement is evident between solutions from Asterix and CCW (5.8); and for this particular problem it is as expected. Recall, a similar comparison was already made between Asterix and the exact solution for the case of a strong shock wave (Figure 3.6a). As noted, the Guderley solution is not valid for the present case of an initially weak shock ($M_s = 2$). In contrast, the CCW approximation appears to be uniformly valid for this problem as shown in Figure 5.3.

Also, recall the earlier discussion surrounding the singularity for $m_2 = 1$, as addressed by Friedman. To illustrate that it poses no problems, the present

case is computed such that it precisely contains such a scenario (I.115); referring to Figure 3.6b, which corresponds to the above case, it is evident that the C_- characteristics are nearly vertical initially. However, for the right facing shock, the transonic flow ($m_2 \sim 1$) downstream of the wave does not pose any problems in the characteristic rule. In fact, it suffices to note that all such cases corresponds to the classical scenarios which were examined by Whitham. *These contain uniform, quiescent gas ahead of a shock wave with either subsonic, transonic, or supersonic flow behind the shock wave.* The CCW theory generally offers good approximation for such problems, with the noted exceptions as discussed in the preceding chapter. Hence, a more precise statement might read as follows: the CCW theory generally provides an accurate description of a "freely propagating" shock wave in a uniform, quiescent medium. *It is not clear from the existing literature to what extent the CCW approximation is valid for flows with non-quiescent gas ahead of the wave.*

5.4.2 Case II

Consider a steady, non-uniform, supersonic flow ($m_1 > 1$) ahead of the shock wave with supersonic flow ($m_2 > 1$) behind the shock wave. The shock wave enters the channel from the left. Figure 5.4 positively compares the CFD results with the extended CCW equation obtained above. Considering the simplifications made in deriving the relation (5.8), and considering the complex flow both upstream and downstream of the moving shock wave, it is truly surprising how much information may be gleamed from a single function.

This case confirms the correctness of the χ_4 term, as shown by $m_1(t)$ in the top-left subplot. With accurate prediction of $m_1(t)$, and with steady upstream flow (fixed $m_\infty = 3$), all of the upstream parameters must be correct; this is evident by the velocity and pressure plots. The downstream state is a function of shock

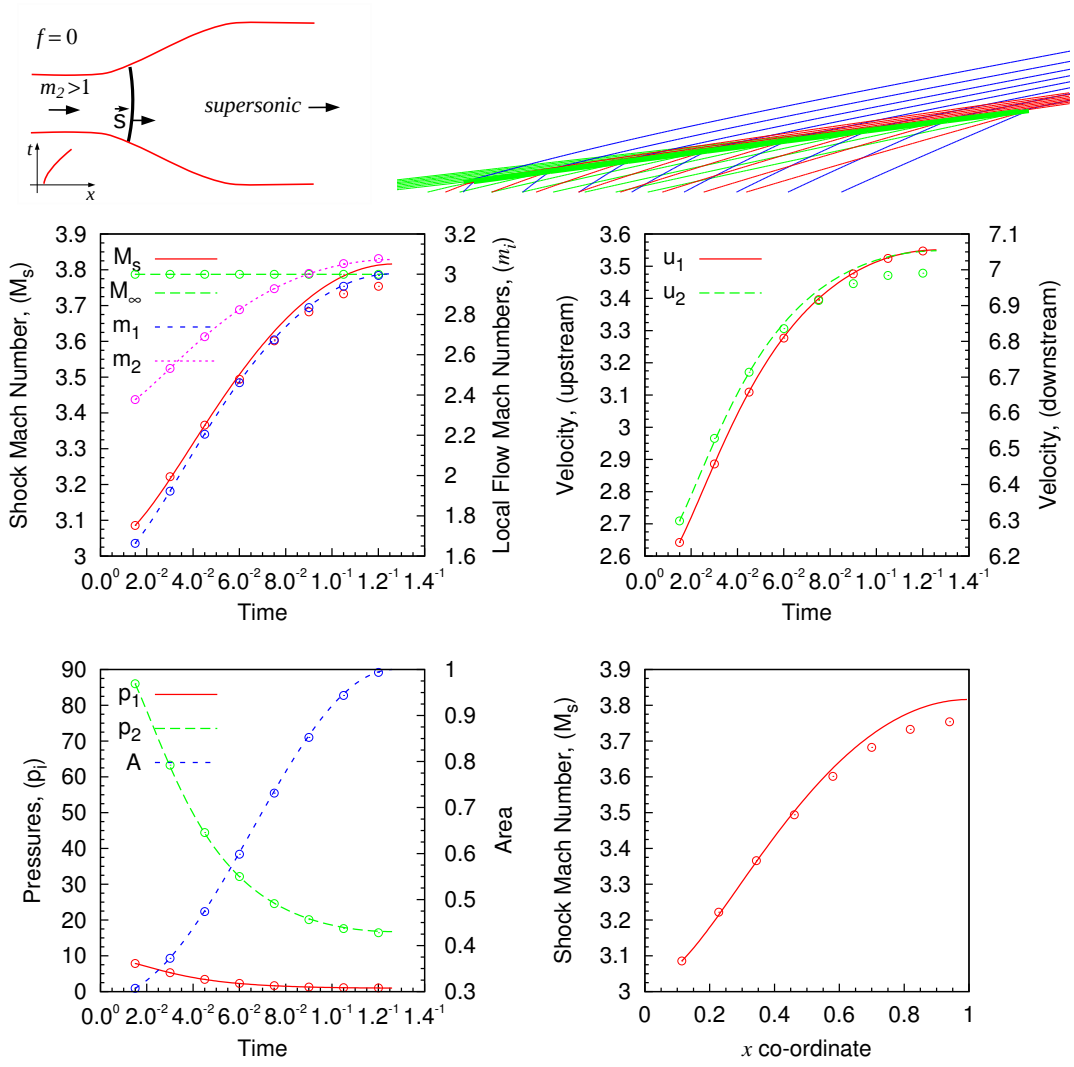

Figure 5.4: Case II: a left moving diverging channel encounters a right facing shock wave, $M_s \simeq 3$. Smooth geometry model, M_D3, IoS0.1. Non-uniform, non-quiescent gas ahead of shock, no body force present ($f = 0$). Comparison between CCW (solid) and CFD (circles). For simplest comparison see the lower right subplot first (M_s vs x_s); the remaining plots show various parameters as a function of time. Initial steady state values can be read at $t \simeq 1.5 \times 10^{-2}$ when the shock enters the channel; in this context, m_∞ refers to $m(x = L) = const$. The agreement is generally very good.

Mach number as well as the upstream state, and slight discrepancies are apparent where the shock Mach number is *not* predicted *nearly exactly*.

5.4.3 Case III

Consider an unsteady, non-uniform, supersonic flow ($m_1 > 1$) ahead of shock, with supersonic flow ($m_2 > 1$) behind the shock, and a nonzero body force term ($f > 0$). The main difference from the previous scenario is that a nonzero body force term is present. The problem is setup in such a way that a shock wave of specified strength enters the channel from the left at $t = 0$. Figure 5.5 positively compares the CFD results with CCW relation obtained above.

This case provides confidence in the validity of the χ_3, χ_4, *and* χ_5 *terms.* The $m_\infty(t)$ function is shown in the upper-left subplot and it is predicted accurately. The right velocity u_1 is shown in the upper right plot and it is also predicted accurately. Note, this case was also repeated for a much larger value of acceleration ($f = 10$) and the comparison was found to be equally accurate.

5.4.4 Case IV

Consider a steady, non-uniform, opposed supersonic flow ($m_1 < -1$) ahead of shock with unsteady subsonic flow ($-1 < m_2 < 0$) behind the shock wave. It is related to the unstarting scenario. An initially started steady supersonic stream ($m_\infty = -3$) originates from the right hand side. The problem is setup such that a relatively weak shock wave ($M_s \simeq 1.6$) enters the channel from the left and leaves an unstarted (subsonic) stream behind itself. Figure 5.6a shows a comparison of the unstarting process as obtained from Asterix and CCW (5.8).

The correspondence is surprising, considering the fact that the unstarting phe-

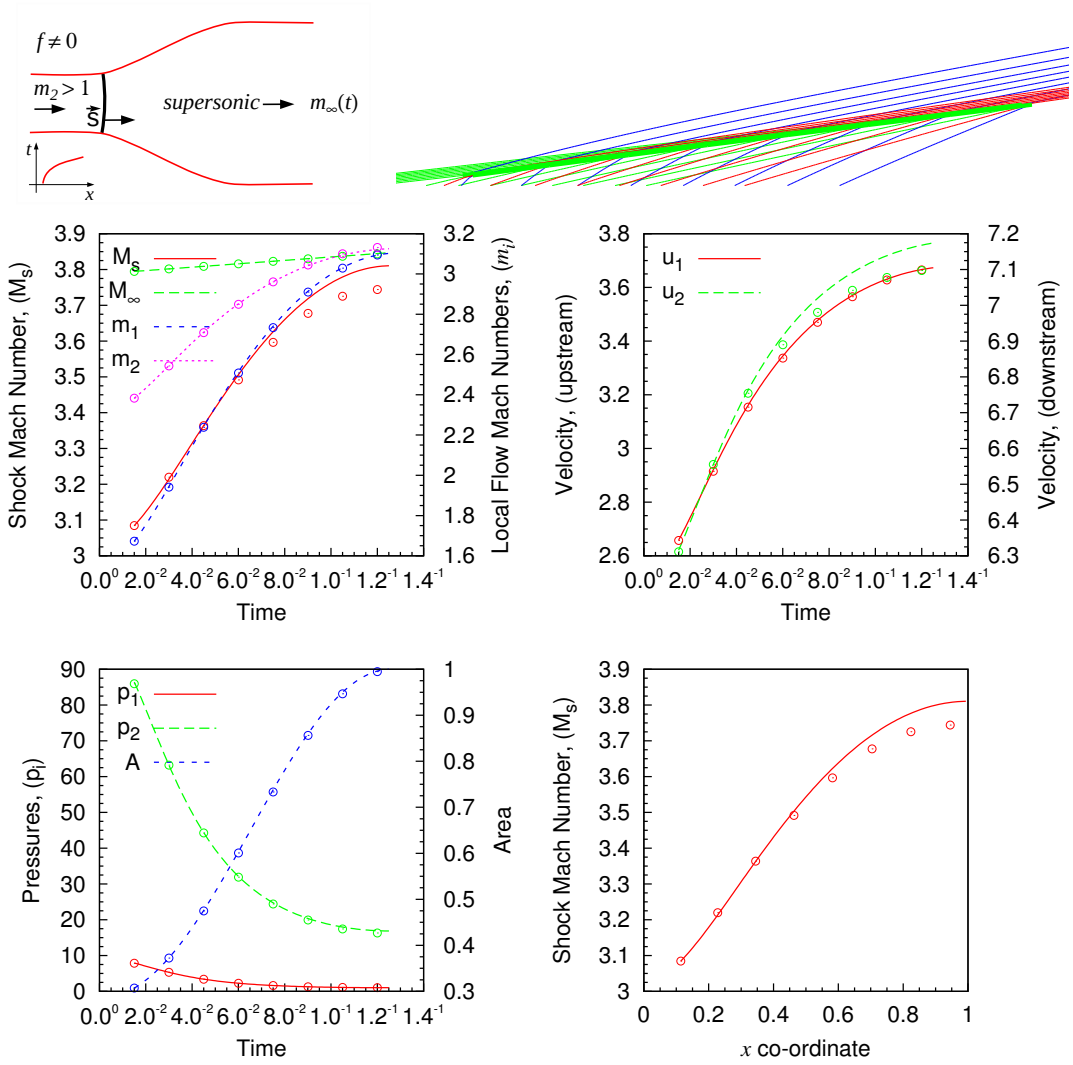

Figure 5.5: Case III: an accelerating, left moving channel encounters a right facing wave, $M_s \simeq 3$. Smooth geometry model, M_D3, IoS0.1 Non-uniform, non-quiescent gas ahead of shock, non-zero body force present ($f = 1$). Comparison between CCW (solid) and CFD (circles). For simplest comparison see the lower right subplot first (M_s vs x_s); the remaining plots show various parameters as a function of time. Initial steady state values can be read at $t \simeq 1.5 \times 10^{-2}$ when the shock enters the channel; in this context, the variation in m_∞ is due to $m|_{(x=L)}(t) \neq const$. The agreement is generally very good.

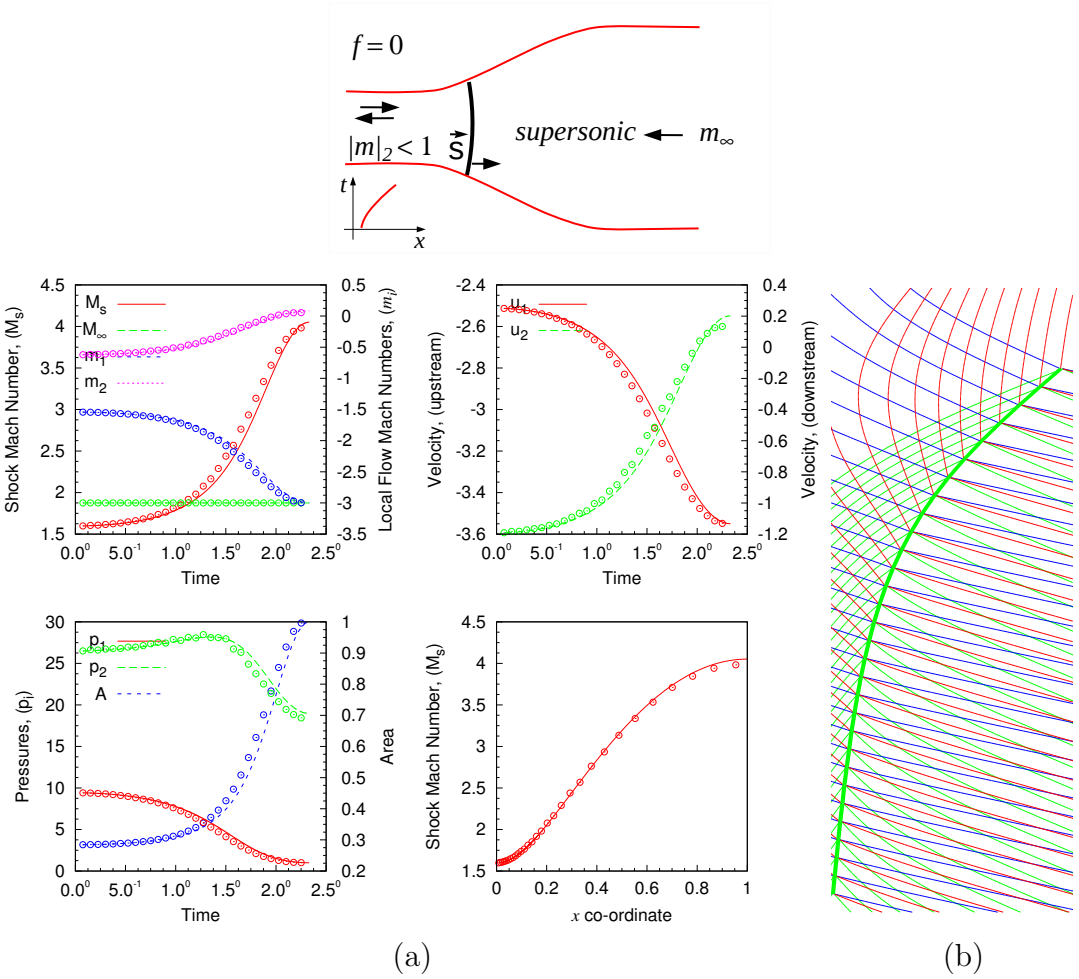

Figure 5.6: Case IV: Unstarting of an inlet; (a) comparison between CCW (solid) and CFD (circles). (b) Space-time diagram, Green–C_+; Blue–C_-; Red–C_0. Smooth geometry model: M_D3, IoS0.1. The agreement is generally very good.

nomenon is strongly coupled with disturbances generated downstream of the wave. However, this comparison shows that once a shock wave enters from the left, it can be self-supporting within the CCW framework and can continue to move rightward. Also, compared with earlier cases, the shock motion is 20 times slower (initially, the shock moves very slowly, which incidentally also explains the initial "bunching up" of the points in the $M_s(x_s)$ plot). Despite the large time interval, the local error does not appear to accumulate during the integration; hence, for such scenarios, the CCW approximation appears to be surprisingly accurate. Figure 5.6b shows the corresponding space-time diagram, illustrating the entire flow. Note that the unstarting process brings about violent changes in the flow structure (compare upstream wave configuration to the downstream one). Some of the features may be deduced more precisely from Figure 5.6a, but the overall process is much less apparent. For instance, at $x = 0$, the shock wave is relatively weak and causes the flow to slow down from $-m_1 \simeq 1.5$ to $-m_2 \simeq 0.6$; similarly at $x = L$, the abrupt changes across the shock wave cause the flow to go from $-m_1 \simeq 3$ to $-m_2 \simeq 0$. Also, the C_+ and the C_- waves directly behind the shock wave appear to be nearly straight segments; this is particularly true for the C_- waves. The situation is reminiscent of the simple wave solution from §3.2.2; more on this observation will follow in Chapter 7.

5.4.5 Case V

Consider a steady, non-uniform, subsonic stream originating on the right ($-1 < m_1 < 0$). A moderate strength shock ($M_s \simeq 3$) enters the channel from the left leaving behind a rightward subsonic stream in the channel ($0 < m_2 < 1$). Figure 5.7a shows a favourable comparison between Asterix and CCW (5.8).

The corresponding space-time diagram (Figure 5.7b) shows the formation of

(a)

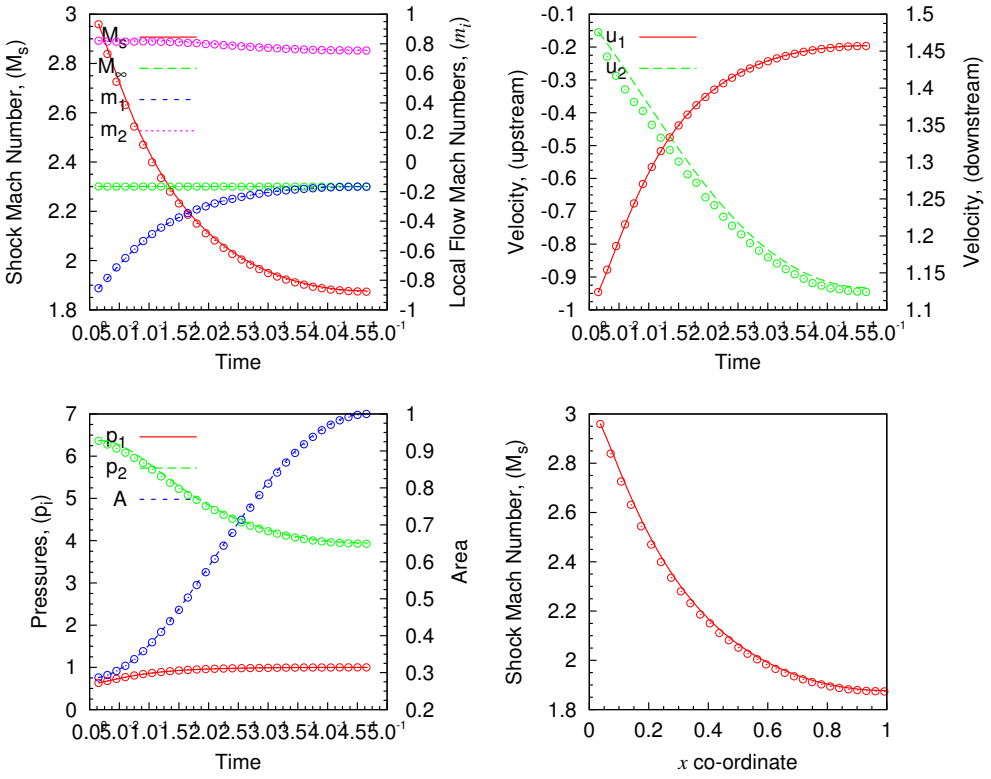

(b)

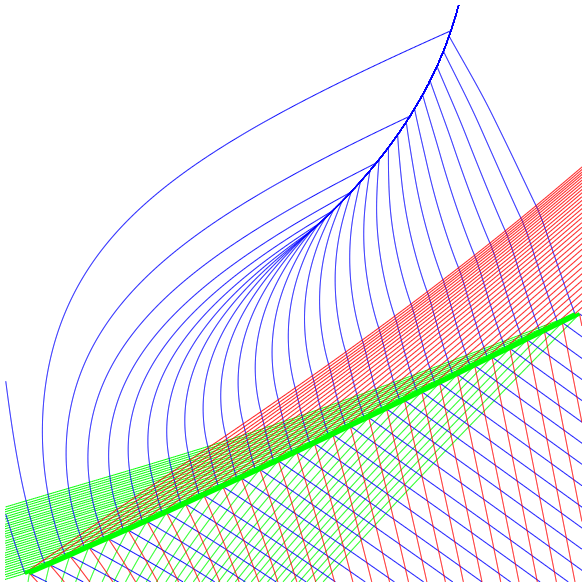

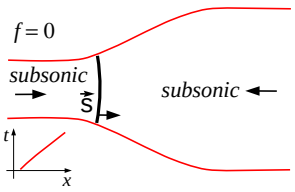

(c)

Figure 5.7: Case V: Leftward upstream subsonic flow, rightward downstream subsonic flow. (a) Comparison between CCW (solid) and CFD (circles). (b) Space-time diagram, Green–C_+; Blue–C_-; Red–C_0; (c) Schematic diagram.

a left-facing* compression wave leading to a secondary shock wave. Within the time interval considered, the left facing shock also moves rightward; the situation corresponds to collision of two opposed flows (rightward flow overcomes the leftward flow) in a diverging section. Subsequent formation of the secondary shock in the diverging section is analogous to nozzle starting process; and, the possible or eventual stabilization of this shock is analogous to the case of a stationary shock wave occurring in a nozzle.

5.4.6 Case VI

Consider a steady, non-uniform, supersonic flow ($m_1 < -1$) ahead of shock with unsteady transonic flow ($m_2 < 0$) behind the shock. It is related to the impulsive flow starting scenario (§1.3.2.2). Figure 5.8 shows the wave diagram.

A right facing wave enters the channel following sudden removal of a membrane; prior to its rupture, the membrane initially supports the high pressure behind the right facing shock wave situated slightly upstream of the channel (hence it is usually called the bow wave). In the present context, we only consider shock dynamics inside the duct, and for the purposes of CCW, *i.e.*, integration of (5.8), the initial condition are considered known.

For this case, Figure 5.9 shows singular behaviour of the CCW relation, and (5.8) can not be used to integrate the shock motion. This singular behaviour will be discussed in the following chapter.

*Recall colour designations from Page 63

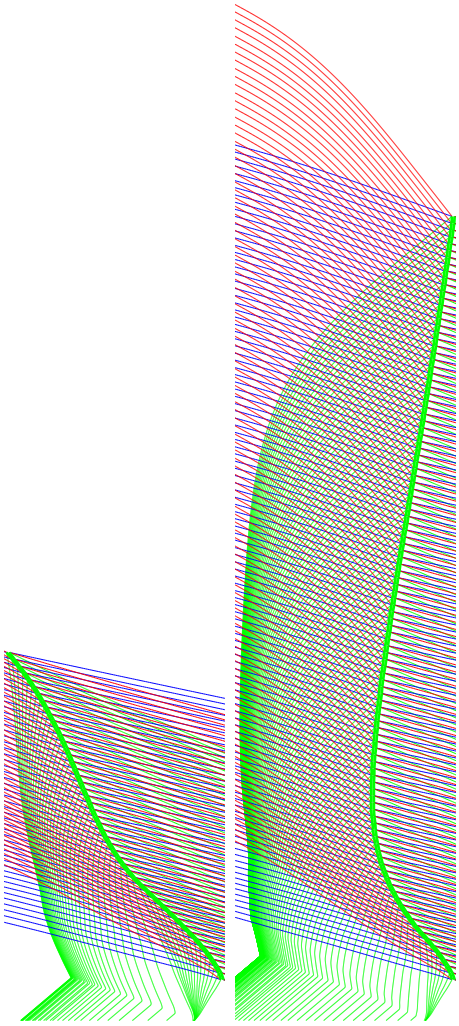

Figure 5.8: Case VI: Asterix model for the membrane rupture scenario; smooth geometry, $M_D 3$, $m_\infty = -3$, IoS0.9, $p(x < L, t = 0)/p_\infty = 0.5$ (left) and IoS0.8, $p(x < L, t = 0)/p_\infty = 1$ (right). Initial shock standoff distance is based on data from Liepmann and Roshko[134] Fig. 4.15. The density and pressure behind the bow wave are assumed instead of the parameters on the stagnation streamline, and the velocity is linearly distributed such that it attains the correct value directly behind the "stationary" shock and is zero at the "membrane" at $x = L$. Note that a more sophisticated simulation of this flow is possible[77], however for the purpose of present discussions, the simpler model may be considered sufficiently representative; both starting and unstarting scenarios may be generated, as test cases for shock dynamics, while using reasonable values of the parameters.

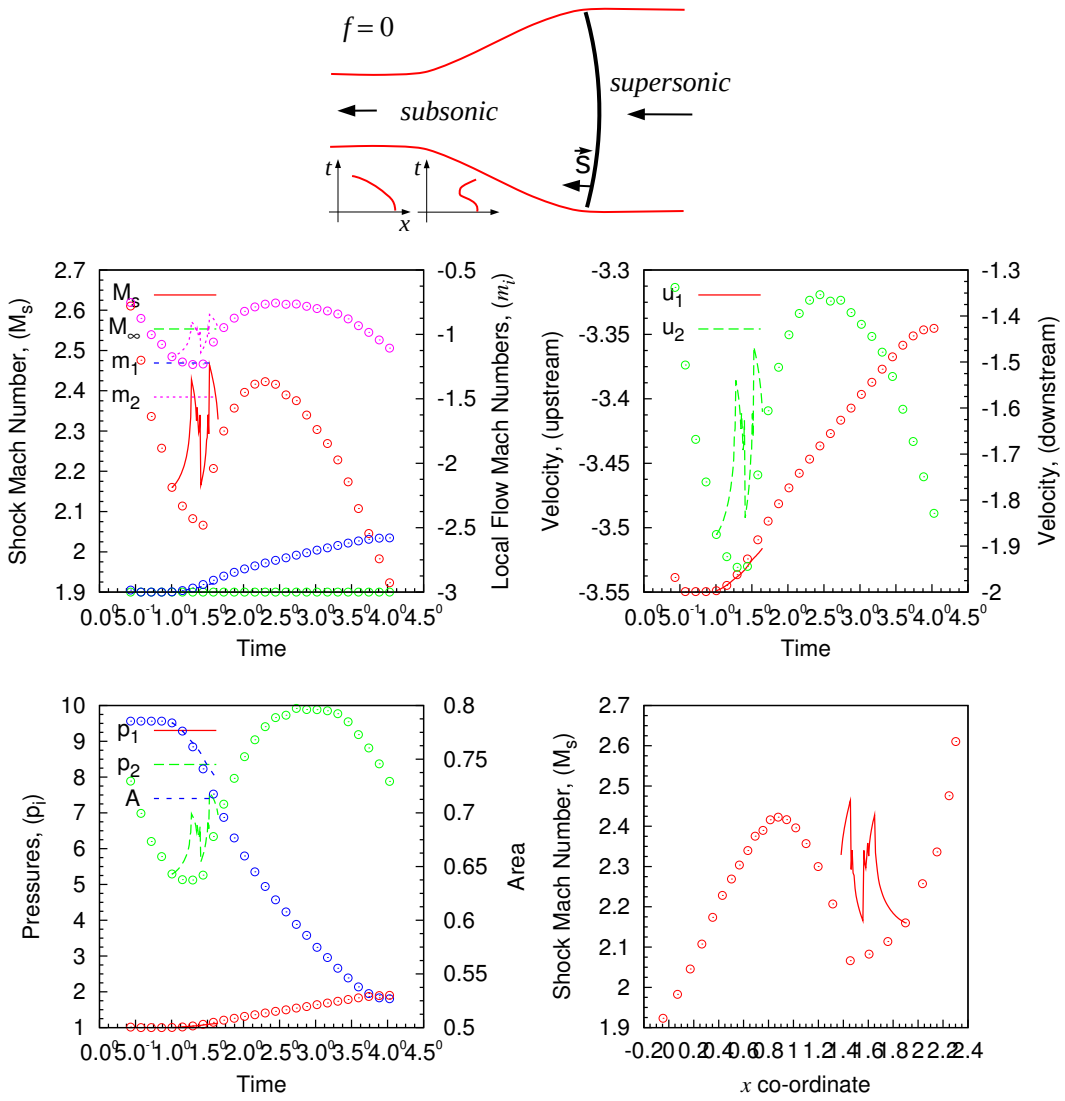

Figure 5.9: Case VI: Impulsive flow starting scenario. This result shows remarkable failure of the approximate model, as (5.8) exhibits singular behaviour for $u_2 + c_2 = 0$. Compare the $m_2 = -1$ points (three distinct ones) in the top-left subplot, with the corresponding space-time diagram (Figure 5.8) where the C_+ waves are stationary (vertical), and note that the concept of flow choking is not applicable to unsteady flows.

5.4.7 Case VII

The second scenario related to impulsive intake flow (§1.3.2.1) occurs following accelerative motion of the channel. Figure 5.10a shows comparison with Asterix. Comparing with Figure 5.10b, the comments made regarding the singularity occurring during typical shock passage are equally applicable here as well. *The singular behaviour occurs in smooth flow region.*

5.4.8 Some Observations

Inspection of the foregoing expression (5.8) with the χ terms, shows smooth behaviour in all terms, except the coefficient for area term, χ_1, which has a singularity at $m_2 = -1$ (and similarly, at $m_2 = 1$ in the case of a left-facing shock). Note that there is no singularity in this result when $m_2 = 1$ for a right facing shock wave. This point was discussed in the preceding chapter in connection to Friedman's work. It was also illustrated by the example in §5.4.5.

The physical significance of the other singularity ($m_2 + 1 = 0$) does not appear to be well understood as hinted previously (§4.3.1). It is likely that both Chester and Friedman dismissed this as a pathological case, *based on physical grounds*, because in the respective analyses such situations are impossible; in the general case however, it can not be dismissed.

To the author's knowledge, the singularity has been only discussed in an appendix to Ref.[135]; referring to the G_1 function* from Han and Yin's text, the authors analyze various scenarios based on the sign of dA, dm_1, and m_1 in connection to their work. The article also shows the behaviour of (4.7) for $m_1 < 0$ for various values of shock Mach number. In interpreting the presence of verti-

*Recall that it is reproduced for easy reference, as (4.7) on Page 79 in the present work.

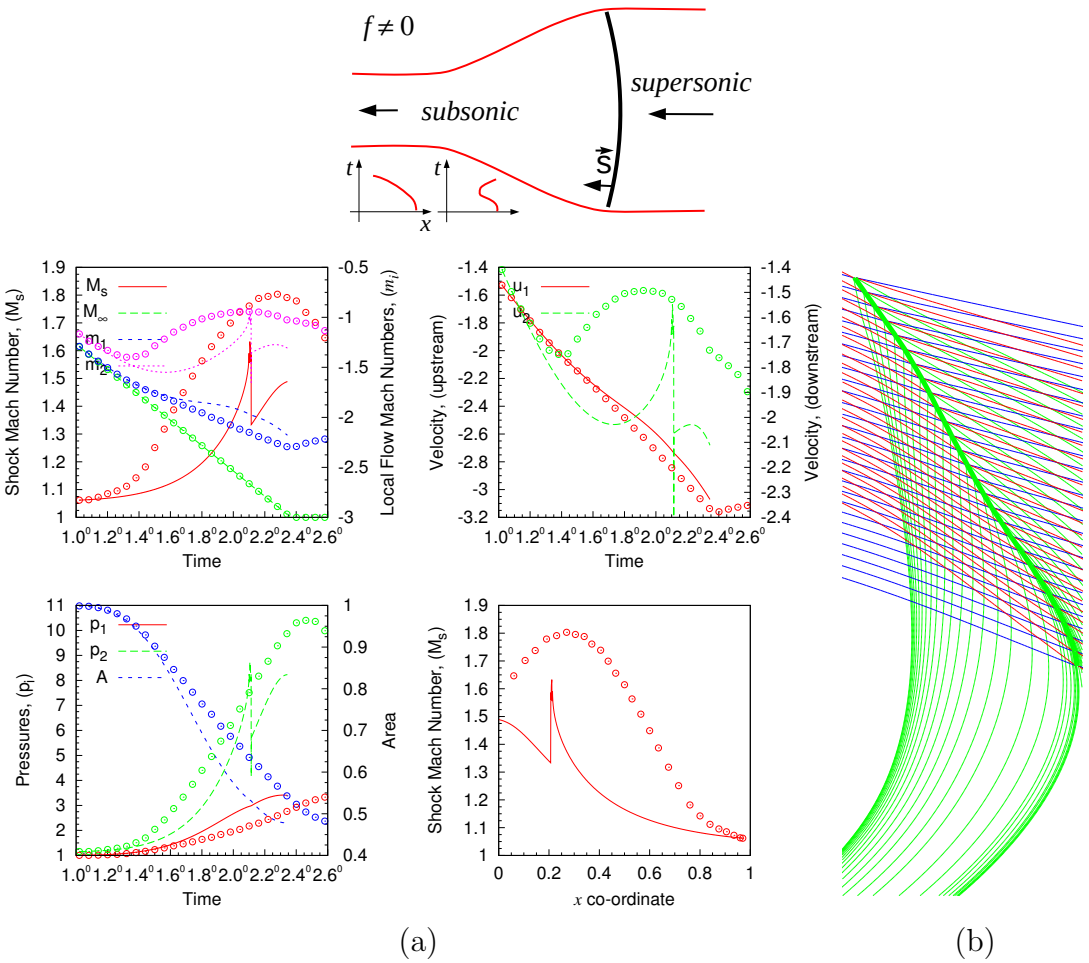

Figure 5.10: Case VII: Accelerative starting scenario. (a) Shows remarkable failure of the approximate model, as (5.8) exhibits singular behaviour for $u_2 + c_2 = 0$. (b) Space-time diagram, Green–C_+; Blue–C_-; Red–C_0; note the presence of singularity causing C_+ waves arriving at the shock. The agreement is generally not very good.

cal asymptotes[135] Fig. 13, pp. 46 of the cited article, which are caused by the singularities in (4.7), it states*:

> As seen in figure 13, $G_1 < 0$ up to the point where $m_2 \to -1$, at which the *flow chokes* immediately behind the shock front *owing to the influence of the area change*, which stands on the term in the numerator of the function G_1. After the discontinuity in G_1 at $m_2 = -1$, G_1 becomes positive.
>
> Once the behaviour of the function G_1 is known, the rules for the interaction of the area change with the shock front can be obtained from (A 1) [*i.e.*, (4.6)].

The cited interpretation of flow choking owing to the influence of area change would require that for a *regular* solution to exist, dA must be zero when G_1 is singular. Hence, the presence of the singularity is likened to that of sonic flow condition at the throat area in a steady stream. The process of flow choking describes a *limiting* condition for *maximum mass flux*; whereas the concept of a limit on the mass flow under steady choked conditions does not extend to unsteady flows, there exists some confusion in the literature about the physical significance of this singularity.

5.5 Summary

The basic CCW formulation has been extended to include non-uniform, non-steady upstream flows. The approach results in a differential relation of the general form $d_{\sigma(t)}\, F(\gamma, M_s(t), \ln A(x_s), m_1(t), m_\infty(t), f(t))$ which is to be integrated along

*The *emphasis* is added by the present author.

the shock trajectory. The lifting isentrope model, furnishes another differential relation for non-uniform unsteady upstream flow $F(f/c_\infty, m_\infty, m_1, A(x_s)/A_\infty)$. In this way, the system is mathematically closed, and comparison of the solution with Asterix, for a broad set of problems, shows remarkably good agreement.

For the case of impulsive flows leading to intake starting, accurate solution of the problem may be obtained using Asterix. However, for these cases, a non-singular CCW solution does not exist in general. *That is to say, the above singularity causing scenario should not be regarded as a pathological case. It is a typical scenario, one among infinitely many others, where a non-singular solution to* (5.8) *does not exist because* $(u_2 + c_2 = 0)$ *is encountered at some point in the shock trajectory. Because the* C_+ *wave is central to the characteristic rule, the precise conditions causing the singularity must be examined first. This is done in a brief chapter which follows next.*

Chapter 6

Singularity in CCW

God does not care about our mathematical difficulties. He integrates empirically.

Albert Einstein

6.1 Introduction

The present chapter builds on §5.4.8 and §5.4.1, and it establishes the precise conditions leading to the singularity in CCW. The analysis concerns the variation of downstream states in the near vicinity of the shock wave, as a function of the state immediately upstream, and of the strength, of the shock wave. It is independent of any discussion on *if and when* such singular conditions arise; *i.e.*, it is not the aim of this chapter to show *how* the shock strength and the upstream state will be perturbed with area variation and by the changes taking place in the free stream state. As indicated in the preceding chapters, the sonic flow condition downstream of the moving shock wave occurs in two different ways; these are discussed next.

6.2 Singular Condition, Type I

The first scenario is that $(u_2 - c_2)$ vanishes at the shock. This issue was known to Chester[89] and he provides a detailed account of the physical scenarios which would follow this condition. Namely, he suggests that the C_- disturbances would tend to coalesce, leading to non-linear behaviour including flow choking. It is safe to say that such non-linear behaviour may occur even if the $(u_2 - c_2) \neq 0$ (*e.g.*, Figure 5.7b). On Whitham's suggestion Friedman[125] addressed this issue by retaining appropriate non-linear terms in Chester's analysis. Incidentally, the correction which he obtained leaves the Whitham's characteristic rule unaltered. *It is moot to deal with this case further (Figure 5.3), and in the present context the other singularity is the relevant one. For shock dynamics performed on a left facing wave, the situation would be reversed.*

6.3 Singular Condition, Type II

The second scenario is that $(u_2 + c_2)$ vanishes at the shock. This condition is mentioned in[89], but then ruled out as a physically relevant possibility (which is the correct assessment for the flows discussed in the cited works), as already discussed in §4.3.1 on Page 76.

Consider the geometry inset in Figure 6.1 which describes a moving right facing shock wave in an arbitrary upstream state. The shock wave connects the upstream state to the downstream state through the Rankine-Hugoniot relations (§I.9.1). These can be easily combined to give a functional relation of the form $f(\gamma, u_1, c_1, M_s, u_2, c_2) = 0$. Substituting the condition $(u_2 + c_2 = 0)$ and the definition $(m_1 = u_1/c_1)$ into this function, one obtains a relation of the form $m_1 = f(\gamma, M_s)$. Hence, the expression so obtained, shows the locus of all singular

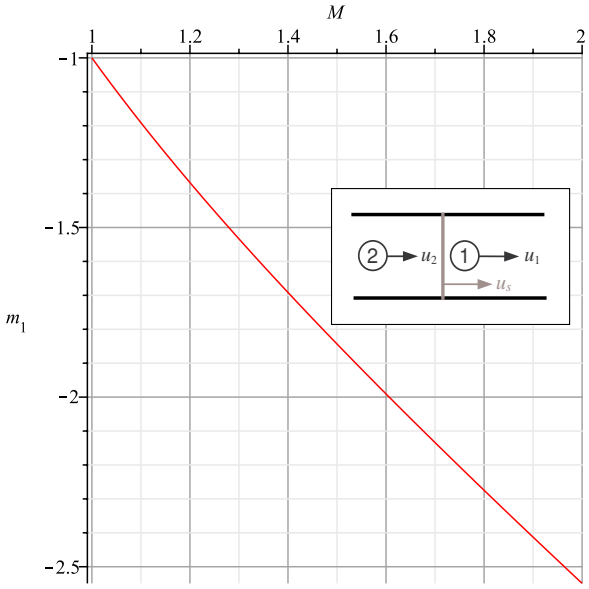

Figure 6.1: Locus of "singular" states relating upstream state and the strength of the shock wave. Plot is valid for $\gamma = 1.4$.

states as a function of upstream state and the strength of the wave. A plot of this expression (Figure 6.1) shows almost linear behaviour between singular m_1 and M_s.

$$m_1 = -\frac{2\,{M_s}^2 - 2 + \sqrt{\left({M_s}^2\gamma - {M_s}^2 + 2\right)\left(-\gamma + 1 + 2\,{M_s}^2\gamma\right)}}{(\gamma + 1)\,M_s} \tag{6.1}$$

It is evident from the plot that solution to (6.1) only exists for opposed supersonic flow ($m_1 < -1$). Note that the above relation is for a right facing shock wave, and that the same situation would exist whenever ($m_1 > 1$) for a left facing shock wave. In the general case where the upstream flow is either quiescent or it flows to the right ($m_1 \geq 0$), or it is leftward subsonic ($-1 < m_1 < 0$), then no singular solution exists.

6.4 Summary

The locus of states leading to singular behaviour in CCW can be obtained simply by analyzing the Rankine-Hugoniot relations. This analysis shows which scenarios might avoid singular behaviour in the case of ($m_1 < -1$). With an initially specified shock wave entering and travelling in a specified area distribution ($A(x)$), to avoid singular behaviour in CCW, the state path must either remain "parallel" to the curve of singular states, or always move "away" from it. In general, for flows containing $m_1 < -1$, it is possible and perhaps likely (though not guaranteed, *e.g.*, Figure 5.6) that the singularity will be encountered. *These statements explain the dramatic failure of* (5.8) *demonstrated in Figure 5.10, in an otherwise "well behaved" and "smooth" downstream flow. That is to say, the "singularity" is not a singularity in the governing equations, rather it is an artifact of one or more assumptions made in deriving the CCW relation.* The issues are resolved in the following chapter.

Chapter 7

Shock Dynamics—Revisited

Theories of the known, which are described by different physical ideas, may be equivalent in all their predictions and hence scientifically indistinguishable. However, they are not psychologically identical when trying to move from that base into the unknown. For different views suggest different kinds of modifications which might be made and hence are not equivalent in the hypotheses one generates from them in one's attempt to understand what is not yet understood.

Richard P. Feynman

7.1 Quick Review

In the preceding chapters it was established that there exists a singularity in the CCW theory which prevents its application to certain flows. The precise condition at which the singularity exists was determined as a function of wave strength and the upstream state. It was also established that there is *no physical significance* to this singularity, and hence, it must be an artifact of one or more assumptions made in deriving CCW.

In contrast to Whitham's characteristic rule,* the original works of Chester and Chisnell, were based on more rigorous analyses, with precise statements on the assumptions made; whereas Chester began with the three-dimensional equations of motion and performed an averaging process (in the hydraulic sense), Chisnell showed that it is sufficient to use the quasi-one-dimensional form at the outset, *before* any further assumptions and simplification lead to the shock-Mach number area $M_s(A)$ relation.

Ignoring for a moment the minor differences†, the three CCW relations are considered equivalent. Hence it is instructive to examine these together. A cursory inspection of Chester's article reveals an important clue; use of steady-state relations is *assumed* to connect the states on either side of the area variation. Indeed, for the problem considered by Chester this assumption was well justified, as reviewed on Page 72. Chisnell's treatment‡ is based on Chester's description, except that he started from the one-dimensional equations, and also provided a closed form relation (he was able to integrate the final differential expression). While this sufficiently explains the presence of the singularity§ in the final expressions from Chester and Chisnell, this does not explain the appropriate steps needed to remove its presence in Whitham's characteristic rule. To examine the situation further, and keeping in mind the remarks by Whitham, as quoted on Page 75, it seems necessary to take a somewhat different approach; after some pondering, one discovers that a simple analogy, made between the wave like disturbances and an *imaginary smooth fabric* floating above the space-time plane, helps to visualize

*Recall the manner in which it is obtained, as quoted on Page 74.

†Recall the discussions surrounding Type-I singularity, as reviewed on Page 110.

‡Effect of reflected disturbances generated by the shock is neglected. Steady state solution of Chester's problem, valid only for large time, is used[90] pp. 287.

§The term $(m^2-1)^{-1}$ appears in the steady-flow relations for du, dp, and $d\rho$ in Eqs. (F.5), (F.9), and (F.8), respectively.

and also to resolve some of the mathematical difficulties. *It leads to a derivation where the physical arguments naturally suggest Whitham's beautiful characteristic rule, but more importantly, it enables removal of the singularity from the CCW.*

7.2 Fault Causing Threads

In the foregoing analysis, it was sufficiently demonstrated that the quasi-one-dimensional framework admits a rich description of the shock motion, and that it is relatively easy to trace all waves within a two-dimensional $(x,\, t)$ space, starting from their respective origins $x_i(t_0)$ at the initial time moment. This is not a novel idea—the wave trajectories and the particle paths were well explored in various settings by Courant and Friedrichs[2]. It is the well regarded method of lines which was known to Riemann and Earnshaw and possibly to Stokes even before. The space time plots shown earlier in Figures 5.6, 5.7, 5.8, and 5.10, are but a few examples of the wide ranging phenomena which may be determined in this manner.

In the present work, however, the above idea has been used in a slightly different manner; here, the waves have often been traced *backwards* in time.* The space-time plots obtained in this way suggest that the differential equations of motion may be considered as sufficiently well behaved on either side of the shock wave. That is to say, it appears adequate to treat the three dimensional surfaces (smooth fabric) formed above the (x, t)-plane by the Riemann variables† as

*Strictly speaking this is not physically possible; but, it was possible to do so in this work because the full solution from Asterix on either side of the shock wave and the wave trajectory itself was known for all time.

†The two variables $J_{\pm} \equiv u \pm 2/(\gamma - 1)c$ which tend to maintain their values along the respective $C_{\pm}$ curves, and the entropy s which tends to maintain its value along C_0; recall from Page 68, the $J_{\pm}$ are *non-invariants* in this work because of non-homogeneities $(A_x, s_x, f) \neq 0$ present in the governing equations. The third Riemann variable is the entropy which is preserved

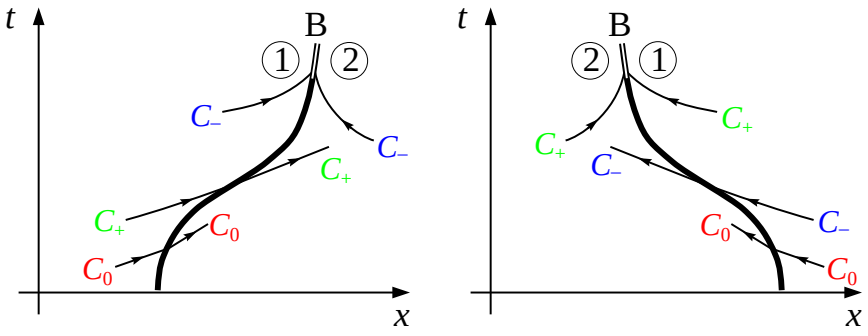

Figure 7.1: A fault forming in a fabric being weaved in space-time from three differently coloured threads. If the C_+ curves were thought of as green coloured threads, then upon merging they would weave together a *green coloured fault*. If the C_- were imagined as blue coloured threads, upon their merging a *blue coloured fault* would appear. In the left picture, C_+ and C_0 are the cross-threads, and C_- are the fault causing threads. In the right picture, C_- and C_0 are the cross-threads, and the C_+ are the fault-causing threads. The two situations are symmetric; the scenario on the right is the one which is discussed throughout this work.

smooth, differentiable two-manifolds.*

Conceptually, then, in shock dynamics one seeks the trajectory of an internal boundary-like curve, $\mathcal{B}(x_s, t_s) = 0$, appearing as a fault in an otherwise smooth fabric (see Figure 7.1). It may be imagined that the fabric is actually being weaved in time, on either side, using three differently coloured cross-threads. The fault may itself be imagined as two strands of an infinitesimally thin zipper forcing together threads of a particular colour (say green). After the green threads merge, they "pile up" inside the fault, but *before* that can happen, kinks must locally

along C_0 curves. The Rankine-Hugoniot jump relations relate these quantities across a shock wave.

*The strict definition would require the characteristics as being one-manifolds across which the derivatives may be discontinuous. Here, the term one-manifold indicates a connected set of points, with every point having a neighbourhood that looks like a segment of a line [136]; Smooth differentiable nature indicates the existence of derivatives along the line. Two-manifold indicates one higher dimension, *i.e.*, a surface that is locally "disk" like; smoothness implies existence of derivatives.

appear in the green threads which approach the fault in an oblique manner.* The variable density of the threads modifies the local strength of the fabric continuously, as, at each identifiable moment a new one arrives from either side of the fault.

For a right facing shock, in the above analogy, the C_+ waves are the fault causing threads. The C_- and the C_0 waves on the other hand tend not to pile up†, as these are the cross-threads which go across the fault, continuing from one particular side of the shock; *i.e.*, in the fabric being weaved together in space-time plane, their trajectories indicate the direction of the cross threads. They appear to refract right at the fault indicating that the properties of the fabric or medium locally undergo discontinuous change. Of course, with sufficient time, away from the shock the C_- *may also tend to coalesce* and then a left-facing shock *would* form. If the cross-threads originate on the right side of the fault, it is a right-facing shock, if they originate on the left, it is a left-facing shock.‡

Concluding the analogy, the Rankine-Hugoniot relations provide the rules and conditions relating the properties on either side of the fault in the fabric being weaved and zipped together in space-time. Intuitively then, for the two strands of the zipper, which are themselves one-manifolds, one may seek a differential relation; once this is done, the shock dynamics approach is akin to zipping up pieces of fabric that have undergone drastically different (anisotropic) shrinking on either side. Mathematically, it amounts to integrating the differential relation for an IVP. The above considerations suggest the existence of differentiable strands on either side of the shock wave.

*It is not necessary, on approach, for them to be running in the same direction as the fault.

†Recall, this description is for right facing waves. Reverse would be true for left facing waves.

‡Recall, by definition, the origin of the particle paths determines the facedness. If the fluid enters the wave from right, it is defined as a right facing wave.

7.3 Differentiable Faults

At first it seems unusual to associate a shock wave with anything smoothly differentiable. However, in shock dynamics, this is precisely the description; a differential relation is obtained which is supposed to hold *along* the shock wave . In the fault analogy, there is a differential relation which holds along the strands of the zipper; *if it is the green waves which form the strands, then it is only natural to apply the C_+ differential relation to the shock.*

However, as already established, the above approach does not provide a sufficiently stable description for all conditions; under certain circumstances, the differential relation obtained in this manner does not contain non-singular solutions. Because of the non-linearities associated with the shock wave, the physical situation has most likely been misinterpreted in the literature—at least in some cases, as mentioned in the preceding chapter. In all such cases encountered here by the author, it appears that the governing equations do admit a locally smooth solution. There are many physical scenarios in reality, as was concluded in the preceding chapter, where it appears possible to obtain non-singular solution to the fault manifold even though the C_+ locally approach it vertically. Indeed, it seems more natural to think that non-smooth behaviour would occur when a *finite* strength wave would approach the shock; if a bundle of threads would simultaneously appear, then it is difficult to imagine that their approach would necessarily be vertical (the contrary seems more likely).

Based on the above considerations, it seems reasonable to think that the desired *non-singular* differential relation holding along the shock (fault manifold) must be obtained directly from the governing equations *rotated along the local fault trajectory.* If possible, that would give an *exact* relation; however, it also

seems unnatural to expect that one would be able to solve the problem locally along the fault in an exact manner, without regard or dependence on the global solution. Thus, it is likely that any useful differentiable manifold would only be solved approximately, unless all pieces of information arriving at the fault were integrated precisely (*i.e.*, unless individual threads approaching the fault were traced backward in time precisely).

7.4 Derivation of CCW$^+$

Following the above ideas, the governing equations must first be rotated to apply along the characteristic directions.* The resulting equations (§I.8.3 on Page 220) describe the variation of Riemann variables in the three characteristic directions (*i.e.*, along the green†, blue‡, and red§ threads):

$$C_\pm: \quad \mathbf{D}_\pm\left(J_\pm\right) = -\left(\pm\frac{\gamma-1}{8}\left[J^2\right]_-^+\frac{A_x}{A}\right)+\left(\frac{\gamma-1}{4}\left[J\right]_-^+\right)^2\frac{1}{\gamma R}s_x+f \tag{7.1}$$

$$C_0: \quad \mathbf{D}\left(s\right)=0 \tag{7.2}$$

As noted in Chapter 3, where A_x, s_x, and f are zero, the homogeneous form of the equations reduces to the familiar form which lead Riemann to discover the invariants named after him, *i.e.*, $\mathbf{D}_\pm\left(J_\pm\right)=0$ gives $J_\pm = const_\pm$ along the respective characteristics¶. Strictly speaking, another scenario may be possible

*It is a standard procedure, *e.g.*, it appears as an assigned problem in Hirsch[137] pp. 217. The necessary steps effectively lead from the equations in §I.3 which are written in terms of conserved quantities and their fluxes, respectively differentiated along the principal directions ∂_t and ∂_x, to those written in terms of Riemann variables $J_\pm \equiv u \pm 2/(\gamma-1)c$, and s, and the differentials of these variables along the respective characteristic directions.

†$\mathbf{D}_+\left(\right) \equiv \partial_t\left(\right)+\left(u+c\right)\partial_x\left(\right)$

‡$\mathbf{D}_-\left(\right) \equiv \partial_t\left(\right)+\left(u-c\right)\partial_x\left(\right)$

§$\mathbf{D}\left(\right) \equiv \partial_t\left(\right)+u\,\partial_x\left(\right)$

¶Except where they cross the shock; there, the Rankine-Hugoniot relations may be used to

where the Riemann invariants exist while $A_x \neq 0$: it seems possible that the combinations could be arranged such that the right hand side vanishes altogether or becomes negligible, but in general it is not the case, for not all of A_x, f, and s_x are arbitrarily specified.

Referring back to Figure 7.1b, note that there are a total of six variables which define the states of the zipper strands: J_{1^+}, J_{1^-}, J_{2^+}, J_{2^-}, s_1, and s_2. Changes in these variables determine the evolution of the shock wave—its dynamic behaviour is determined by the rate at which these quantities change for a given geometry $A(x)$ and other specified conditions $f(t)$, $m_\infty(t)$, *etc.*

In the upstream (1) state, all three waves approach the shock wave, whereas in the downstream (2) state two leave and one arrives, *i.e.*, no threads originating on the (2) side ever make it across the fault; that is the defining characteristic of such a faulty fabric. Given the states at some initial time $t_s = t_0$, if the *proper directional* rate of change of the Riemann variables can be determined, then a well-defined IVP may be solved.

For a well-posed IVP, the physical situation with regard to information propagation demands that rate of change of all three quantities J_{1^+}, J_{1^-}, and s_1 be *specified* on the upstream side, while the rate of change of J_{2^-}, and s_2 be *determined* according to the Rankine-Hugoniot relations. The evolution of the remaining quantity J_{2^+} is to be determined using the last green thread just arriving at the shock. *The description is reminiscent of Whitham's characteristic rule! And, it is also the point of departure from the CCW formulation; hence, what follows may justifiably be labelled CCW*$^+$.

Equations (7.1) and (7.2) give the rate of desired variables along the three threads. To determine the correct differential relation valid locally along the

determine the jumps $[J_\pm]_1^2$ and $[s]_1^2$ precisely.

strand, a rotation must be performed. That is to say, the $\mathbf{D}_{\pm}(J_{\pm})$ and $\mathbf{D}(s)$ must be transformed into $\mathbf{D}_{\sigma}(J_{\pm})$ and $\mathbf{D}_{\sigma}(s)$. Carrying out the transformation, one readily obtains:

$$\mathbf{D}_{\sigma}() \equiv ()_t + u_s\,()_x \tag{7.3}$$

$$= ()_t + \frac{u_s}{2c}(\mathbf{D}_{+}() - \mathbf{D}_{-}()) \tag{7.4}$$

$$= \mathbf{D}() + (u_s - u)\,()_x \tag{7.5}$$

$$= \mathbf{D}_{\pm}() + (u_s - (u \pm c))\,()_x \tag{7.6}$$

$$= \frac{u_s - (u-c)}{2c}\mathbf{D}_{+}() - \frac{u_s - (u+c)}{2c}\mathbf{D}_{-}() \tag{7.7}$$

Explicitly applying the last operator (7.7) to the quantity J_{2^+}, it reads:

$$\mathbf{D}_{\sigma}(J_{2^+}) = \frac{u_s - (u_2 - c_2)}{2c_2}\mathbf{D}_{+}(J_{2^+}) - \frac{u_s - (u_2 + c_2)}{2c_2}\mathbf{D}_{-}(J_{2^+}) \tag{7.8}$$

Note that the coefficients appearing in front of the $\mathbf{D}_{\pm}()$ operators are *known* quantities at any given time moment (in the manner of an IVP). Their physical meaning will be interpreted later on. The *first* quantity $\mathbf{D}_{+}(J_{2^+})$ is just the rate of growth of Riemann's positive characteristic variable approaching the shock and it is given by (7.1), which was obtained by rotating the governing equations along the C_+ direction. Operating on s_2 with (7.5) and with (7.6), and rewriting it explicitly in physical variables, one obtains:

$$\mathbf{D}_{+}(J_{2^+}) = \frac{-(\gamma-1)(J_{2^+}^2 - J_{2^-}^2)\partial_x(A_2)}{8\,A_2} + \frac{(\gamma-1)^2(J_{2^+} - J_{2^-})^2\partial_x(s_2)}{16\,\gamma R} + f \tag{7.9}$$

$$= -\frac{c_2 u_2}{A_2}A_x + \frac{c_2^2}{\gamma R(u_s - u_2)}\mathbf{D}_{\sigma}(s_2) + f \tag{7.10}$$

$$= -\frac{c_2 u_2}{A_2}A_x + \frac{c_2}{\gamma R}\mathbf{D}_{+}(s_2) + f \tag{7.11}$$

The above three expression are *identical* and *exact* for isentropic flow, except for the rotation performed on the direction of entropy variation. These equivalent, and exact expressions suggest different opportunities for approximation. The last form is the one used for further developments below, as it leads to the simplest approximation.

Returning once again to the thread analogy, imagine the magnitudes of $J_{\pm}$ as the thickness of the respective threads, *i.e.*, their stretching quality. Note that the stretching is a linear function of their physical speed in the (x, t) space and that larger magnitudes of A_x/A and and f and s_x would tend to accelerate the stretching. Then, in (7.8), the *second* quantity $\mathbf{D}_{-}(J_{2^+})$ describes how the thickness of the green threads varies as one traces forward along the blue cross-thread. There does not appear to be any obvious way to evaluate this term accurately; if the $\mathbf{D}_{-}(J_{2^+})$ term was evaluated exactly, then there would be no approximation needed, and the shock motion would be described exactly! As expected, an approximation must be made.

Recall, the earlier analogy made on Page 62, where it was noted that if all disturbances originate on the right, then a simple wave results with constancy of two of the Riemann variables. In our analogy, the threads do not become stretched over time, and each one maintains a constant thickness; all green threads have the same thickness; all red threads have the same thickness; but each blue thread originating on the right has a slightly different thickness, though it remains constant thereafter. Here, and in general however it is not the case, for J_{2^+} varies as a result of non-homogeneities A_x, s_x, and f. However, if we assume that variation in J_{2^+}, *along* the C_{-} waves leaving the shock is negligible then the situation is greatly simplified. Note, the assumption is *not* that J_{2^+} is constant everywhere, or that it is constant along the shock, but that it is nearly so *along* the

C_- *at* the downstream strand, *i.e.*, just downstream of the shock wave, along the blue threads the thickness of the green cross-threads does not change appreciably. Whenever this assumption is valid, then the second term in (7.8) vanishes and the expression may be greatly simplified.

Returning yet again to (7.8), as noted already, the coefficients appearing in front of the $\mathbf{D}_{\pm}()$ operators are *known* quantities at any given time moment. Their physical meaning may be interpreted as $\frac{\partial t_+}{\partial t_s}$ and $\frac{\partial t_-}{\partial t_s}$, respectively, such that:

$$\mathbf{D}_{\sigma}() = \frac{\partial()}{\partial t_s} = \frac{\partial t_+}{\partial t_s}\frac{\partial()}{\partial t_+} + \frac{\partial t_-}{\partial t_s}\frac{\partial()}{\partial t_-}. \tag{7.12}$$

This is suggestive of a geometric interpretation, *viz.*, that a locally Euclidean triangle is formed in the fabric over (x,t) space by the blue and green threads with the strand as the hypotenuse. Then, applying (7.8) locally is equivalent to approximating the fabric as a two-manifold, as originally assumed.

Applying (7.8) to (7.11), and letting $\mathbf{D}_-(J_{2^+}) = 0$, one directly obtains:

$$[1, 0, A_{13}] \cdot \mathbf{D}_{\sigma}([J_{2^+}, J_{2^-}, s_2]) = b_1 \tag{7.13}$$

where,

$$A_{13} = -\frac{c_2}{\gamma R}$$

and

$$b_1 = \left(-\frac{c_2 u_2}{A}A_x + f\right)\partial_{t_s} t_+.$$

The choice of notation here is very convenient both for derivations and for practical calculations; this will become clear shortly. Here, b_1 is the right hand side which forces the evolution $\mathbf{D}_{\sigma}()$ of the state vector $[J_{2^+}, J_{2^-}, s_2]$ along the fault.

Similarly, an implicit relation for $\mathbf{D}_{\sigma}(J_{2^-})$ and $\mathbf{D}_{\sigma}(s_2)$ can be obtained most

easily by differentiating the Rankine-Hugoniot relations with respect to shock Mach number and then relating $\mathbf{D}_\sigma(M_s)$ to entropy $\mathbf{D}_\sigma(s_2)$ using (I.111). Consider for a moment (I.105) which is the same quantity as (I.108). Differentiating (I.108) one obtains:

$$[1, 1, A_{23}] \cdot \mathbf{D}_\sigma([J_{2^+}, J_{2^-}, s_2]) = b_2 \tag{7.14}$$

where,

$$A_{23} = \frac{-4c_1}{\gamma+1}\left(1 + \frac{1}{M_s^2}\right)\partial_s M_s,$$

and

$$b_2 = 2\,\mathbf{D}_\sigma(u_1) + \frac{4}{\gamma+1}\left(M_s - \frac{1}{M_s}\right)\mathbf{D}_\sigma(c_1).$$

Similarly, differentiating (I.96) which is the square of (I.100), gives:

$$[1, -1, A_{33}] \cdot \mathbf{D}_\sigma([J_{2^+}, J_{2^-}, s_2]) = b_3 \tag{7.15}$$

where,

$$A_{33} = \frac{-4c_1}{\gamma+1}\frac{\partial}{\partial M_s}\left(\frac{c_2}{c_1}\right)\partial_s M_s,$$

and

$$b_3 = 2\,\mathbf{D}_\sigma(u_1) + \frac{4}{\gamma+1}\left(M_s - \frac{1}{M_s}\right)\mathbf{D}_\sigma(c_1).$$

As suggested, leaving (7.13), (7.14), and (7.15) unaltered, it is convenient to assemble the three differential equations into a linear system of the form $\mathbf{A}\cdot\mathbf{x} = \mathbf{b}$:

$$\begin{bmatrix} 1 & 0 & A_{13} \\ 1 & 1 & A_{23} \\ 1 & -1, & A_{33} \end{bmatrix} \mathbf{D}_\sigma \begin{pmatrix} J_{2^+} \\ J_{2^-} \\ s_2 \end{pmatrix} = \begin{pmatrix} b_1 \\ b_2 \\ b_3 \end{pmatrix} \tag{7.16}$$

Hence, given the initial state $\mathbf{x}(\mathbf{0}) = [J_{2^+}, J_{2^-}, s_2]_0$ *and the right hand side forcing function, the IVP is easily integrated as* $\mathbf{x}(\mathbf{t}) = \int_\sigma \mathbf{A^{-1}b}\, dt + \mathbf{x_0}$. The upstream state $[J_{1^+}, J_{1^-}, s_1]$ is obtained in an analogous fashion, using the lifting isentrope model.

It is important to recognize that the formulation is *not* akin to applying the method of characteristics. It is, just like CCW, *an approximate analytical description in differential form* that is supposed to hold along the shock trajectory. Indeed, it will be shown later on how (7.16) relates to CCW (5.8). The various cases from the preceding chapter are solved using above formulation next.

7.5 Example Scenarios—Revisited

For succinctness, in what follows the new formulation (7.16) is referred to as CCW$^+$. Removal of the singularity in CCW$^+$ is seen by analysis of the first coefficient in (7.8); because it is the ratio of times, it always carries a positive sign and further, it lies in the range $[0, 1]$ for all $M_s > 1$, and for arbitrary m_1. Comparison with the "case" results of the preceding chapter as well as other variations below demonstrate this point sufficiently.

7.5.1 Case I

Figure 7.2 shows results for the implosion problem described in §3.2.4. Note that the lower-right subplot in these figures shows the four Riemann variables $J_\pm$, instead of the shock Mach number as was done in the preceding chapter. Effectively, it is these variables which are integrated (along with s_2, which is directly related to M_s). The remaining subplots contain physical variables for consistency and easier comparison with the previous chapter. For the imploding

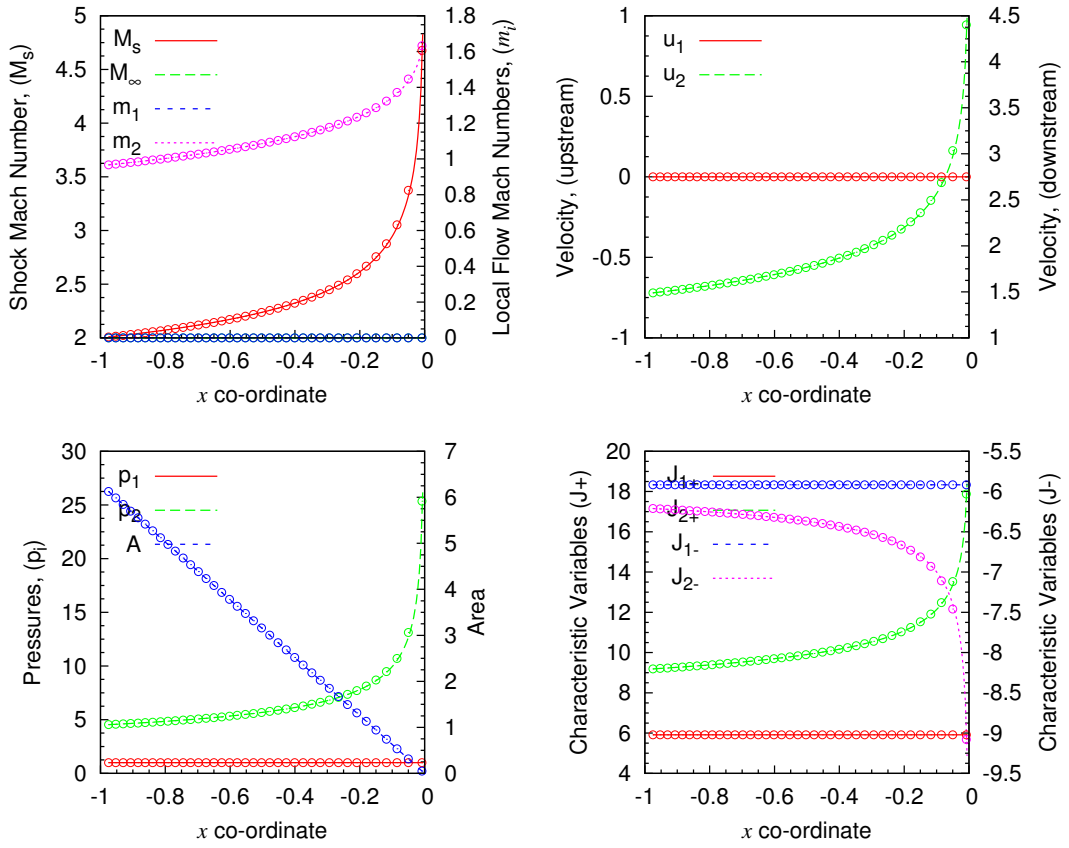

Figure 7.2: Case I: shock implosion problem (§3.2.4), comparison between CCW$^+$ (solid) and Asterix (circles). Cylindrical geometry, uniform, quiescent gas ahead of the shock wave, $\gamma = 1.4$. The parameters are plotted as a function of shock location. The agreement is considered excellent.

shock case, the CCW$^+$ approximation appears to provide results which are in excellent agreement with the Asterix solution.

7.5.2 Case II

Referring to Figure 7.3, for the second test case from previous chapter, the CCW$^+$ formula (7.16) clearly does not provide as good an approximation as it did for the imploding shock problem. Recall that CCW (5.8) also exhibited a slightly larger

discrepancy for this case.

However, it is possible to obtain much better agreement for this case by using a different approximation as shown in Figure H.1 in Appendix H. It turns out that for this case, if the term A_{13} is multiplied by the dimensionless ratio $c_2/(u_2 - c_2)$, then excellent agreement exists; while no satisfactory explanation or justification has been found, it is reported here as a fact for future reference only, and hence, it should *not* be judged as an *improvement* over the more general and justifiable result of (7.16).

7.5.3 Case III

Recall this case is similar to the previous one, except that a non-zero body force is present ($f = 1$). Referring to Figure 7.4, the level of agreement is exactly similar to the scenario presented above in Case II. Also, as before modifying the $A13$ term by multiplying it with the non-dimensional ratio $c_2/(u_2 - c_2)$, dramatically improves the accuracy. This case was also tested for various other values of f, including $f = 10$ as shown in Figure H.2 in Appendix H; the agreement with Asterix is found to be similar or slightly better than the present case.

7.5.4 Case IV

Referring to Figure 7.5, for the fourth test case from previous chapter, the CCW$^+$ formula (7.16) clearly does not provide a good approximation. The trends are physically correct, except the shock moves faster than the true solution. Incidentally, the same case also arises when the inlet *fails to start*; this occurs in "Case VI" in connection to membrane rupture, and in "Case VII" in connection to accelerative starting. In the preceding chapter this scenario was included as a separate

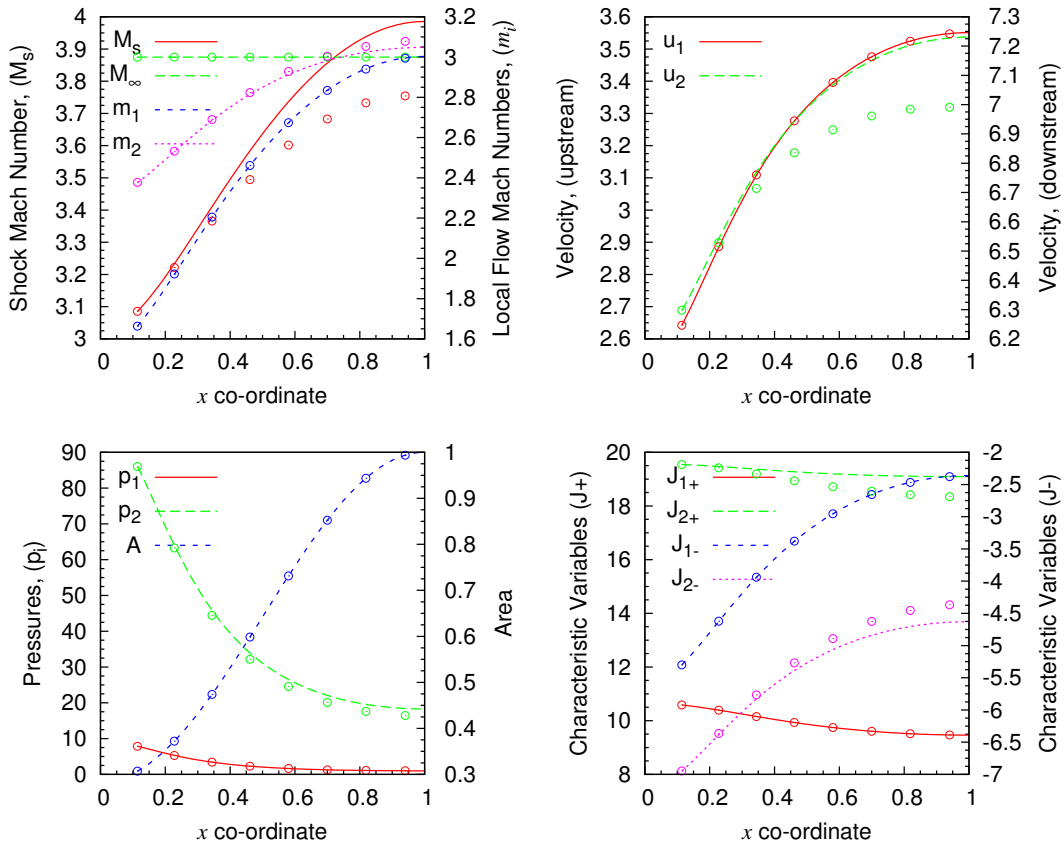

Figure 7.3: Case II: a left moving diverging channel encounters a right facing shock wave, $M_s \simeq 3$; comparison between CCW$^+$ (7.16) (solid) and CFD (circles); non-uniform, non-quiescent gas ahead of shock, no body force present ($f = 0$); m_∞ refers to $m(x = L) = const$; Smooth geometry model: M_D3, $IoS = 0.1$. The agreement is considered fair; the discrepancy appears in J_{2^-} and J_{2^+} in the lower-right subplot.

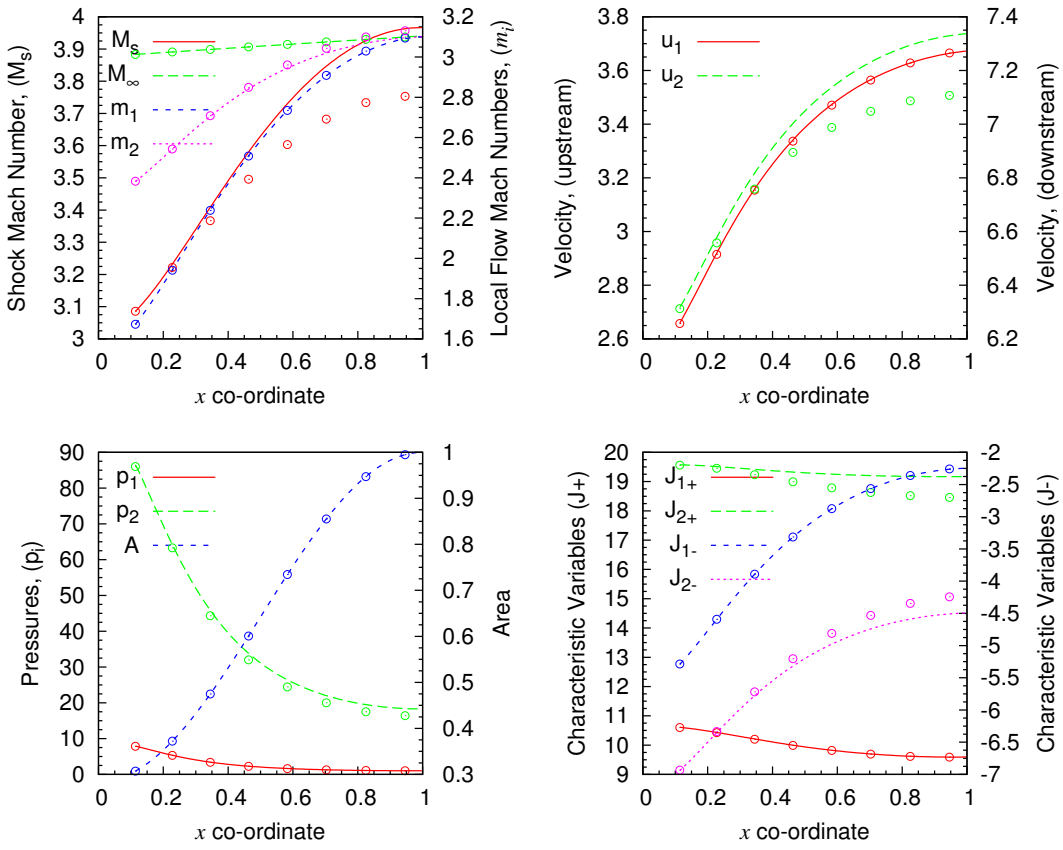

Figure 7.4: Case III: a left moving diverging channel encounters a right facing shock wave, $M_s \simeq 3$; comparison between CCW$^+$ (7.16) (solid) and CFD (circles); non-uniform, non-quiescent gas ahead of shock, non-zero body force present ($f = 1$); m_∞ refers to $m(x = L) = const$; Smooth geometry model: M_D3, $IoS = 0.1$. The agreement is considered fair; the key discrepancy appears in J_{2^-} and J_{2^+} in the lower-right subplot.

case, because the singularity in CCW prevented its natural occurrence. Recall that the accuracy of the CCW for this case was found to be truly surprising.

7.5.5 Case V

Referring to Figure 7.6, for the fifth test case of previous chapter, the CCW$^+$ approximation appears to provide excellent agreement with the Asterix solution. The level of agreement is similar to the earlier CCW solution; except for the u_2 plot, the two (CCW and CCW$^+$) solutions appear so similar at first glance, that it is difficult to distinguish between these.

7.5.6 Case VI

This scenario is related to impulsive intake flow (§1.3.2.2) which occurs following the rupture of a membrane. Recall that for the membrane rupture case shown in preceding chapter, the CCW theory exhibits singular behaviour.

Figures 7.7 and 7.8 show the solution for two different scenarios obtained using CCW$^+$ and compared against Asterix. The first figure is for $M_D = 3$, $IoS = 0.8$, *without* low internal pressure inside the intake before rupture $p(x < L, t_0)/p_\infty = 1$. In this case it is seen (Figure 7.7) that the intake fails to start.

The second case is for $M_D = 3$, $IoS = 0.9$, *with* low internal pressure inside the intake before rupture $p(x < L, t_0)/p_\infty = 0.5$. In this case it is seen (Figure 7.8) that the intake impulsively starts following the membrane rupture.

While CCW$^+$ is not singular and it is able to predict the correct net outcome for this case, the solution must still be considered poor in terms of agreement with Asterix. On the one hand the poor agreement is not surprising, because this case involves strong interaction between the downstream flow and the shock wave.

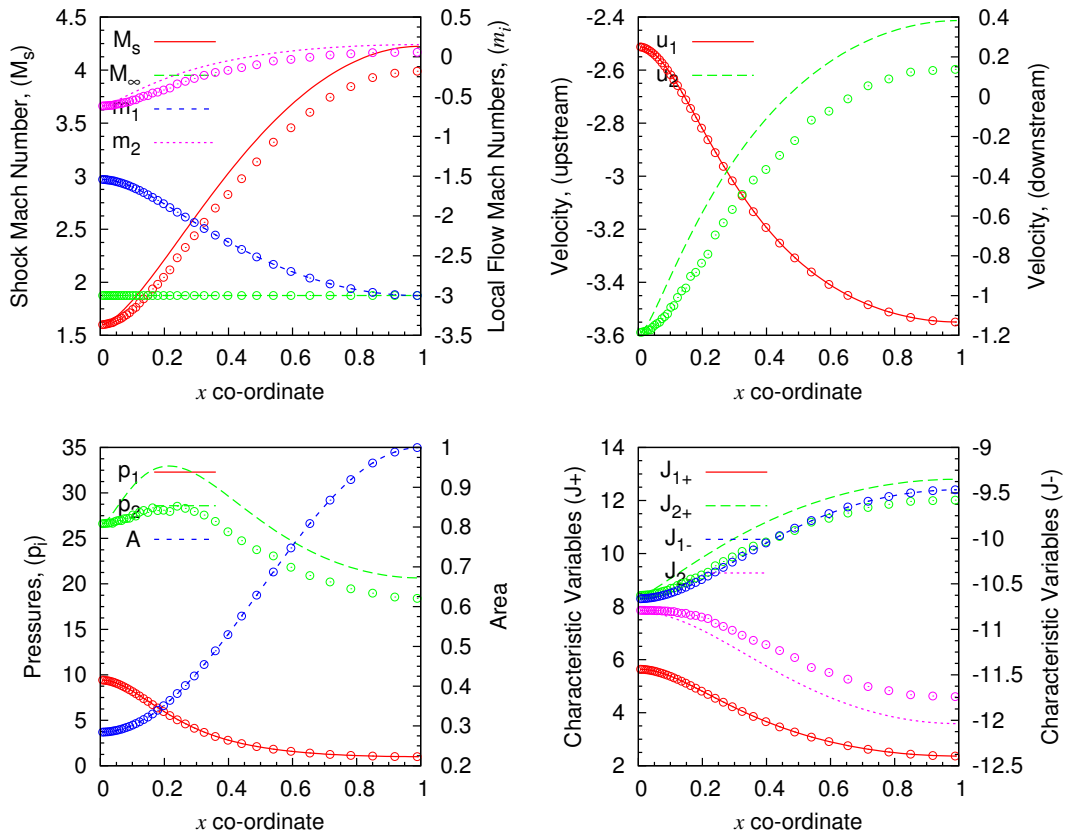

Figure 7.5: Case IV: Unstarting of an inlet; comparison is shown between CCW$^+$ (solid) and CFD (circles); smooth geometry model: M_D3, $IoS = 0.1$. The agreement is considered fair; recall, CCW gives virtually exact agreement in this case. Also, it is should be noted that generally speaking, for a stronger initial disturbance at the back (*e.g.*, $M_s = 3$ instead of $M_s = 1.6$) the agreement will be better.

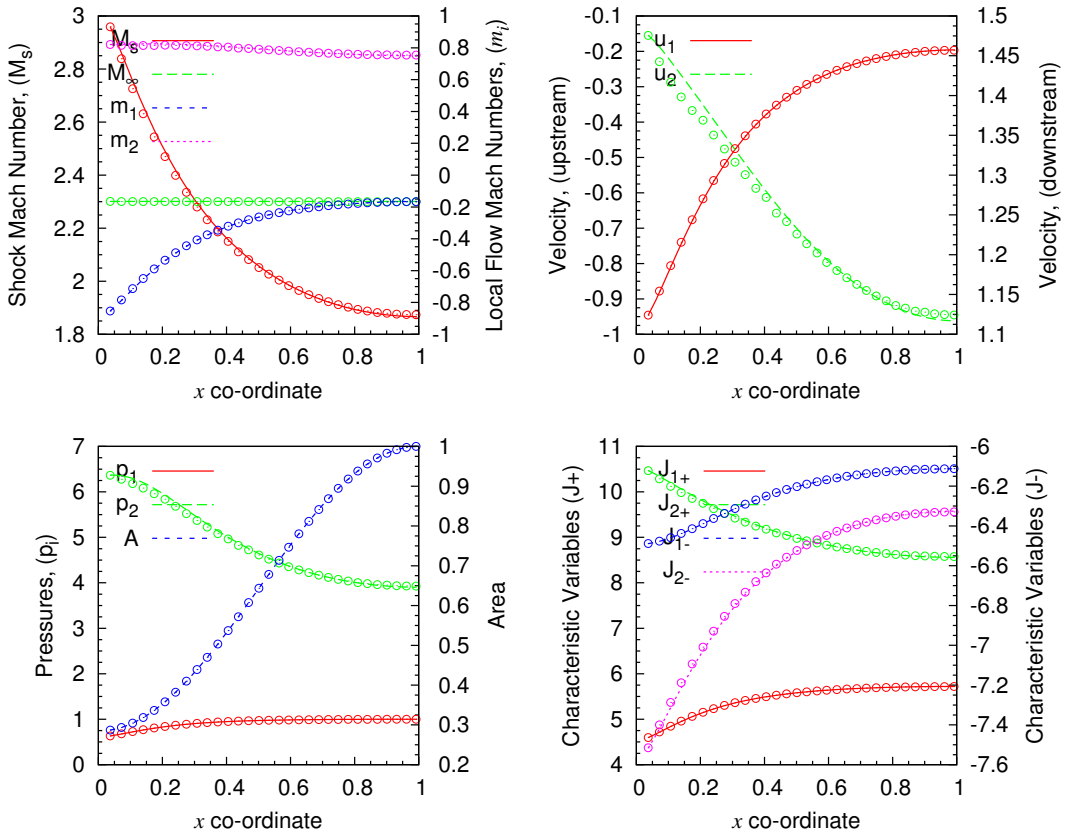

Figure 7.6: Case V: Leftward upstream subsonic flow, rightward downstream subsonic flow; comparison is shown between CCW$^+$ (solid) and CFD (circles); smooth geometry model: M_D3, $IoS = 0.1$. The agreement is considered excellent.

On the other hand, the solution is remarkable in that the simple CCW$^+$ relation admits such complex *reversible* shock motion, with overall trends in qualitative agreement with the full solution of the governing equations obtained using Asterix.

7.5.7 Case VII

This scenario is related to impulsive intake flow (§1.3.2.1) which occurs following accelerative motion of the channel. Comparing the CCW$^+$ results with those of CCW from the previous chapter, it is evident (Figure 7.9) that no singularity exists. However the solution exhibits poor accuracy in comparison with the more accurate result obtained from the full solution of the quasi-one-dimensional Euler equations. As with "Case II" above, a simple modification which dramatically improves the overall accuracy is noteworthy; the modification involves the acceleration term which is removed (decoupled) from the forcing function, *i.e.*, from the b_1 term in (7.13). It is however allowed to modify the upstream state through changes in m_∞ using the lifting isentrope model; no justification has been found, and the term must be present for other cases ("Case III" requires it). This should be seen as an additional approximation which seems to be beneficial for improving the accuracy in the accelerative starting scenarios. Some solutions obtained in this way, for different inlet contractions ($IoS = 0.5$, and $IoS = 0.1$) and for different accelerations ($f = -1.5$, $f = -3.6$), are shown in Figures H.3, H.4, H.5, and H.6 in Appendix H. It is noted that the model appears to predict the final outcome rather well, and considering the complexity of the problem such agreement may be considered good for this simple model.

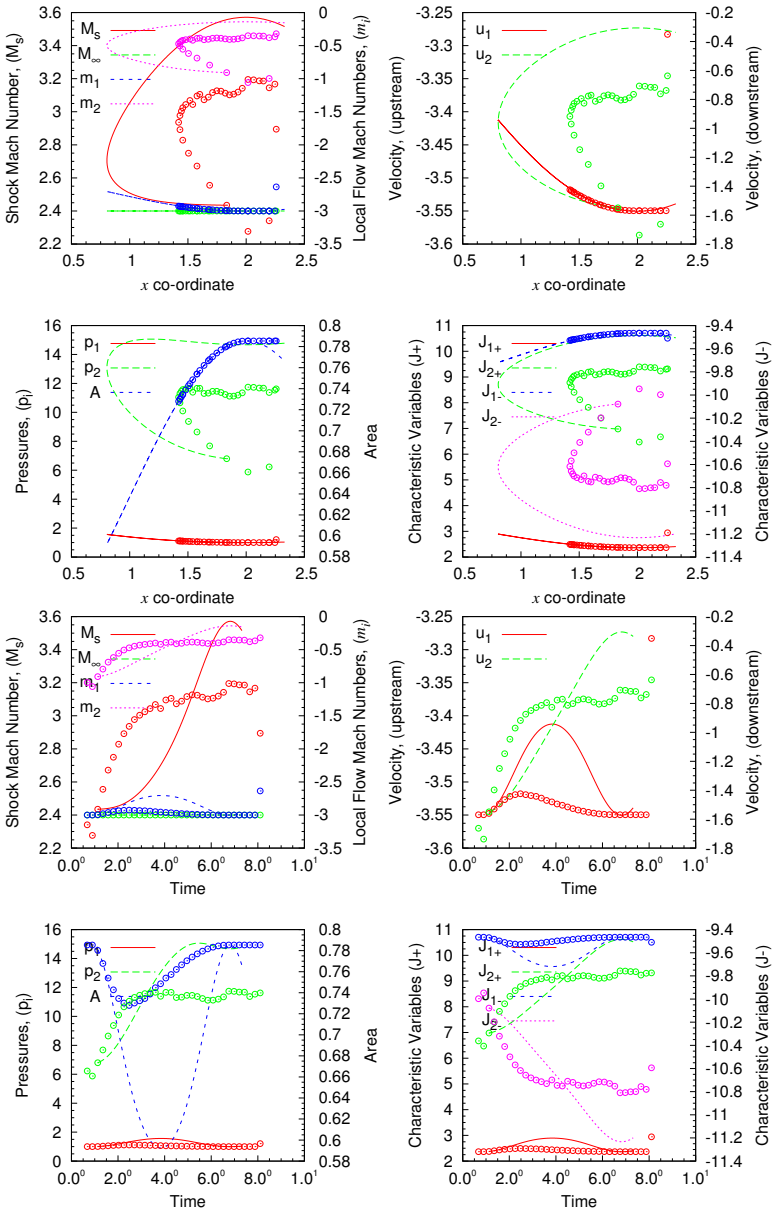

Figure 7.7: Case VI: Impulsive flow starting scenario (membrane rupture, intake fails to start, $M_D 3$, $m_\infty = -3$, IoS0.8, $p(x < L, t = 0)/p_\infty = 1.0$). Recall that CCW exhibits singular behaviour for this case. While CCW$^+$ is not singular and it is able to predict the correct net outcome for this case, the solution must still be considered poor in terms of agreement with Asterix. However, it is remarkable that the simple CCW$^+$ relation admits such complex *reversible* shock motion, with overall trends in agreement with the full solution of the governing equations obtained using Asterix.

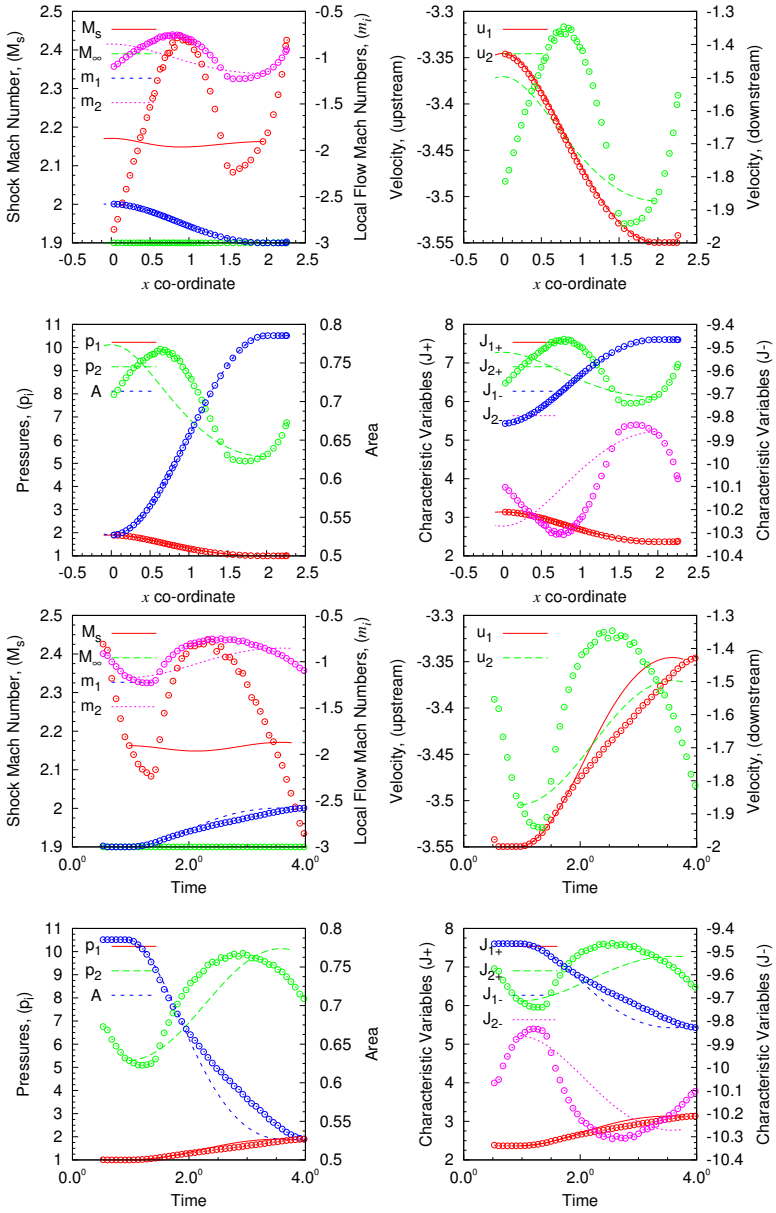

Figure 7.8: Case VI: Impulsive flow starting scenario (membrane rupture, intake starts, M_D3, $m_\infty = -3$, $IoS = 0.9$, $p(x < L, t = 0)/p_\infty = 0.5$). Recall that CCW exhibits singular behaviour for this case. While CCW$^+$ is not singular and it is able to predict the correct net outcome for this case, the solution must still be considered poor in terms of agreement with Asterix. This is to be expected considering that the entire wave structure and the concomitant information originating from the downstream direction is discarded in CCW$^+$.

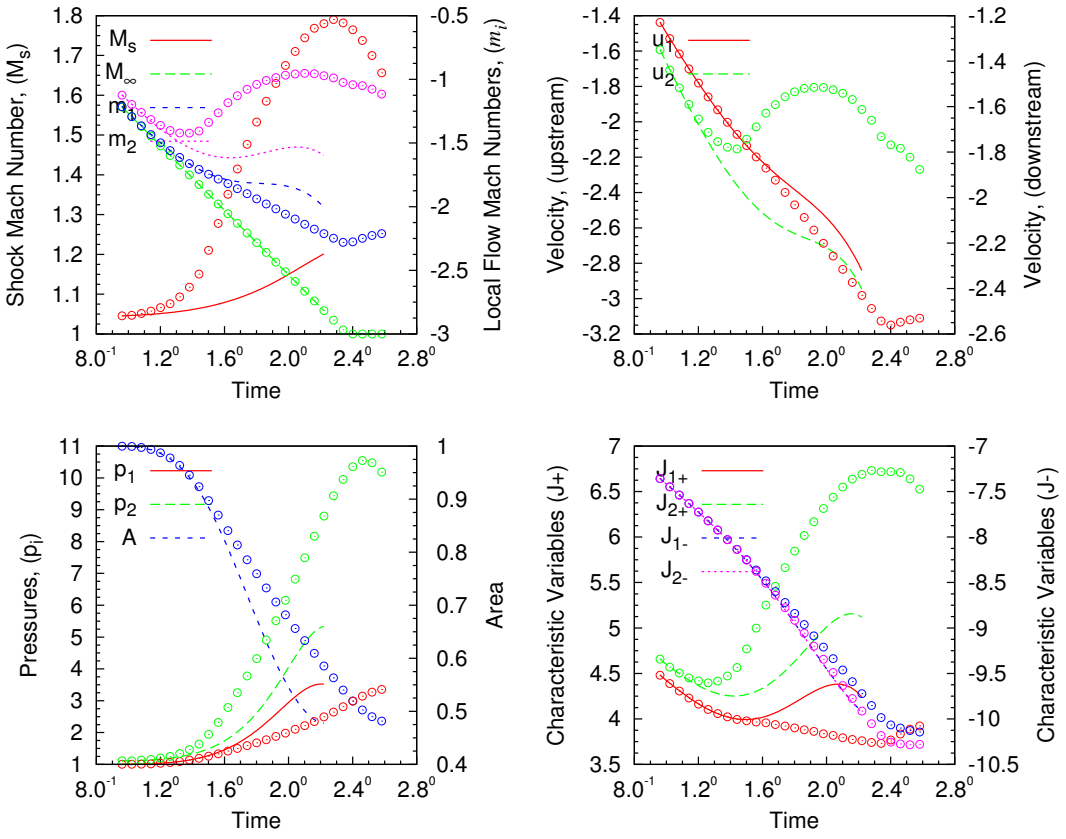

Figure 7.9: Case VII: Accelerative starting scenario. Comparison between CCW$^+$ and the full solution of the quasi-one-dimensional governing equations obtained using Asterix. While CCW$^+$ is not singular and it is able to predict the correct net outcome for this case, the solution must still be considered poor in terms of agreement with the more accurate result from Asterix.

7.6 Some Observations

At first sight, the differences or even the similarities between the CCW$^+$ theory and the classical characteristic rule are not obvious. It was hinted at the end of §7.1 and indeed established in §7.3 that the fault analogy naturally suggests a derivation like the characteristic rule. Both theories lead to a differential equation, and although CCW$^+$ gives a differential system, the 3×3 matrix is trivial to invert analytically. However, it does not appear to be practicable to relate the theories in this way. The task may be achieved in a much simpler way, by carefully retracing the steps taken in deriving CCW$^+$. After some analysis, it turns out that the *only*[*] distinguishing feature between the theories is as follows.

Whereas the CCW$^+$ leads to the system (7.16) with:

$$b_1 = \left(-\frac{c_2 u_2}{A} A_x + f\right) \frac{dt_+}{dt_s}$$

the CCW relation (5.8) is equivalent to the system (7.16), but with:

$$b_1 = \left(-\frac{c_2 u_2}{A} \frac{u_s}{u_2 + c_2} A_x + f\right). \tag{7.17}$$

Hence, ignoring the f term for a moment,[†] then the traditional characteristic rule actually uses a mapping of the C_+ onto the shock using:

$$\frac{dt_+}{dt_s} = \frac{u_s}{u_2 + c_2}. \tag{7.18}$$

In hindsight, that may now seems obvious! but, going in the reverse direction from a well regarded and well tested theory to discover the physical significance

[*] *i.e.*, other than their psychological origins.

[†] This term is zero in most scenarios treated above and in the literature known to the author.

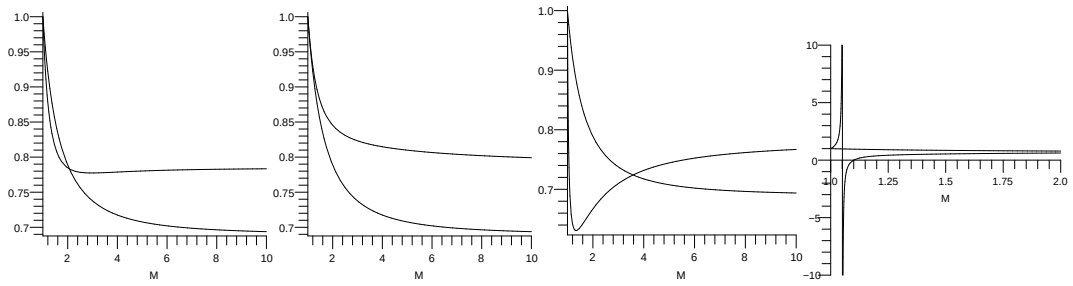

Figure 7.10: Comparison between (7.18) and the expression derived here. $\gamma = 1.4$. From left to right, $m_1 = [0, 1, -0.9, -1.1]$. For large M_s the term from (7.16) gives $\simeq 0.689$, whereas (7.18) gives $\simeq 0.784$. The former is always well behaved and independent of m_1.

of $u_2 + c_2 = 0$ proves rewarding enough. The proper $\frac{\partial t_+}{\partial t_s}$ is as given earlier, and where the f term is non-zero, there does not seem to be any justification for not including it in the multiplicand. Comparison between these function is presented in Figure 7.10 for $m_1 = [0, 1, -0.9, -1.1]$. The dependence of (7.18) on m_1 is evident along with the appearance of a singularities for $m_1 < -1$.

Whereas the (7.18) is singular for various values of m_1 depending* on the shock Mach number, the coefficients in the relation (7.8) are always well behaved (these are in fact independent of m_1). Also, in the limit of a weak shock, both expressions agree. Note that for $m_1 = 0$ they are equal at $M_s \simeq 2$.

7.7 Summary

An approximate differential relation holding along the shock wave has been obtained using the smooth fabric analogy for the surfaces formed by the Riemann variables. The final result is labelled CCW$^+$.

It has been shown how the thought of substituting the positive characteristic

*Incidentally, it must be singular in the same manner as that described in Figure 6.1 where $u_2 + c_2 = 0$.

onto the shock seems like a natural consequence of the analogy. The analogy also leads to an easy derivation of an operator which is valid along the shock direction. Its application to the positive characteristic variable naturally suggests a simple assumption. By differentiating two of the Rankine-Hugoniot relations with respect to shock Mach number, the evolution of the Riemann states on either side of the shock wave is implicitly linked. Combining the three relations, a differential system is obtained. Its application is demonstrated by way of examples from the preceding chapter; using additional ones, it is shown that the above rule works quite well for a variety of problems.

The CCW$^+$ formulation does not contain any singularities when $u_2 + c_2 = 0$, and it is well behaved for any combination of M_s and m_1. After removal of the singularity, it has been shown how the method admits *reversible* shock behaviour, predicting both starting and unstarting. The qualitative behaviour is good, however quantitatively some further improvements must be sought.

The CCW$^+$ is shown to be very closely related to CCW; the differences and the similarities between the two theories are explained.

Chapter 8

Summary of Contributions and Conclusions

In the first part of the thesis, an analytical, numerical and experimental study was performed to assess the flow starting characteristics in an external-compression ramp-type intake. The analysis was performed within the configuration space, on either side of the critical condition where the intake was expected to self-start under quasi-steady flow conditions. This expectation was based on common understanding existing in the field, consistent with well-cited literature dealing with starting characteristics of supersonic intakes.

Through analytical and numerical modelling carried out in two space dimensions, it was concluded that the traditional model for predicting flow starting in the external compression intakes is insufficient for the ramp-type intakes; the existing popular model, based on one-dimensional flow across a planar shock, was shown to be inaccurate, especially when these intakes are supposed to start under conditions away from their specific design point.

To remedy this, a novel analytical model was proposed in the first part of

the thesis to predict off-design self-starting behaviour; its application was demonstrated for a particular two-shock ramp intake. The calculations were compared with the CFD results which further lend credence to the assumptions made in the analysis. Finally, some experimental evidence was presented which further supports the starting characteristics as predicted by the new analytical model. Taken together, it was concluded that these results (analytical, numerical, and experimental) constitute overwhelming evidence supporting the arguments forwarded here.

Hence, the single most important contribution made in the first part of the thesis is the argument made in favour of using *curved shock models for prediction of external-compression intakes.* Application of the basic idea was demonstrated for a particular two-shock inlet operating away from its design point.

In the second part of the thesis, an analytical and numerical study was performed to assess the feasibility of predicting shock dynamics inside an intake using a simple, approximate, yet representative model. The basic notion was driven by the fact that the flow starting phenomenon is inherently tied to shock motion inside the intake.

It was found that there is very little widely-available knowledge on impulsive flow starting in the literature, and that there is no systematic study describing the shock dynamics occurring inside supersonic intakes. Consequently, there is no existing theory for analytically predicting impulsive flow starting phenomena discussed in this work.

Hence, it was suggested to the author that the well-known Chester-Chisnell-Whitham (CCW) formulation for approximating shock dynamics might be extendible for application to impulsive flow starting phenomena occurring in supersonic intakes. Owing to the analytical nature of the work, the entire modelling

was carried out in the quasi-one-dimensional setting.

It was found that the usual problems studied in shock dynamics are much simpler than the present case. Firstly, the flow upstream of the moving wave is both non-uniform and unsteady. Secondly, the disturbances originating downstream of the shock play an important role in intake flows. Thirdly, the flow direction may be different than that of the shock wave. These facts presented as new challenges, unrelated to flow starting, but required sufficient attention before actual application of CCW could be made to intake flows. Only the first and the third points have been addressed here.

An analytical model was proposed for predicting unsteady flow inside the intake, upstream of the shock wave. It was shown to be highly accurate within the desired range of applicability. The model was termed lifting isentrope, and its comparison with time-accurate solution of the full governing equations was presented as conclusive evidence. Once the lifting isentrope model was coupled with the classical CCW formulation, it was concluded that the resulting model sufficiently resolved the first point made in the above para.

It was also found that CCW presented a singularity in most of the cases dealing with impulsive flow starting situations. The singularity was found to be related to situations where the upstream flow was in a direction opposite to that of the shock. For intake flows it is always the case that the flow is opposed to the shock. Hence, in general non-singular solutions could not be found until the source of the singularity was addressed.

There is little or no literature on this singularity. It was demonstrated that the usual singularity dealt with in the existing literature is of a different type. The limited knowledge available on this singularity was concluded to be false and not applicable in the present context. Time-accurate solution of the full governing

equations was presented as conclusive evidence supporting the last claim.

The source of the singularity was then studied; it was found that an analogy made between the surfaces formed of Riemann variables atop the space-time plane, and an imaginary smooth fabric containing three coloured threads, helped to visualize and also to resolve some of the mathematical difficulties. The novel formulation, labelled CCW$^+$, was proved to be *regular* in the desired range of applicability; *i.e.*, it was concluded to be non-singular for all upstream flows, opposed and not, and for all shock Mach numbers. It was concluded that this step sufficiently resolved the *third problem point* mentioned above.

Finally, some sample computations were presented in an effort to evaluate the CCW$^+$ range of application. It was found that qualitatively the theory gives correct behaviour of shock dynamics related to impulsive flow starting in supersonic intakes. However, quantitatively, there remains significant room for further improvement. For the classical applications, CCW$^+$ was demonstrated to be similar to CCW and explanations were provided in support of this point.

References

[1] `Asterix`, Software Package, Ver. 1.0.2.22, RBT Consultants, Toronto, ON, 2007.

[2] Courant, R. and Friedrichs, K. O., *Supersonic Flow and Shock Waves*, Interscience, 1st ed., 1948.

[3] Townend, L. H., "Research and Design for Hypersonic Aircraft," *Philosophical Transactions: Physical Sciences and Engineering*, Vol. 335, No. 1637, 1991, pp. 201–224.

[4] Waltrup, P. J., Anderson, G. Y., and Stull, F. D., "Supersonic combustion ramjet (scramjet) engine development in the United States," 3^{rd} *International Symposium on Air Breathing Engines, Munich, Germany*, 1976.

[5] Fry, R. S., "A Century of Ramjet Propulsion Technology Evolution," *AIAA Journal of Propulsion and Power*, Vol. 20, No. 1, January–February 2004, pp. 27–58.

[6] Canan, J. W., "Breathing new hope into hypersonics," *Aerospace America*, November 2007, pp. 26–31.

[7] Guy, R. W., Rogers, R. C., Puster, R. L., Rock, K. E., and Diskin, G. S., "The NASA Langley Scramjet Test Complex," AIAA Paper 96-3243, AIAA, 1996.

[8] Walsh, P., Tahir, R., and Molder, S., "Boundary-layer Correction for the Busemann Hypersonic Air Inlet," *Canadian Aeronautics and Space Journal*, Vol. 49, No. 1, March 2003.

[9] Anderson, J. D., *Hypersonic and High Temperature Gasdynamics*, McGraw-Hill Book Company, 4th ed., 1989.

[10] VanWie, D. M., "Ch. 7 Scramjet Propulsion," *Scramjet Propulsion, Progress in Aeronautics and Astronautics*, edited by E. T. Curran and S. N. B. Murthy, Vol. 189, AIAA, 2000, pp. 447–511.

[11] Bertin, J. J. and Cummings, R. M., "Fifty years of hypersonics: where we've been, where we're going," *Progress in Aerospace Sciences*, Vol. 39, 2003, pp. 511–546.

[12] Billig, F. S., "Supersonic combustion ramjet missile," *AIAA Journal of Propulsion and Power*, Vol. 11, No. 6, November–December 1995, pp. 1139–1146.

[13] Stuckey, R. M. and Lewis, M. J., "Hypersonic Missile Requirements and Operational Tradeoff Studies," *AIAA Journal of Spacecraft and Rockets*, Vol. 40, No. 2, March–April 2003.

[14] Wie, D. M. V., DAlessio, S. M., and White, M. E., "Hypersonic Airbreathing Propulsion," *APL Technical Digest*, Vol. 26, No. 4, 2005.

[15] Shachtman, N., "Hypersonic Cruise Missile: America's New Global Strike Weapon," *Popular Mechanics*, January 2007.

[16] Smart, M. and Tetlow, M., "Orbital Delivery of Small Payloads Using Hypersonic Airbreathing Propulsion," AIAA Paper 2006-8019, AIAA, November 2006.

[17] Townend, L. H., "The Domain of the Scramjet," *Philosophical Transactions: Mathematical, Physical and Engineering Sciences*, Vol. 357, No. 1759, 1999, pp. 2317–2334.

[18] Cheng, S.-I., "Hypersonic Propulsion," *Progress in Energy and Combustion Science*, Vol. 15, 1989, pp. 183–202.

[19] Stalker, R. J., Paull, A., Mee, D. J., Morgan, R. G., and Jacobs, P. A., "Scramjets and shock tunnels—The Queensland experience," *Progress in Aerospace Sciences*, Vol. 41, 2005, pp. 271–513.

[20] Henry, J. R. and Anderson, G. Y., "Design considerations for the airframe-integrated scramjet." *First International Symposium on Air Breathing Engines, Marseille, France.*, 1971.

[21] O'Neill, M. K. L. and Lewis, M. J., "Design tradeoffs on scramjet engine integrated hypersonic waverider vehicles." *AIAA Journal of Aircraft*, Vol. 30, No. 6, 1993, pp. 943.

[22] Ferri, A., "Review of problems in application of supersonic combustion." *Journal of the Royal Aeronautical Society*, Vol. 68, No. 645, 1964, pp. 575–597.

[23] Finley, D., "Hypersonic aerodynamics considerations and challenges." AIAA Paper 90-5222, AIAA, 1990.

[24] Drummond, J. P., Cockrell, Jr., C. E., Pellett, G. L., Diskin, G. S., Auslender, A. H., Exton, R. J., Guy, R. W., Hoppe, J. C., Puster, R. L., Rogers, R. C., Trexler, C. A., and Voland, R. T., "Hypersonic Airbreathing Propulsion—An Aerodynamics, Aerothermodynamics, and Acoustics Competency White Paper," Tech. Rep. TM-2002-211951, NASA, 2002.

[25] Johnston, P. J., Cubbage, J. M., and Weidner, J. P., "Studies of engine-airframe integration on hypersonic aircraft." *AIAA Journal of Aircraft*, Vol. 8, No. 7, 1971, pp. 495–501.

[26] Benkmann, P., "Design techniques for integrated rocket - ram/scramjets." *Seventh International Symposium on Air Breathing Engines*, 1985, pp. 237–244.

[27] Lewis, M. J. and Takashima, N., "Engine/airframe integration for waverider cruise vehicles." AIAA Paper 93-0507, AIAA, 1993.

[28] Maudet, V. and Perrier, P., "Air intake integration by CFD at high Mach number." AIAA Paper 90-5205, AIAA, 1990.

[29] Gusev, V., Blagoveshchensky, N., and Zadonsky, S., "The integration of a hypersonic vehicle airframe with an airbreathing engine." AIAA Paper 93-5034, AIAA, 1993.

[30] Pulsonetti, M. V. and Stalker, R., "A study of scramjet scaling," AIAA Paper 96-4533, AIAA, November 1996.

[31] Anderson, G. Y., "An examination of injector/combustor design effects on scramjet performance." *Second International Symposium on Air Breathing Engines.*, 1974.

[32] Sun, M.-B., Wang, Z.-G., Liang, J.-H., and Geng, H., "Flame Characteristics in Supersonic Combustor with Hydrogen Injection Upstream of Cavity Flameholder," *AIAA Journal of Propulsion and Power*, Vol. 24, No. 4, July–August 2008, pp. 688–696.

[33] Ferri, A., "Mixing-controlled supersonic combustion." *Annual Review of Fluid Mechanics*, 1973, pp. 301–338.

[34] Billig, F. S. and Dugger, G. L., "The Interaction of Shock Waves and Heat Addition in the Design of Supersonic Combustors," *Twelfth Symposium (International) on Combustion, Pittsburgh, PA*, The Combustion Institute, 1969, p. 1125.

[35] Schetz, J. A., Billig, F. S., and Favin, S., "Approximate Analysis of Axisymmetric Supersonic Base Flows with Injection," *AIAA Journal*, Vol. 18, No. 8, 1980, pp. 867–868.

[36] Schetz, J. A., Billig, F. S., and Favin, S., "Flowfield analysis of a scramjet combustor with a coaxial fuel jet." *AIAA Journal*, Vol. 20, No. 9, 1982, pp. 1268–1274.

[37] Waltrup, P. J., "Liquid fueled supersonic combustion ramjets: a research perspective of the past, present and future," AIAA Paper 86-0158, AIAA, 1986.

[38] Billig, F. S., "Research on supersonic combustion." *AIAA Journal of Propulsion and Power*, Vol. 9, No. 4, 1993, pp. 499–514.

[39] Morgan, R. G. and Casey, R., "Supersonic combustion with transverse, circular wall jets." *Tenth International Symposium on Air Breathing Engines.*, 1991, pp. 1211–1219.

[40] Curran, E. T., Heiser, W. H., and Pratt, D. T., "FLUID PHENOMENA IN SCRAMJET COMBUSTION SYSTEM," *Annual Review of Fluid Mechanics*, Vol. 28, 1996, pp. 323–360.

[41] Baxter, M. R. and Lefebvre, A. H., "Flame stabilization in high-velocity heterogeneous fuel-air mixtures." *Tenth International Symposium on Air Breathing Engines.*, 1991, pp. 1011–1017.

[42] Jones, R. A. and Huber, P. W., "Toward scramjet aircraft." *Astronautics and Aeronautics*, Vol. February, 1978, pp. 38–48.

[43] Baysal, O., Engelund, W. C., Eleshaky, M. E., and Pittman, J. L., "Adaptive computations of multispecies mixing between scramjet nozzle flows and hypersonic freestream." AIAA Paper 89-0009, AIAA, 1989.

[44] Bakos, R., Tamagno, J., Rizkalla, O., Pulsonetti, M. V., Chinitz, W., and Erdos, J. I., "Hypersonic mixing and combustion studies in the GASL HYPULSE facility." AIAA Paper 90-2095, AIAA, 1990.

[45] Andrews, Jr., E. H., Torrence, M. G., Anderson, G. Y., Northam, G. B., and Mackley, E. A., "Langley Mach 4 scramjet test facility." Tech. Memo. NASA-TM/86277, NASA, 1985.

[46] Bobskill, G., Bittner, R., Riggins, D., and McClinton, C., "CFD evaluation of Mach 17 HYPULSE scramjet combustor data." AIAA Paper 91-5093, AIAA, 1992.

[47] Brescianini, C. P. and Morgan, R. G., "Nuumerical modeling of wall-injected scramjet models." *AIAA Journal of Propulsion and Power*, Vol. 9, No. 2, 1993, pp. 169–175.

[48] Buttsworth, D. R., Morgan, R. G., and Stalker, R. J., "Shock tunnel testing of a parametric scramjet engine." *International Aerospace Congress, Melbourne, Australia*, 1991.

[49] Chinzei, N., Komuro, T., Kudou, K., Murakami, A., Tani, K. andMasuya, G., and Wakamatsu, Y., "Effects of injector geometry on scramjet combustor performance." *Tenth International Symposium on Air Breathing Engines.*, 1991, pp. 1219–1227.

[50] Clark, R. L., Ng, W. F., Walker, D. A., and Schetz, J. A., "Large-scale structure in a supersonic slot-injected flow field." *AIAA Journal*, Vol. 28, No. 6, 1990, pp. 1045–1051.

[51] Drummond, J. P. and Weidner, E. H., "Numerical study of a scramjet engine flowfield." *AIAA Journal*, Vol. 20, No. 9, 1982, pp. 1182–1187.

[52] Ebrahami, H. B., "CFD validation for scramjet combustor and nozzle flows, part 1." AIAA Paper 93-1840, AIAA, 1993.

[53] Edwards, T. A., "The effect of exhaust plume/ afterbody interaction on installed scramjetperformance." Tech. Memo. 101033, NASA, 1988.

[54] Eklund, D. R., Northam, G. B., and Fletcher, D. G., "A validation study of the SPARK Navier-Stokes code for nonreactingscramjet combustor flowfields." AIAA Paper 90-2360, AIAA, 1990.

[55] Harloff, G. J., Lai, H. T., and Nelson, E. S., "Two-dimensional viscous flow computations of hypersonic scramjet nozzleflowfields at design and offdesign conditions." AIAA Paper 88-3280, AIAA, 1988.

[56] Hartill, W. R., "Analytical and experimental investigation of a scramjet inlet of quadriformshape," Technical Report AFAPL-TR-65-74, AF Aero Propulsion Laboratory, Wright-Patterson Air Force Base, Ohio, 1965.

[57] Billig, F. S., "SCRAM-A supersonic combustion ramjet missile." AIAA Paper 93-2329, AIAA, 1993.

[58] Billig, F. S., Waltrup, P. J., and Stockbridge, R. D., "Integral-rocket dual-combustion ramjets," *AIAA Journal of Spacecraft and Rockets*, Vol. 17, No. 5, September–October 1980, pp. 416–424.

[59] Veillard, X., Tahir, R., Timofeev, E., and Molder, S., "Limiting contractions for starting simple ramp-type scramjet intakes with overboard spillage," *AIAA Journal of Propulsion and Power*, Vol. 24, No. 5, September–October 2008, pp. 1042–1049.

[60] Wie, D. M. V., Kwok, F. T., and Walsh, R. F., "Starting characteristics of supersonic inlets," AIAA Paper 96-2914, AIAA, July 1–3 1996.

[61] Trexler, C. A., "Inlet Starting Predictions for Sidewall-compression Scramjet Inlets," AIAA Paper 88-3257, AIAA, 1988.

[62] Kantrowitz, A. and Donaldson, C., "Preliminary Investigation of Supersonic Diffusers," Adv. confid. report L5D20, NACA, May 1945.

[63] Evvard, J. C. and Blakey, J. W., "The use of perforated inlets for efficient supersonic diffusion," Research Memo. E7C26, NACA, June 1947.

[64] Kantrowitz, A., "The formation and stability of normal shock waves in channel flows," Tech. Note 1225, NACA, March 1947.

[65] Molder, S., Timofeev, E., and Tahir, R., "Flow Starting in High Compression Hypersonic Air Inlets by Mass Spillage," AIAA Paper 2004-4130, AIAA, 2004.

[66] Yu, D., Chang, J., Bao, W., and Xie, Z., "Optimal Classification Criterions of Hypersonic Inlet Start/Unstart," *AIAA Journal of Propulsion and Power*, Vol. 23, No. 2, March–April 2007, pp. 310–316.

[67] Walker, S., Rodgers, F., Paull, A., and Wie, D. M. V., "HyCAUSE Flight Test Program," AIAA Paper 2008-2580, AIAA, 2008.

[68] Shapiro, A. H., *The Dynamics and Thermodynamics of Compressible Fluid Flow*, Wiley and Sons, New York, 1953.

[69] Hermann, R., *Supersonic Inlet Diffusers and Introduction to Internal Aerodynamics*, Minneapolis-Honeywell Regulator Company, 1st ed., 1956.

[70] Oates, G. C., *The Aerodynamics of Gas Turbine and Rocket Propulsion*, AIAA Education Series, AIAA, Washington, D.C., revised edition ed., 1988.

[71] Seddon, J. and Goldsmith, E. L., *Intake Aerodynamics*, AIAA Education Series, AIAA, New York, revised edition ed., 1985.

[72] Hunczak, H. R. and Kremzier, E. J., "Characteristics of perforated diffusers at free-stream Mach number 1.90," Research Memo. E50B02, NACA, May 1950.

[73] Clark, J. P. C., "An Experimental Investigation of a Supersonic Two-Dimensional Perforated Inlet at a Nominal Free-Stream Mach Number of 2.50," Tech. Note 24, UTIA, 1958.

[74] Wu, J. H. T., "An Experimental Study of Perforated Intake Diffusers at a Free-Stream MachNumber of 2.50," Tech. Note 69, UTIA, 1960.

[75] Scherrer, R. and Anderson, W., "Investigation of the performance and internal flow of a variable-area, variable-internal-contraction inlet at Mach numbers of 2.00, 2.50, and2.92," Research Memo. A58C24, NACA, July 1958.

[76] Smart, M. K. and Trexler, C. A., "Mach 4 Performance of Hypersonic Inlet with Rectangular-to-Elliptical Shape Transition," *AIAA Journal of Propulsion and Power*, Vol. 20, No. 2, March–April 2004, pp. 288–293.

[77] Tahir, R., Molder, S., and Timofeev, E. V., "Unsteady Starting of High Mach Number Air Inlets—A CFD Study," AIAA Paper 2003-5191, AIAA, 2003.

[78] Mossman, E. and Pfyl, F. A., "An experimental investigation at Mach numbers from 2.1 to 3.0 of circular-internal-contraction inlets with translating centerbodies," Research Memo. A56G06, NACA, October 1956.

[79] Ferri, A. and Nucci, L. M., "Theoretical and Experimental Analysis of Low-Drag Supersonic Inlets Having a Circular Cross Section and a Central Body at Mach Numbers of 3.30, 2.75, and 2.45," Research Memo. L8H13, NACA, 1948.

[80] Scherrer, R. and Gowen, F. E., "PRELIMINARY EXPERIMENTAL INVESTIGATION OF A VARIABLE-AREA, VARIABLE-INTERNAL-CONTRACTION AIR INLET AT MACH NUMBERS BETWEEN 1.42 AND 2.44," RM A55F23, NACA, September 1955.

[81] Tahir, R. B., *Starting and Unstarting of Hypersonic Air Inlets*, MASc Thesis, Ryerson University, 2003, National Library of Canada. ISBN: 061285325X.

[82] Najafiyazdi, A., Tahir, R., Timofeev, E., and Molder, S., "Analytical and Numerical Study of Flow Starting in Supersonic Inlets by Mass Spillage," AIAA Paper 2007-5072, AIAA, 2007.

[83] Wie, D. V. and Mölder, S., "Application of Busemann Inlet Designs for Flight at Hypersonic Speeds," AIAA Paper 92-1210, AIAA, 1992.

[84] Ferri, A., "Application of the method of characteristics to supersonic rotational flow," Report 841, NACA, 1946.

[85] Ferri, A. and Nucci, L. M., "PRELIMINARY INVESTIGATION OF A NEW TYPE OF SUPERSONIC INLET," Report 1104, NACA, 1952.

[86] Oswatitsch, K. I., "Pressure Recovery for Missiles with Reaction Propulsion at High Supersonic Speeds (The Efficacy of Shock Diffusers)," Tech. Memo. 1140, NACA, June 1947.

[87] Herrmann, D. and Triesch, K., "Experimental investigation of isolated inlets for high agile missiles," *Aerospace Science and Technology*, Vol. 10, 2006, pp. 659–667.

[88] Molder, S., Sullivan, P. A., Sislian, J. P., Gottlieb, J. J., McGregor, R. J., Paisly, T. W., Weston, S. C., Rogers, R. J., Hawboldt, R. J., Deschambault, R. L., Groth, C. P. T., Hawken, D. W., He, Z. D., Chen, L. W., and

Gordon, K. A., "Investigations in the fluid dynamics of scramjet inlets," Final Contract Report USAF, Contract No: F33615-87-C-2748; JHU, Contract No: APL 602235-0, Ryerson Polytechnic Institute and University of Toronto Institute for AerospaceStudies, 1992.

[89] Chester, W., "The Quasi-Cylindrical Shock Tube," *Philosphical Magazine*, 1954, pp. 1293–1301.

[90] Chisnell, R. F., "The Motion of a Shock Wave in a Chanel, with Applications to Cylindrical and Spherical Shock Waves," *Journal of Fluid Mechanics*, Vol. 2, 1957, pp. 286–298.

[91] Whitham, G. B., *Linear and Nonlinear Waves*, Wiley-Interscience, 1973.

[92] DRDC, "Trisonic Wind Tunnel, Defence RD Canada—Valcartier," .

[93] Jacobsen, L., Tam, C., Behdadnia, R., and Billig, F., "Starting and Operation of a Streamline-Traced Busemann Inlet at Mach 4," AIAA Paper 2006-4508, AIAA, 2006.

[94] Barber, T. J., Hiett, D., and Fastenberg, S., "CFD Modeling of the Hypersonic Inlet Starting Problem," AIAA Paper 2006-123, AIAA, 9–12 January 2006.

[95] Goldfeld, M. and Nestoulia, R., "Numerical and Experimental Studies of 3D Hypersonic Inlet," AIAA Paper 2003-14, AIAA, 6–9 January 2003.

[96] Tam, C.-J., Baurle, R. A., and Streby, G. D., "Numerical Analysis of Streamline-Traced Hypersonic Inlets," AIAA Paper 2003-13, AIAA, 2003.

[97] Goonko, Y. P., Latypov, A. F., Mazhul, I. I., Kharitonov, A. M., Yaroslavtsev, M. I., and Rostand, P., "Structure of Flow over a Hypersonic Inlet with Side Compression Wedges," *AIAA Journal*, Vol. 41, No. 3, March 2003, pp. 436–447.

[98] Yuan, Z. K., Dong, X. X., and Hui, X., "The parametric analysis and experimental investigation of sidewall compression inlet at Mach 5.3 in non-uniform incoming flow condition," AIAA Paper 95-2889, AIAA, 10–12 July 1995.

[99] Hudgens, J. A. and Trexler, C. A., "Operating characteristics at Mach 4 of an inlet having forward-swept, sidewall-compression surfaces," AIAA Paper 92-3101, AIAA, 1992.

[100] Timofeev, E., Tahir, R., and Molder, S., "On Recent Developments Related to Flow Starting in Hypersonic Air Intakes," AIAA Paper 2008-2512, AIAA, 2008.

[101] `SolverII`, Software Package, Ver. 2.30.2385, RBT Consultants, Toronto, ON, 2004.

[102] Tahir, R., Timofeev, E., Voinovich, P., and Molder, S., "Simulation of Inviscid, Unsteady Flows in Hypersonic Air Inlets Using an Adaptive, Unstructured, Multi-Block Method," *Computational Fluid Dynamics 2004*, Springer Berlin Heidelberg, July 2004, pp. 859–860.

[103] von Neumann, J., "Oblique Reflection of Shocks," Explosives Research Report, U.S. Bureau of Ordnance Rep. No. 12, U.S. Bureau of Ordnance, 1943.

[104] NACA AMES Research Staff, "Equations, Tables, and Charts for Compressible Flow," Tech. Report 1135, NACA, 1953.

[105] `3DViewer`, *One-, two-, and three-dimensional, structured and unstructured data visualization software for Windows®*, Software Package, Ver. 1.1.723, RBT Consultants, Toronto, ON, 2003.

[106] Smart, M. K., "Experimental testing of a hypersonic inlet with rectangular-to-elliptic shape transition," *AIAA Journal of Propulsion and Power*, Vol. 17, 2001, pp. 276–283.

[107] Darrigol, O. and Frischb, U., "From Newtons mechanics to Eulers equations," *Physica D*, 2008.

[108] Oliveira, A. R. E., "Eulers Contribution to Classical Mechanics," *12th IFToMM World Congress, Besanon (France)*, June 2007.

[109] Riemann, B., "Ueber die Fortpflanzung ebener Luftwellen von endlicher Schwingungsweite," *Aus dem achten Bande der Abhandlungen der Koniglichen Gesellschaft der Wissenschaften zu Gottingen*, 1860.

[110] Earnshaw, S., "On the Mathematical Theory of Sound," *Philosophical Transactions of the Royal Society of London*, Vol. 150, 1860, pp. 133–148.

[111] Lord Rayleigh, "Aerial Plane Waves of Finite Amplitude," *Proceedings of the Royal Society of London. Series A, Containing Papers of a Mathematical and Physical Character*, Vol. 84, No. 570, 1910, pp. 247–284.

[112] Stokes, G. G., "On a difficulty in the theory of sound," *Philosophical Magazine*, Vol. XXXIII, 1848, pp. 349–356.

[113] Zeldóvich, Y. and Raizer, Y., *Physics of Shock Waves and High-Temperature Hydrodynamic Phenomena*, Vol. 2, Academic Press, 1967.

[114] Taylor, G., "The Formation of a Blast Wave by a Very Intense Explosion I Theoretical Discussion," *Proceedings of the Royal Society of London Series A, Mathematical and Physical Sciences*, Vol. 201, No. 1065, March 1950, pp. 159–174.

[115] Taylor, G., "The Formation of a Blast Wave by a Very Intense Explosion II The Atomic Explosion of 1945," *Proceedings of the Royal Society of London Series A, Mathematical and Physical Sciences*, Vol. 201, No. 1065, 1950, pp. 175–186.

[116] Guderley, G., "Powerful Spherical and Cylindrical Compression Shocks in the Neighbourhood of the Centre and of the Cylinder Axis," *Luftfahrtforschung*, Vol. 19, 1942, pp. 302–312.

[117] Yousaf, M., "The Effect of Overtaking Disturbances on the Motion of Converging Shock Waves," *Journal of Fluid Mechanics*, Vol. 66, No. 3, 1974, pp. 577–591.

[118] Lazarus, R. B., "Erratum: Self-Similar Solutions for Converging Shocks and Collapsing Cavities," *SIAM Journal on Numerical Analysis*, Vol. 19, No. 5, 1982, pp. 1090–1090.

[119] Hafner, P., "Strong Convergent Shock Waves Near the Center of Convergence: A Power Series Solution," *SIAM Journal on Applied Mathematics*, Vol. 48, No. 6, 1988, pp. 1244–1261.

[120] Jones, C. W., "On the Propagation of Shock Waves in Regions of Non-Uniform Density," *Proceedings of the Royal Society of London Series A, Mathematical and Physical Sciences*, Vol. 228, No. 1172, 1955, pp. 82–99.

[121] Sakurai, A., "On the Problem of a Shock Wave Arriving at the Edge of a Gas," *Communications on Pure and Applied Mathematics*, Vol. 13, 1960, pp. 353–370.

[122] Whitham, G. B., "On the Propagation of Shock Waves Through Regions of Non-Uniform Area or Flow," *Journal of Fluid Mechanics*, Vol. 4, 1958, pp. 337–360.

[123] Han, Z. and Yin, X., *Shock Dynamics*, Kluwer Academic Publishers / Science Press, 1993.

[124] Chester, W., "The Propagation of Shock Waves in a Channel of Non-uniform Width," *The Quarterly Journal of Mechanics and Applied Mathematics*, Vol. 6, No. 4, 1953.

[125] Friedman, M. P., "An Improved Perturbation Theory for Shock Waves Propagating Through Non-uniform Regions," *Journal of Fluid Mechanics*, Vol. 8, 1960, pp. 193–209.

[126] Hayes, W. D., "Self-similar strong shocks in an exponential medium," *Journal of Fluid Mechanics*, Vol. 32, 1968, pp. 305–315.

[127] Rosaciszewski, J., "Calculations of the Motion of Non-uniform Shock Waves," *Journal of Fluid Mechanics*, Vol. 8, 1960, pp. 337–367.

[128] Fursenko, A. A., Oshima, K., Mende, N. P., Voinovich, P. A., Timofeev, E. V., and Sharov, D. M., "Numerical Simulation of Propagation of Shock Waves Through Channel Bends," *Computational Fluid Dynamics Journal*, Vol. 2, No. 1, 1993, pp. 1–36.

[129] Yousaf, M., "Motion of a Strong Shock Wave in a Medium of Nonuniform Density," *Phys Fluids*, Vol. 21, No. 2, 1978, pp. 217–220.

[130] Yousaf, M., "Effect of Overtaking Disturbances on the Motion of a Shock Wave due to an Intense Explosion," *Phys Fluids*, Vol. 25, No. 1, 1982, pp. 45–47.

[131] Yousaf, M., "Motion of a Strong Shock Wave in an Exponential Medium," *Phys Fluids*, Vol. 28, No. 6, 1985, pp. 1659–1664.

[132] Yousaf, M., "Strong Shocks in an Exponential Atmosphere," *Phys Fluids*, Vol. 30, No. 12, 1987, pp. 3669–3672.

[133] Yousaf, M., "Analysis of the Interaction Terms of The Motion of a Shock Wave due to an Intense Explosion," *Phys Fluids*, Vol. 31, No. 7, 1988, pp. 1922–1929.

[134] Liepmann, H. W. and Roshko, A., *Elements of Gasdynamics*, John Wiley & Sons, Inc., 1953.

[135] Zhang, F., Chue, R. S., Frost, D. L., Lee, J. H. S., Thibault, P., and Yee, C., "Effects of Area Change and Friction on Detonation Stability in Supersonic Ducts," *Proceedings: Mathematical and Physical Sciences*, Vol. 449, No. 1935, 1995, pp. 31–49.

[136] Wikipedia, "Manifold," http://en.wikipedia.org/wiki/Manifold, 2008.

[137] Hirsch, C., *Numerical Computation of Internal and External Flows*, Vol. 2, John Wiley & Sons, 1st ed., 1984.

[138] Lambert, W. D., "A Generalized Trigonometric Solution of the Cubic Equation," *The American Mathematical Monthly*, Vol. 13, No. 4, April 1906, pp. 73–76.

[139] Thompson, M., "A Note on the Calculation of Oblique Shock-Wave Characteristics," *Journal of Aeronautical Sciences*, November 1950.

[140] Emanuel, G., *Analytical Fluid Dynamics*, CRC Press, Boca Raton, FL, 2001.

[141] Anderson, J. D., *Modern Compressible Flow*, McGraw-Hill Companies, 3rd ed., 2002.

[142] Toro, E. F., *Riemann Solvers and Numerical Methods for Fluid Dynamics*, Springer-Verlag, 2nd ed., 1999.

[143] Sod, G. A., "A survey of several finite difference schemes for hyperbolic conservationlaws," *Journal of Computational Physics*, Vol. 27, 1978, pp. 1–31.

[144] Saito, T., Voinovich, P., Timofeev, E., and Takayama, K., "Development and Application of High-resolution Adaptive Numerical Techniques in Shock Wave Research Center," *Godunov Methods: Theory and Application*, edited by E. Toro, Kluwer Academic/Plenum Publishers, 2001, pp. 763–784.

Appendices

Appendix A

On-design Starting Characteristics of Two-Shock Inlets

A.1 Assumptions

Here, the concept of a quasi-steady starting condition is applied to the two-shock inlet. The air is modelled as an inviscid, calorically perfect gas. For theoretical purposes, here it is assumed that the inlet is to be started near its design condition. That is to say, the inlet is designed for Mach M_D, and that we are interested in its self-starting behaviour at $M_\infty = M_D$.

A.2 Starting

Consider the geometry of an unstarted two-shock inlet that is operating at a supersonic value of free-stream Mach number, M_∞, as shown in Figure A.1.

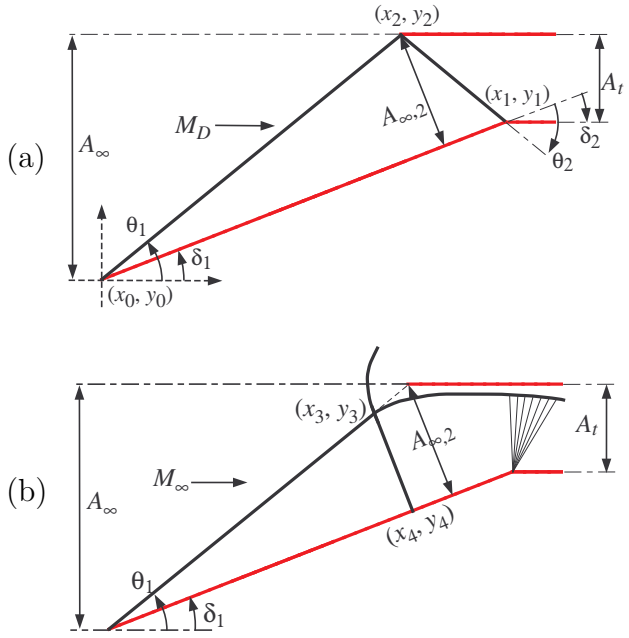

Figure A.1: Schematic of the inlet formed by using a two shock configuration. a) started operation at design conditions; b) unstarted operation near design conditions.

The flow undergoes compression from M_∞ to $M_{\infty,2}$ across an attached, oblique shock. In the *sub-critical* (unstarted) mode, a bow shock is situated some distance upstream of the cowl leading edge and provides a spillage mechanism. If the inlet is to start under quasi-steady flow condition, then the bow shock may be considered quasi-stationary in the sense that no transient accumulation of mass takes place between the shock system and the exit plane of the inlet. When the inlet is at the verge of starting (*critical mode*), the bow shock approaches the cowl lip where the capture area is $A_{\infty,2}$, as shown in Figure A.1. It is also known that in the unstarted mode, the throat must be choked (because maximum mass flux, $\dot{m}/A$, occurs at sonic conditions, *i.e.*, $M_t = 1$). Under these conditions, the geometry of

Figure A.1 must satisfy an equation of the general form:

$$0 = f_1(M_\infty, \delta_1, \phi, \gamma), \tag{A.1}$$

where,

$$\begin{aligned} f_1 = & \frac{A_t}{A_{\infty,2}} \left(\delta_1, \theta_1(M_\infty, \delta_1, \phi, \gamma), \theta_2(M_\infty, \delta_1, \phi, \gamma)\right) \\ & - \frac{A_{_K}}{A_{\infty,2}} \left(\gamma, M_{\infty,2}(M_\infty, \delta_1, \gamma)\right). \end{aligned} \tag{A.2}$$

The first term is a geometric constraint describing the area-ratio for the internal-expansion part in an unstarted two-shock inlet operating near its design Mach number, *i.e.*, $\lim_{M_\infty \to M_D} (A_t/A_{\infty,2})$:

$$\frac{A_t}{A_{\infty,2}} = \frac{\sin\theta_1 \sin\theta_2 - \sin(\pi - \theta_1 - \theta_2 + \delta_1)\sin\delta_1}{\sin\theta_2 \sin(\theta_1 - \delta_1)}. \tag{A.3}$$

This is a composite function, so that the θ_i terms are formal functions of (γ, M, δ, and ϕ), as discussed further below. The second term in (A.2) is the classical Kantrowitz function, which describes the sonic to local area ratio across a steady normal shock wave[62].

$$\frac{A_{_K}}{A_{(u)}} \left(\gamma, M_{(u)}\right) \equiv \frac{A_s}{A_{(d)}} \left(\gamma, M_{(d)}\right) \tag{A.4}$$

According to the Kantrowitz criterion, in the unstarted mode, the flow undergoes isentropic expansion beginning at state, (d), just aft of the shock wave and ending with choked flow at $A_s = A_t$, $M_t = 1$. For steady quasi-one-dimensional, isentropic flow, the general sonic-flow area is given by the well-known relation[104] pp. 6,

Eq. 80:

$$\frac{A_s}{A_j}(\gamma, M_j) = M_j \left[\frac{1 + \frac{\gamma-1}{2} M_j^2}{\frac{\gamma+1}{2}} \right]^{-\frac{1}{2}\frac{\gamma+1}{\gamma-1}} \tag{A.5}$$

The Mach number across the normal shock (used for obtaining the Kantrowitz function) is given by[104] pp. 7, Eq. 96:

$$M_{(d)} = \sqrt{\frac{(\gamma-1)M_{(u)}^2 + 2}{2\gamma M_{(u)}^2 - (\gamma-1)}} \tag{A.6}$$

The stream-tube area across the normal shock remains unchanged, so that:

$$A_{(d)} \equiv A_{(u)} \tag{A.7}$$

The Mach number downstream of the leading edge shock is obtained as $M_{\infty,2} = M_{(d)}(\gamma, M_\infty, \theta_1)$ using[104] pp. 9, Eq. 132:

$$M_{(d)} = f\left(\gamma, M_{(u)}, \theta\right) \tag{A.8}$$

$$= \sqrt{\frac{(\gamma+1)^2 M_{(u)}^2 \beta - 4(\beta-1)(\gamma\beta+1)}{[2\gamma\beta - (\gamma-1)][(\gamma-1)\beta+2]}}, \tag{A.9}$$

with square of the normal component of upstream Mach number given by:

$$\beta = M_{(u)}^2 \sin^2\theta. \tag{A.10}$$

As stated above, the aerodynamic angle for the leading-edge shock is obtained here by solving the classical oblique shock relation. It is well-known[104] that for an attached shock, in general, the solution may lie on one of two branches corre-

sponding to either the strong- or the weak-shock solution.

This aerodynamic shock angle can be obtained on either branch as a general solution to a cubic equation[104,138–141]. For completeness and consistency of notation, in the remainder of this chapter, it is used in the following explicit form:

$$\theta = \theta\left(\gamma, M, \delta, \phi\right) \tag{A.11}$$

$$= \arctan\left(\frac{b_1 + 2d\cos\left(\frac{\sigma+\phi}{3}\right)}{3b_2\tan\delta}\right), \tag{A.12}$$

where,

$$d = \sqrt{b_1^2 - 3b_2b_3\tan^2\delta_1}, \tag{A.13}$$

with,

$$\mathbf{b} = \left[\begin{array}{ccc} M^2 - 1 & 1 + \frac{\gamma-1}{2}M^2 & 1 + \frac{\gamma+1}{2}M^2 \end{array}\right]^T, \tag{A.14}$$

and,

$$\sigma = \arccos\left(\frac{b_1^3 - 9b_2\left(b_2 + \frac{\gamma+1}{4}M^4\right)\tan^2\delta}{d^3}\right). \tag{A.15}$$

Here, $\phi = 4\pi$ for weak-shock solution, and zero otherwise.

In the present disquisition, the leading edge shock always belongs to the weak family and is formally obtained as $\theta\left(\gamma, M_\infty, \delta_1, 4\pi\right)$. The reflected shock is obtained in an analogous manner, except that it may belong to either the strong- or the weak-shock branch.

In (A.2), $A_t/A_{\infty,2}$ is obtained after the geometry is constrained by the choice of any two of the three design parameters (M_D, δ_1, and θ_1), which are uniquely associated with a given two-shock inlet. Thus, quasi-steady starting behaviour of the inlet near design conditions can be determined in the $(M_\infty, A_t/A_\infty)$-plane and the effective free-stream capture area, $A_\infty = A_{\infty,1}$, at $M_\infty = M_D$ can be

determined using:

$$\frac{A_t}{A_\infty} = 1 - \frac{\sin(\pi - \theta_1 - \theta_2 + \delta_1)\sin\delta_1}{\sin\theta_1 \sin\theta_2}. \tag{A.16}$$

The above relation simultaneously satisfies solution to (A.2), so that for a given design value of free-stream Mach number, the δ_1-parameter is related to area contraction, and its selection completely specifies the geometry. *A plot of* (A.16) *in the area-Mach number domain, thus provides the Kantrowitz-like curve for an on-design, self-starting two-shock intake, as shown in Figure A.2.*

A.3 Multiple Solutions

As noted above, the second shock, as represented by the θ_2 parameter in (A.16), may belong to one of two families (corresponding either to weak or to strong reflected shock). Hence, depending on this choice, the self-starting condition is described either with the weak or with the strong reflected shock branch, *i.e.*, with ($\phi = 4\pi$) or with ($\phi = 0$), respectively, in (A.12).

Referring to Figure A.2, the new curves (for self-starting) lie below the original Kantrowitz function. The distance between these curves points out the degree to which the overboard spillage helps when compared with a fully enclosed duct. Indeed, a fully enclosed planar inlet can be constructed based on this geometry (using symmetry about the upper wall), and in the present idealized context, its starting characteristics would then match the original Kantrowitz curve. While the performance of the two inlets would be identical once the flow is started, their behaviour in the unstarted flow would be dramatically different.

The improved starting characteristics shown in Figure A.2 suggest that other geometries may also benefit to a similar degree. Hence, it is advantageous to

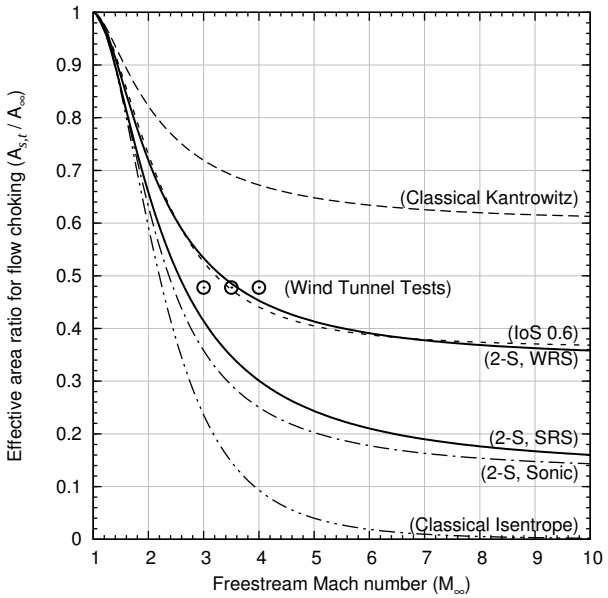

Figure A.2: Classical Kantrowitz curve applicable to fully enclosed internal compression inlets or Pitot-type intakes; Self-starting ability of two-shock inlets with weak reflected shock (WRS) and with strong reflected shock (SRS); Area-ratio of a two-shock inlet with sonic-design ($M_t = 1$); Maximum permissible area contraction under isentropic compression.

construct other stream traced geometries which provide external spillage in the unstarted mode, without sacrificing performance in the started mode. While the advantages of overboard spillage are clear from this analysis, there could be other factors present, such as flow stability and sensitivity to yaw and angle of attack, etc., which have not been considered here.

A.4 Unstarting

To determine the limit on supersonic operability of a two-shock inlet, we can substitute $M_3 = 1$ (downstream of the second oblique shock) in the foregoing relations. If this condition is used to constrain the geometry, then using the

relations listed in the previous section, one obtains a new curve for A_t/A_∞, as shown in Figure A.2. This curve is a lower limit on the permissible area ratio under highly idealized (on-design) conditions for stable, started operation (supersonic flow throughout). In practice, viscous effects would actually cause the inlet to unstart before this limit is reached; such effects are almost always of physical significance because disturbances originating at a downstream section of the boundary are able to propagate upstream through the subsonic flow in the boundary layer.

Comparing this limit to the isentrope, we note that for low values of free-stream Mach number (*viz.*, $M < 2$), the two curves lie close to one another. This result is attributable to the relatively small loss in total pressure across weak shock waves (low free-stream Mach number in combination with the obliqueness of the leading edge wave). However, a significant loss in stagnation pressure does still occur at higher free-stream Mach numbers (increased shock Mach number). Depending on application, this fact may render the SRS design point impractical (e.g., in the hypersonic flow regimes). In this respect, the two shock inlet shows limited potential for applications requiring very high contraction fixed geometry. Alternatively, for efficient high compression at hypersonic speeds, the straight compression ramp can be replaced with a suitable planar Prandtl-Meyer compression surface, as discussed in Appendix B.

Appendix B

On-design Starting Characteristics of Prandtl-Meyer Inlets

Consider the geometry of an unstarted P-M inlet that is operating at a supersonic value of free stream Mach number, M_∞, as shown in Figure B.1b. The flow undergoes isentropic compression from M_∞ to M_2. A bow shock is situated some distance upstream of the cowl leading edge. If the inlet is to start under pseudo-steady flow conditions, then the bow shock may be considered pseudo-stationary in the sense that no accumulation of mass takes place between the shock and the exit plane of the inlet. Under these conditions, when the inlet is at the verge of starting, the bow shock approaches the cowl lip where the capture area is represented by A_∞ as shown in Figure B.1b. It can be shown that in the unstarted mode, the throat is choked (recall that maximum mass flux, $\dot{m}/A$, occurs at sonic conditions, *i.e.,* $M_t = 1$).

Consider the flow geometry as shown in Figure B.1a. In the started mode,

when the inlet is operating at design conditions, it is evident that:

$$\frac{A_t}{A_{\infty,2}} = \frac{\sin(\theta - \delta)}{\sin\theta}, \tag{B.1}$$

where, θ and δ are design parameters uniquely associated with a given P-M inlet (*vide* Figure B.1a). Comparing the flow geometries between the started and the unstarted mode, we note that $A_{\infty,2}$ in the started mode is equal to A_∞ in the unstarted mode. For the latter case, if we assume that flow undergoes isentropic

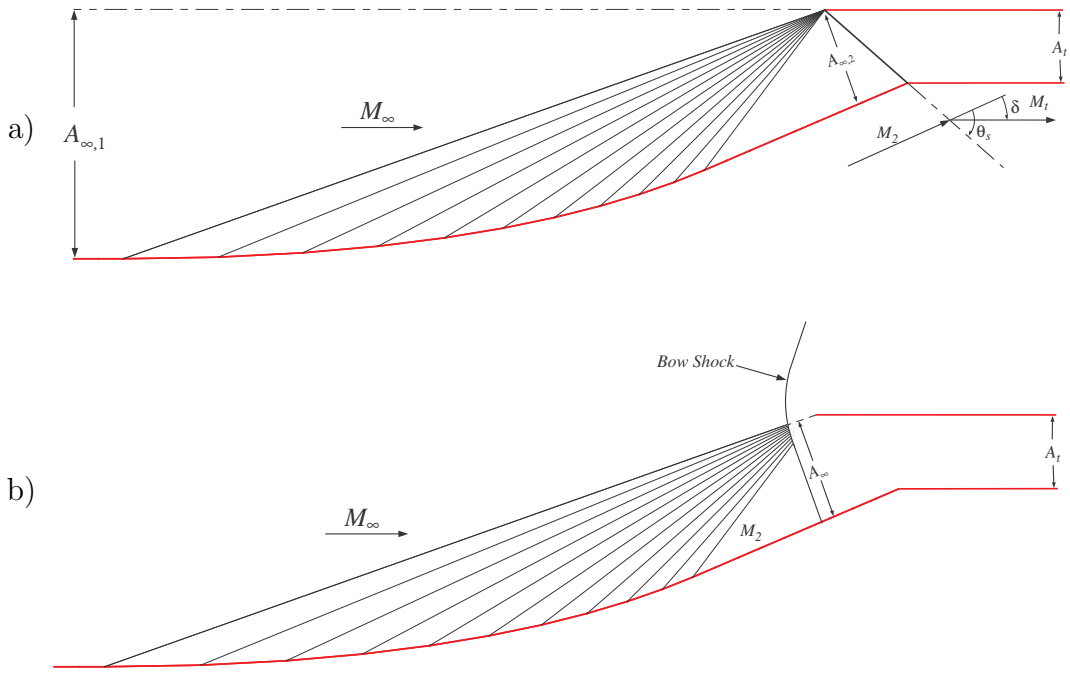

Figure B.1: Inlet formed by using a Prandtl-Meyer compression surface: a) started operation at design conditions, showing external compression followed by an oblique shock which turns the flow back parallel to free-stream direction; b) un-started operation at design conditions, showing external compression followed by a bow shock.

expansion aft of the bow shock (in Figure B.1b), then it may be shown that:

$$\frac{A_t}{A_\infty} = M_3 \left[\frac{1 + \frac{\gamma-1}{2} M_3^2}{1 + \frac{\gamma-1}{2}} \right]^{-\frac{1}{2}\frac{\gamma+1}{\gamma-1}}, \tag{B.2}$$

where the Mach number, M_3, just aft of the bow shock is given by:

$$M_3 = \sqrt{\frac{\frac{2}{\gamma-1} + M_2^2}{\frac{2}{\gamma-1}\gamma M_2^2 - 1}}. \tag{B.3}$$

Relating Eqs. (B.1) and (B.2), we obtain a relationship for startability of P-M inlets under design conditions.

$$\frac{\sin(\theta - \delta)}{\sin\theta} = M_3 \left[\frac{1 + \frac{\gamma-1}{2} M_3^2}{1 + \frac{\gamma-1}{2}} \right]^{-\frac{1}{2}\frac{\gamma+1}{\gamma-1}}. \tag{B.4}$$

The relationship between M_∞ and M_2 is strictly determined by geometry of Figure B.1, given the fact that the drawn compression waves are characteristics, locally inclined at Mach angles relative to the compression surface. Thus, their local inclination relative to the surface is given by:

$$\mu = \arcsin(1/M). \tag{B.5}$$

The net flow turning may also be determined using Prandtl-Meyer relation for isentropic compression between M_∞ and M_2:

$$\delta = \nu(M_\infty) - \nu(M_2), \tag{B.6}$$

where ν is the Pradtl-Meyer function given by:

$$\nu(M) = \phi(M) - \arctan\left(\beta(M)\right), \tag{B.7}$$

with,

$$\phi(M) = \sqrt{C_1}\arctan\left(\beta(M)\sqrt{C_2}\right), \tag{B.8}$$

where, $C_1 = \frac{\gamma+1}{\gamma-1}$, $C_2 = \frac{\gamma-1}{\gamma+1}$, and $\beta(M) = \sqrt{M^2-1}$.

Equation (B.6) may be substituted in (B.4) to render the latter in the form: $f(\gamma, M_\infty, M_2, \theta) = 0$. Isolating for θ in this function, one gets $\theta = f(\gamma, M_\infty, M_2)$, and with $M_3 = f(\gamma, M_2)$ as defined by (B.3):

$$\theta = \arctan\left[\frac{1}{\cot(\nu(M_\infty) - \nu(M_2)) - \frac{M_3}{\sin(\nu(M_\infty)-\nu(M_2))}\left[\frac{1+\frac{\gamma-1}{2}M_3^2}{1+\frac{\gamma-1}{2}}\right]^{-\frac{1}{2}\frac{\gamma+1}{\gamma-1}}}\right], \tag{B.9}$$

For a given ratio of specific heats, γ, this is an equation in two independent variables, so that an additional relation for the aerodynamic shock angle, θ, must be written simultaneously. For a given value of M_2, the aerodynamic shock angle and flow deflection are related by:

$$0 = -M_2^{-2} + \sin^2\theta - \frac{\gamma+1}{2}\frac{\tan\theta}{\tan\theta + \cot\left[\nu(M_\infty) - \nu(M_2)\right]} \tag{B.10}$$

Substituting from (B.9) for θ in (B.10), the latter can be now be solved, for $M_2 = f(\gamma, M_\infty)$, to give a unique inlet that is defined by $\{\gamma, M_\infty, M_2\}$. The resulting inlets give a curve in the Area ratio and free stream Mach number domain as plotted in Figure B.2. This curve describes the startability of Pradtl-Meyer inlets under pseudo-steady flow conditions. This is applicable when the

inlet is to be started by accelerating it slowly from a subsonic value of free stream Mach number, M_∞, to its design Mach number, M_D. As with the geometry of any oblique shock intake (166), there are two separate design curves: one for weak shock solution and the other for strong shock solution. In this regard comments made in Appendix A on Page 166 are equally applicable here as well.

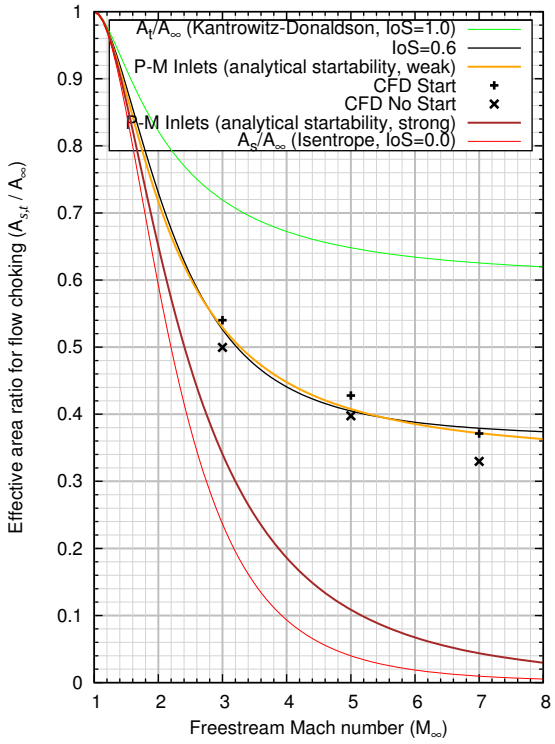

Figure B.2: Startability of P-M inlets compared to the classical Kantrowitz curve for fully internal compression inlets. Curve for maximum compression with isentropic operability is also plotted (dashed line). It is noted that the startability of P-M inlets closely follows the curve for IoS = 0.6. startability is also plotted (dashed line). It is noted that the startability of P-M inlets closely follows the curve for IoS = 0.6.

Appendix C

Quasi-one-dimensional Index of Startability (IoS)

The index of startability is a measure of the difficulty or the ease with which an inlet is expected to start—especially, when compared to a fully enclosed version of the same inlet, without any perforations or overboard spillage, and under fully idealized, quasi-steady free-stream flow conditions. The index of startability is defined as follows[65]:

$$\text{IoS} = \frac{A_t/A_\infty - A_s/A_\infty}{A_{_K}/A_\infty - A_s/A_\infty}. \tag{C.1}$$

Here, A_t/A_∞ is the net area ratio of a designed inlet; A_s/A_∞ is the sonic area corresponding to isentropic compression from (M_∞ and A_∞) to ($M_s = 1$, and A_t); $A_{_K}/A_\infty$ is the area ratio corresponding to a fully enclosed inlet operating at M_∞ that is just about to start (Kantrowitz condition).

For practical inlets, the above function lies in the range [0:1], and its value simply indicates a design condition in the area-Mach number plane. For example, a positive value near zero indicates that under started mode, the inlet is designed

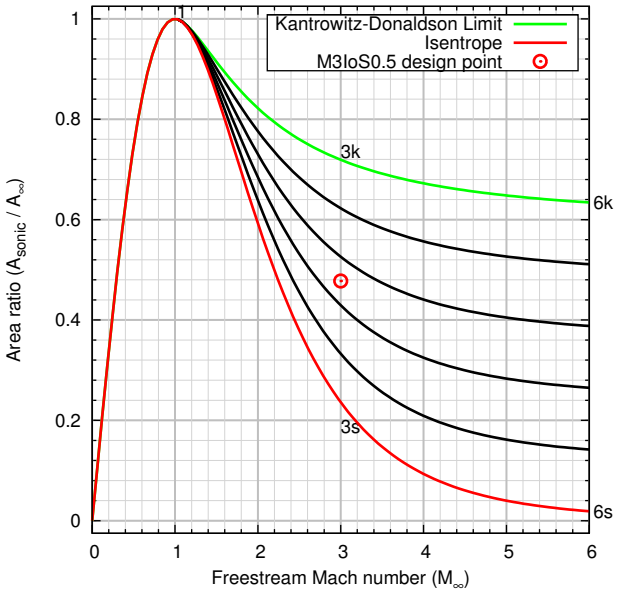

Figure C.1: Classical Kantrowitz-Donaldson function (curve 1-3k-6k, IoS = 1) applicable to fully enclosed internal compression inlets. Maximum permissible area contraction under isentropic compression (curve 1-3s-6s, IoS = 0). Intermediate curves in black are drawn for IoS = $[0.8, 0.6, 0.4, 0.2]$.

to operate near the isentropic curve of Figure C.1. An IoS value of unity recovers the Kantrowitz function; above this value an inlet will typically self-start. A negative value of IoS signifies inoperability (or an unstarted flow) under steady state operation (even with isentropic compression efficiency). Strictly speaking, the above description is applicable only to inlets containing quasi-one-dimensional flow. *Nevertheless, according to the above definition, the wind-tunnel model described in Chapter 2 is described by the "M3IoS0.5" design point.*

The actual self-starting ability of two-shock inlets differs from the above function. In fact it is described by IoS values significantly less than unity. Similarly, on-design operation at a given free-stream Mach numbers is possible only in a significantly narrower band of IoS values. The supersonic operability of a two-shock

design is described by IoS values significantly above zero. These two points are elaborated in greater detail in Chapter 2.

Appendix D

Experimental Data

The 2S-WRS M3IoS0.5 wind-tunnel model contained 43 pressure taps; 15 of these were staggered along the main ramp, at one inch spacing, while four taps were placed in the upper wall, as shown in Figure D.1. A fan-like distribution of taps (3×4) was drilled in each side-wall (tap needles are visible in Figure 2.16). The pressure data was collected using a scanning transducer module (model: ESP-32, s/n: 32821, calibrated with a worst case accuracy of ±0.15 %FS over a range of ±5 psi).

Figure D.2 shows the pressure traces (in time) during the back door open-close-open cycle for the M3 test condition. It is evident that the upon completion of the door-cycle, the flow reverts to the original configuration (unstarted); although some temporal variation exists, the flow is generally stable.

Figure D.3 and Figure D.4 show the same process for the M3.5 and M4 cases, respectively. It is evident that the upon completion of the door-cycle, the flow reverts to the original configuration (started); in each case, the resulting flow is generally very stable.

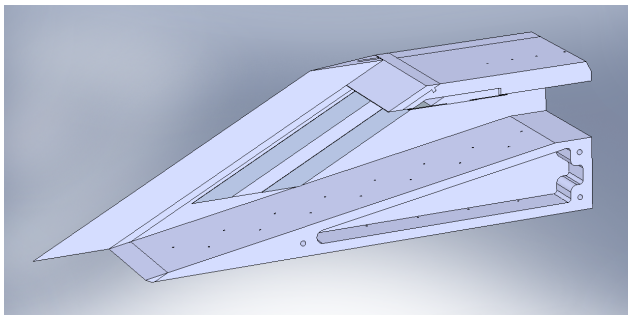

Figure D.1: Sectioned view of the CAD model. The pressure tap holes are enlarged to enhance the view (actual diameter of the drilled holes was 0.020 inches).

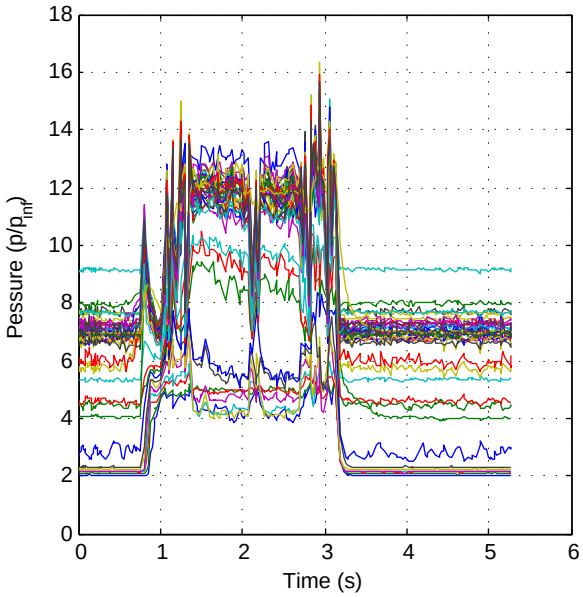

Figure D.2: Pressure traces for various tap location for the M3 test condition (R10330). The same data was used to render Figure 2.18, which is arguably much easier to grasp.

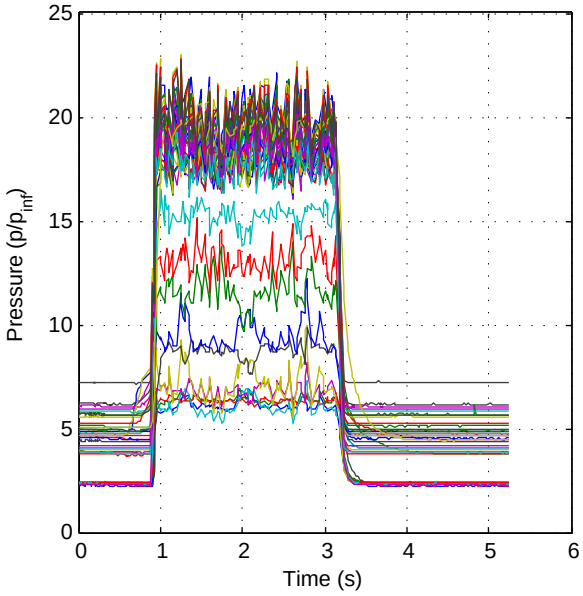

Figure D.3: Pressure traces for various tap location for the M3.5 test condition (R10329). The same data was used to render Figure 2.19, which is arguably much easier to grasp.

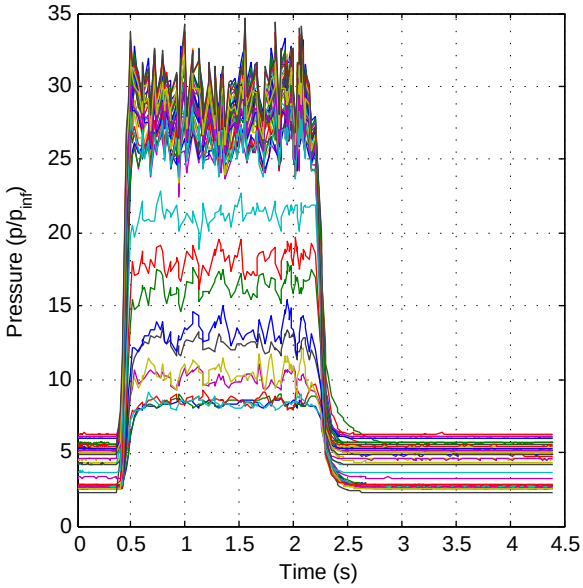

Figure D.4: Pressure traces for various tap location for the M4 test condition (R10344). The same data was used to render Figure 2.20, which is arguably much easier to grasp.

Appendix E

CFD Software Package

Several different numerical kernels are present in the software package; the kernel which was used here (`UnsteadyEuler` option) is accurate to second order in both spatial and temporal discretization. It is based on a finite volume approach using the MUSCL Hancock[142] scheme for solution-adaptive unstructured meshes, and is suitable for computation of highly unsteady gas dynamic flows involving localized flow features[102]. An approximate Riemann solver (`PDSRiemann=2` option) was used. The software routinely undergoes extensive benchmarking and regression testing by the author, against both experimental data and the classical solutions available in CFD literature[77,137,143,144].

Appendix F

Influence Coefficients for Body Force

Following §I.6, under the quasi-one-dimensional, quasi-steady flow assumptions, the conservation laws for a system of mass subjected to a constant acceleration or mass specific force, f, and area variation, $\mathrm{d}A/\mathrm{d}x$, can be written as:

$$\frac{\mathrm{d}\rho}{\rho} + \frac{\mathrm{d}u}{u} + \frac{\mathrm{d}A}{A} = 0 \tag{F.1}$$

$$\mathrm{d}p + \rho u \mathrm{d}u = \rho f \mathrm{d}x \tag{F.2}$$

$$\mathrm{d}h + \frac{1}{2}\mathrm{d}u^2 = f \mathrm{d}x \tag{F.3}$$

Following the approach of Shapiro[68], the influence of acceleration source terms on various flow parameters can be obtained as listed below. Note that the coefficients to the "independent variable" dA/A must turn out to be identical to those listed in the first column of[68] Table 8.1, pp. 228. Similarly, the extra terms which appear below should be seen as the "influence coefficients" for the case $f \neq 0$, with $\hat{a}dx/L$ as the "independent variable"; listed together, these coefficients may

be considered as an additional column to be appended to Shapiro's table.

$$\frac{\mathrm{d}T}{T} = \left[-\hat{a}\frac{T_\infty}{T}\frac{\gamma-1}{\gamma}\frac{1}{M^2-1}\right]\frac{\mathrm{d}x}{L} - \left[(\gamma-1)\frac{M^2}{M^2-1}\right]\frac{\mathrm{d}A}{A} \tag{F.4}$$

$$\frac{\mathrm{d}u}{u} = \left[\hat{a}\frac{T_\infty}{T}\frac{1}{\gamma}\frac{1}{M^2-1}\right]\frac{\mathrm{d}x}{L} + \left[\frac{1}{M^2-1}\right]\frac{\mathrm{d}A}{A} \tag{F.5}$$

$$\frac{\mathrm{d}M}{M} = \left[\frac{\hat{a}}{2}\frac{T_\infty}{T}\frac{\gamma+1}{\gamma}\frac{1}{M^2-1}\right]\frac{\mathrm{d}x}{L} + \left[\frac{\frac{1}{2}(\gamma-1)M^2+1}{M^2-1}\right]\frac{\mathrm{d}A}{A} \tag{F.6}$$

$$\frac{\mathrm{d}c}{c} = \left[-\frac{\hat{a}}{2}\frac{T_\infty}{T}\frac{\gamma-1}{\gamma}\frac{1}{M^2-1}\right]\frac{\mathrm{d}x}{L} - \left[\frac{\gamma-1}{2}\frac{M^2}{M^2-1}\right]\frac{\mathrm{d}A}{A} \tag{F.7}$$

$$\frac{\mathrm{d}\rho}{\rho} = \left[-\hat{a}\frac{T_\infty}{T}\frac{1}{\gamma}\frac{1}{M^2-1}\right]\frac{\mathrm{d}x}{L} - \left[\frac{M^2}{M^2-1}\right]\frac{\mathrm{d}A}{A} \tag{F.8}$$

$$\frac{\mathrm{d}p}{p} = \left[-\hat{a}\frac{T_\infty}{T}\frac{1}{M^2-1}\right]\frac{\mathrm{d}x}{L} - \left[\gamma\frac{M^2}{M^2-1}\right]\frac{\mathrm{d}A}{A} \tag{F.9}$$

where, $\hat{a} = fL/c_\infty^2$ is the non-dimensional acceleration, T is local static temperature, c is the local speed of sound, ρ is the local mass density, p is the local static pressure, L is the length of the channel, and M is the local flow Mach number.

The above equations can be integrated starting with prescribed conditions $(\rho(x_0), u(x_0), p(x_0),\ etc.)$ at the entrance plane (x_0) of a specified channel (given dA/dx, L, *etc.*). However, in the context of intake flows, the approach flow conditions are customarily designated by the ∞ subscript, as reflected in the above notation. The result of the integration is the steady state spatial profile/distribution of the above parameters $(\rho(x), u(x), p(x),\ etc.$ for $0 < x < L)$. This result can be used as a check against the numerical implementation of body force term in the numerical (CFD) codes.

Figures F.1 and F.2 show comparison between Asterix simulation and the integrated result from the above equations. The first test (Figure F.1) is for

subsonic inflow in a constant area channel with $\hat{a} = -0.1$. This is a rather sensitive test because the CFD simulation must include proper subsonic outflow boundary treatment; this is done using the standard pressure boundary condition in Asterix, and as can be seen, excellent agreement is present with the exact solution. The second test (Figure F.2) is for a planar constant slope channel with area ratio of 10, inflow Mach number of -3, and $\hat{a} = -5$. Again, excellent agreement between the CFD simulation and the integration of the above exact steady state relations is evident.

The negative signs accompanying the acceleration, flow velocity and the Mach number deserve a brief note. The physical situation above corresponds to a body accelerating rightward, along the conventionally positive x-direction. In the equations describing the flow however, the negative f term denotes acceleration of a leftward flow originating on the right; the sign is consistent with the flow going in a direction opposite to the usual definition for a positive x-axis. Barring signs, the situation is in every other respect identical to the rightward flow originating on the left, and aligned with the positive x-axis.

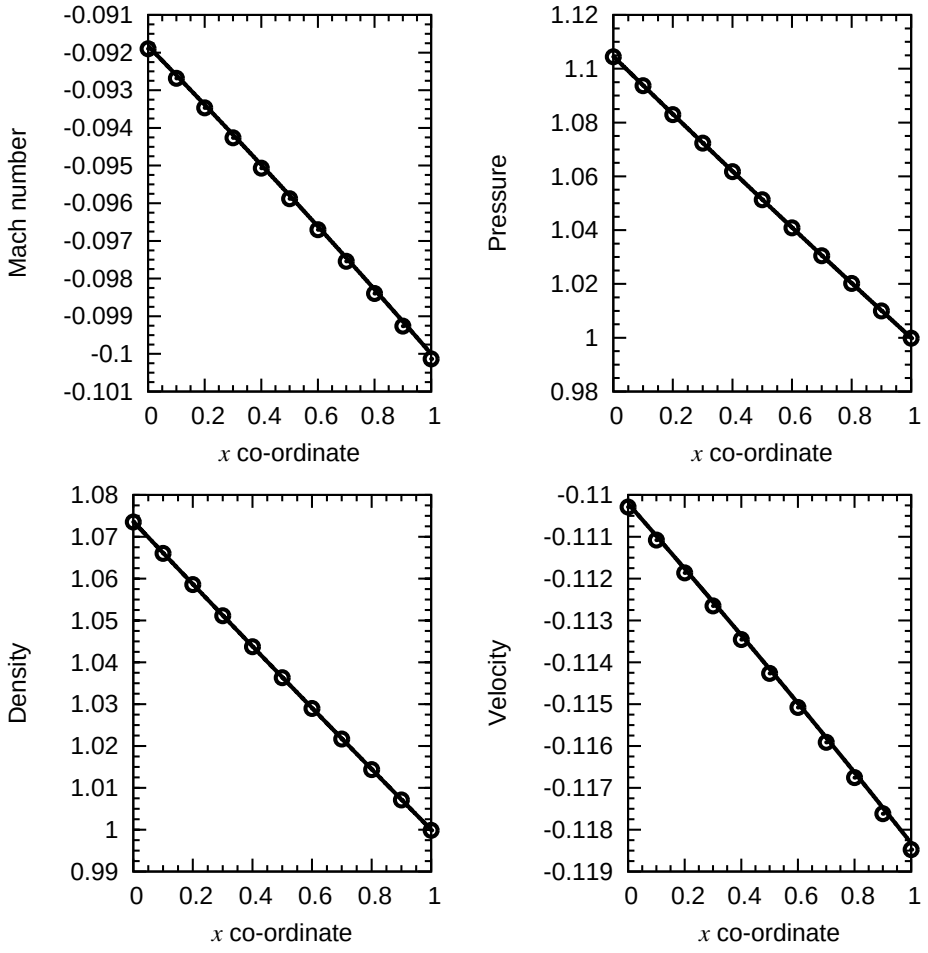

Figure F.1: Comparison between theory (solid line) and Asterix (CFD, circles). $A_l = A_r = 1$, $\hat{a} = -0.1$, subsonic inflow, exit/back pressure: $p_b = 1.10451$, channel length $L = 1$.

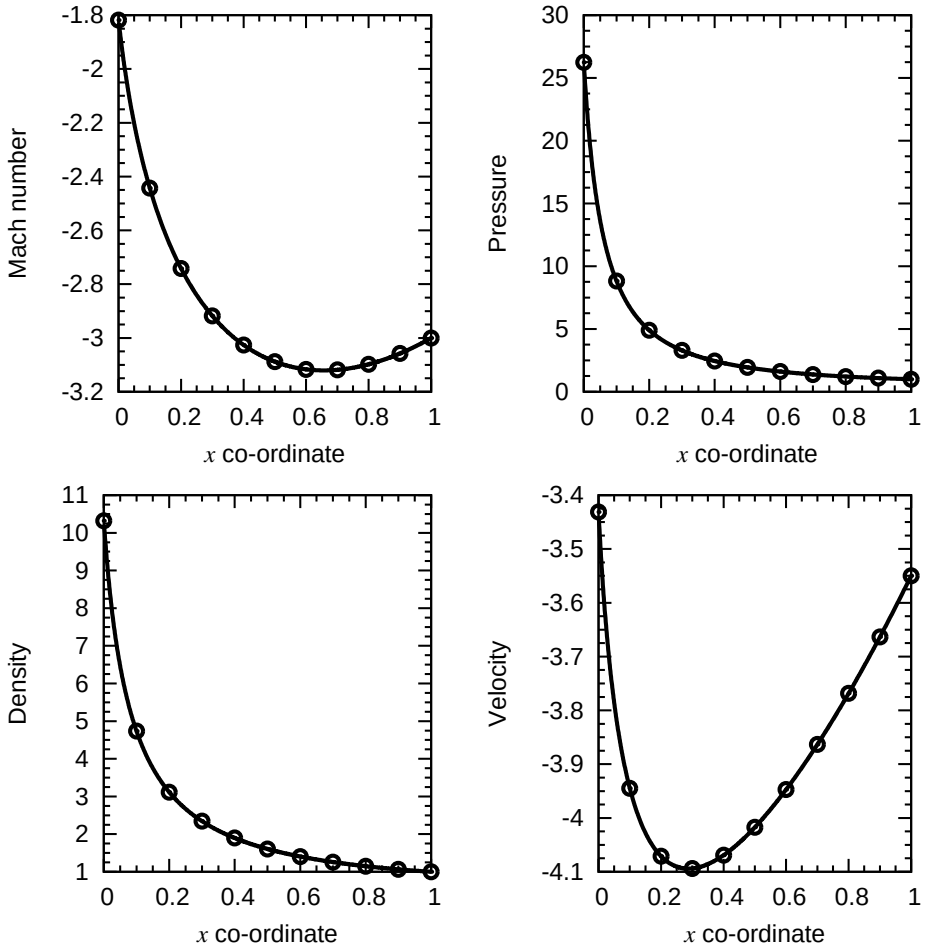

Figure F.2: Comparison between theory (solid line) and Asterix (CFD, circles). $A_l = 0.1$, $A_r = 1$, $\hat{a} = -5$, supersonic inflow $M_\infty = -3$, channel length $L = 1$.

Appendix G

Lifting Isentrope Tests

Here the *lifting isentrope* model (§5.3.1 on Page 90) is evaluated by direct comparison with Asterix. Several cases are reported; in each case, the flow is from the right, and the solution is compared after accelerating ($\hat{a} = \{0.1, 1.0, 10.0\}$), from an initial to a final value of free stream Mach number ($m_\infty = 3 \rightarrow 4$ or $m_\infty = 3 \rightarrow 6$). The circles are the correct solution (from Asterix) and the solid lines are the result of lifting isentrope model. The observations and interpretations are as follows:

- at the entrance plane of the duct $x = L$, the solution is known and hence it must match the exact value;
- for constant area section, $A_x = 0$ the exact solution is trivial (simple, homentropic, uniform flow in an accelerated duct);
- for non-uniform area, the error accumulates near $x = 0$ at the back, but it is typically very small;
- the error as $x \rightarrow 0$ is greater for larger values of $\hat{a}$, and may be considered

negligible for low values of $\hat{a}$, as expected;

- the error is greater for $m_\infty = 3 \to 4$ cases as compared to $m_\infty = 3 \to 6$;
- among the tests shown/conducted, the error is the greatest ($\approx 15\%$) for the $m_\infty = 1.5 \to 2$ case and it is reduced dramatically with time, so that in the $m_\infty = 1.5 \to 3$ case there is minimal error.
- the interpretation of these results is that for larger free stream Mach numbers, the flow disturbances take a shorter duration to subside (flow adjusts quickly) making the approximation better;
- it is found that the model is sufficiently accurate for use in intake shock dynamics.

The variational change in spatial distribution of flow parameters according to the lifting isentrope can be found using the formulae given under §I.7, along with $\partial_t(m_\infty) = f/c_\infty$. For instance, for density we have:

$$\begin{aligned} \frac{\delta}{\delta t}\rho &= \frac{\delta}{\delta t}\left(\rho_\infty \left(\frac{1+\frac{\gamma-1}{2}m_\infty^2}{1+\frac{\gamma-1}{2}m^2}\right)^{\frac{1}{\gamma-1}}\right) \\ &= \frac{\rho f}{c_\infty}\left(\frac{m_\infty}{1+\frac{\gamma-1}{2}m_\infty^2}\right)\left(1-\frac{m^2(m_\infty^2-1)}{m_\infty^2(m^2-1)}\right) \end{aligned} \tag{G.1}$$

For large m_∞ the term in first parentheses scales like $1/m_\infty$ which may explain the better accuracy for larger m_∞. Similarly, the last term gives zero for $m = m_\infty$, *i.e.*, the above function gives zero variation in the free stream where $\rho = \rho_\infty = const$, as expected. Far downstream, where m is different from m_∞ the variation is the largest.

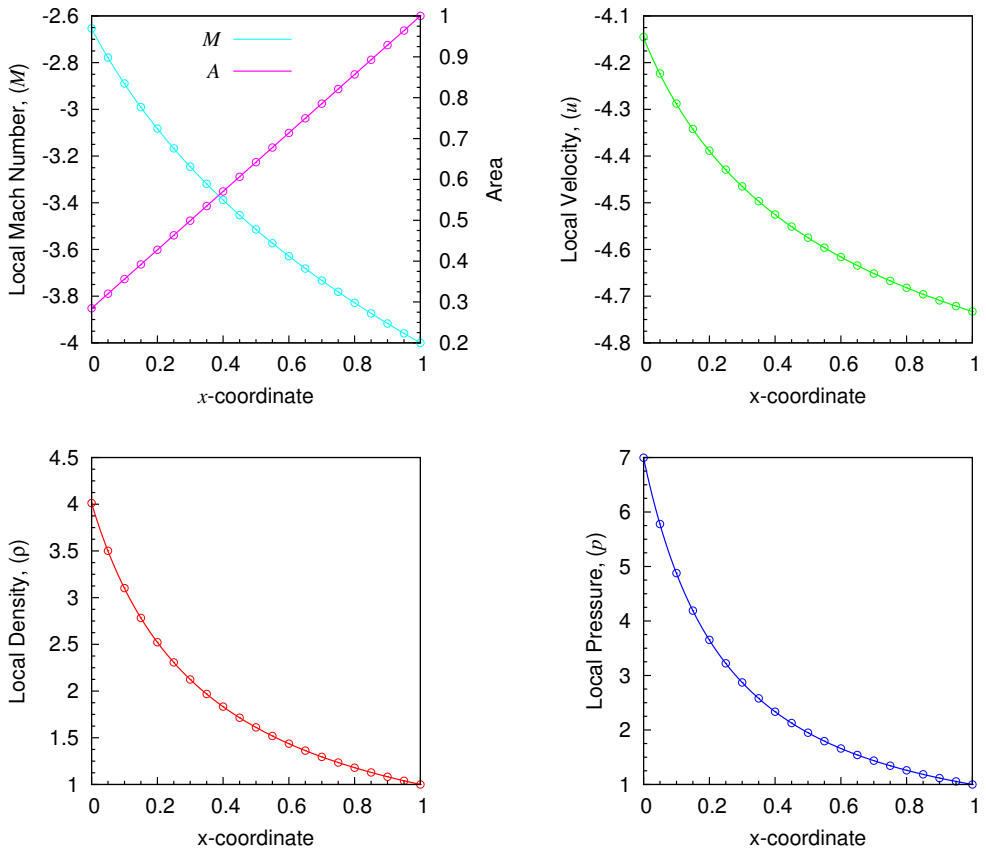

Figure G.1: Comparison between lifting isentrope (approximate) with Asterix (accurate). $\hat{a} = -0.1$, $m_\infty = -(3 \to 4)$.

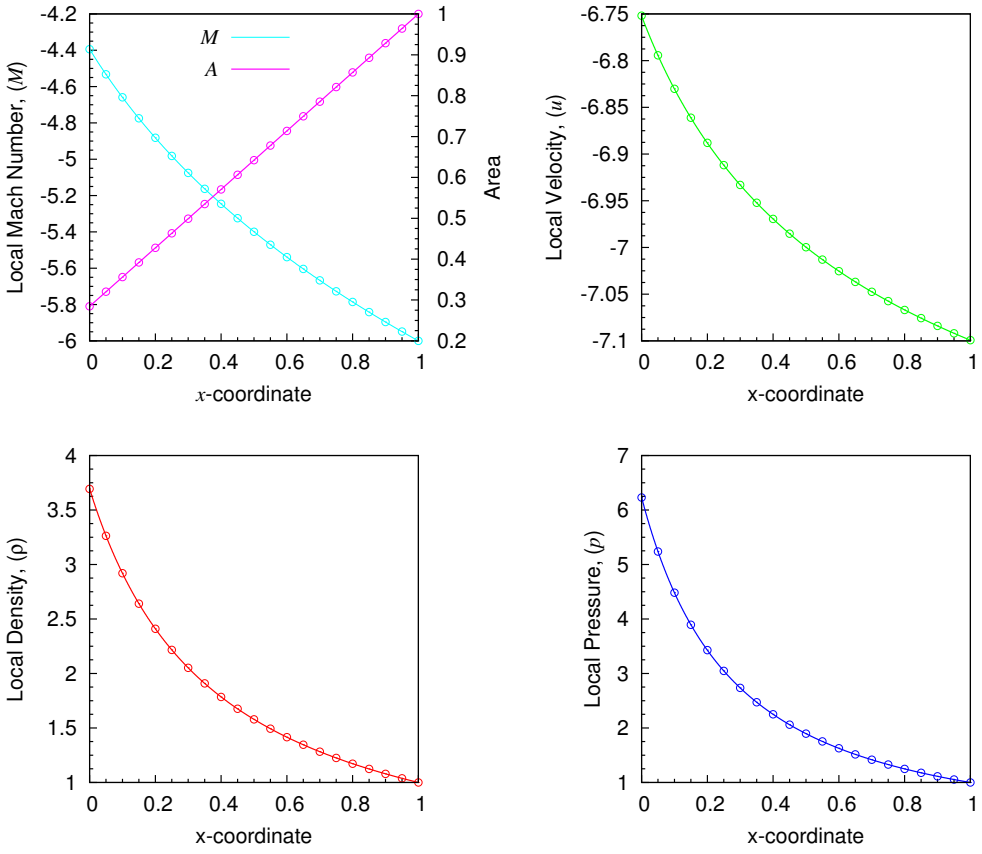

Figure G.2: Comparison between lifting isentrope (approximate) with Asterix (accurate). $\hat{a} = -0.1$, $m_\infty = -(3 \to 6)$.

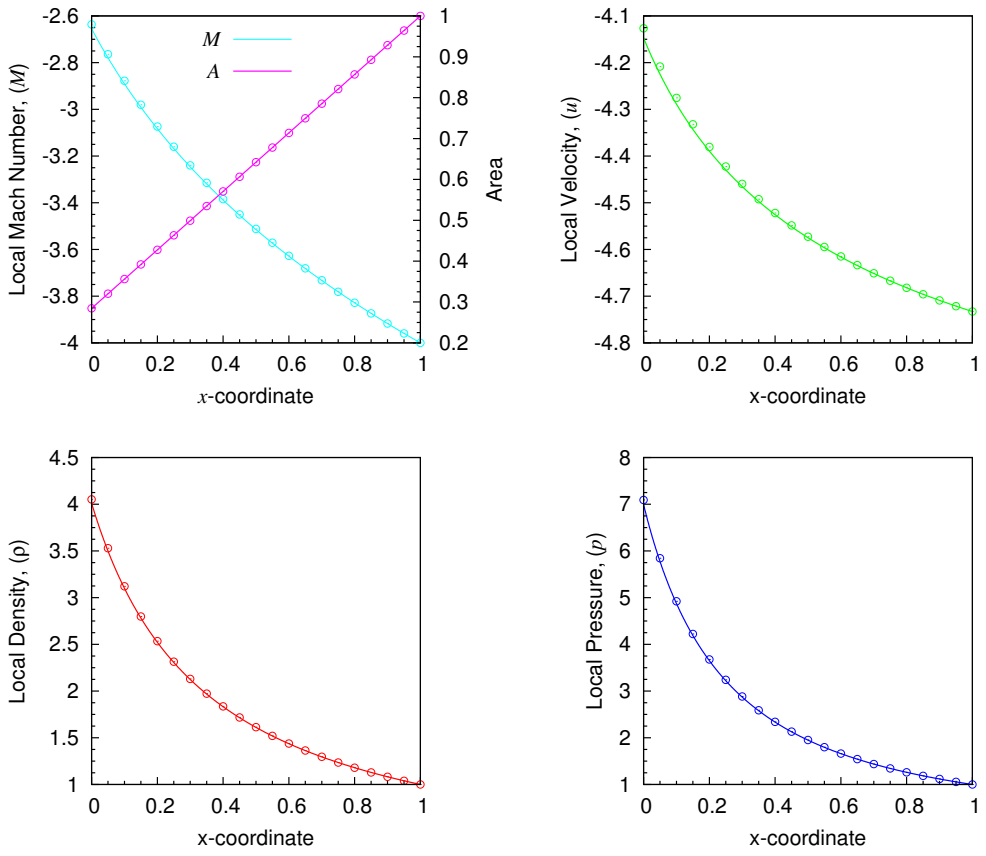

Figure G.3: Comparison between lifting isentrope (approximate) with Asterix (accurate). $\hat{a} = -1.0$, $m_\infty = -(3 \to 4)$.

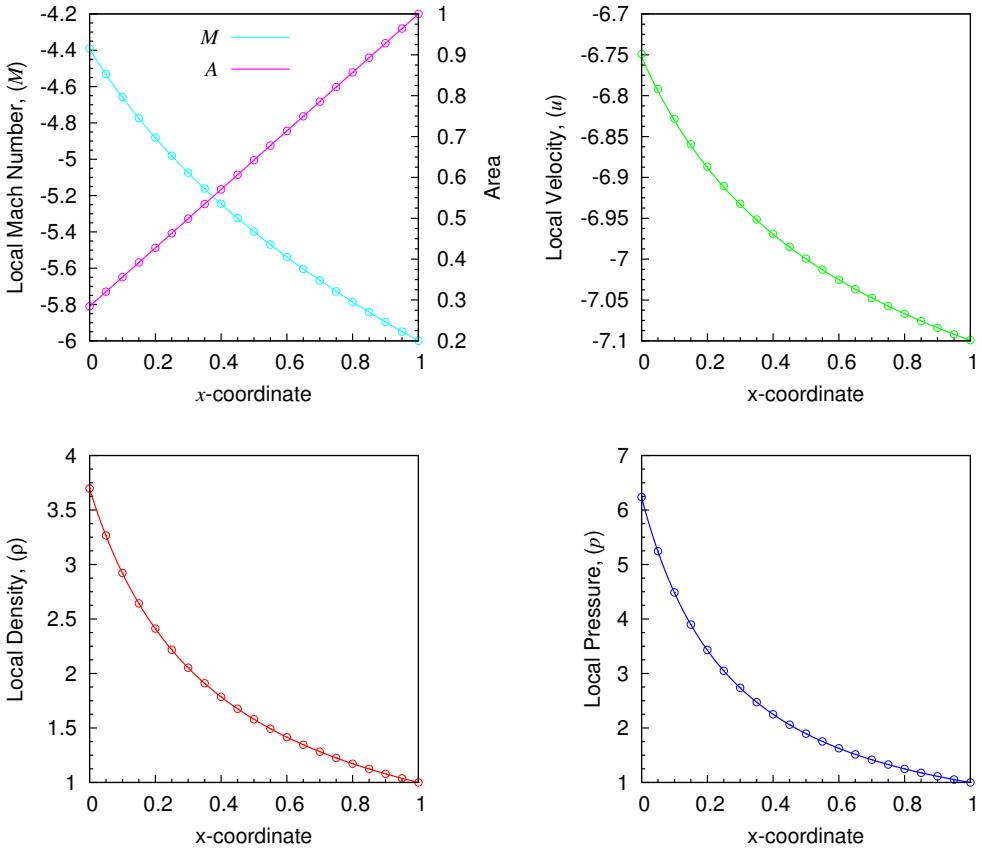

Figure G.4: Comparison between lifting isentrope (approximate) with Asterix (accurate). $\hat{a} = -1.0$, $m_\infty = -(3 \to 6)$.

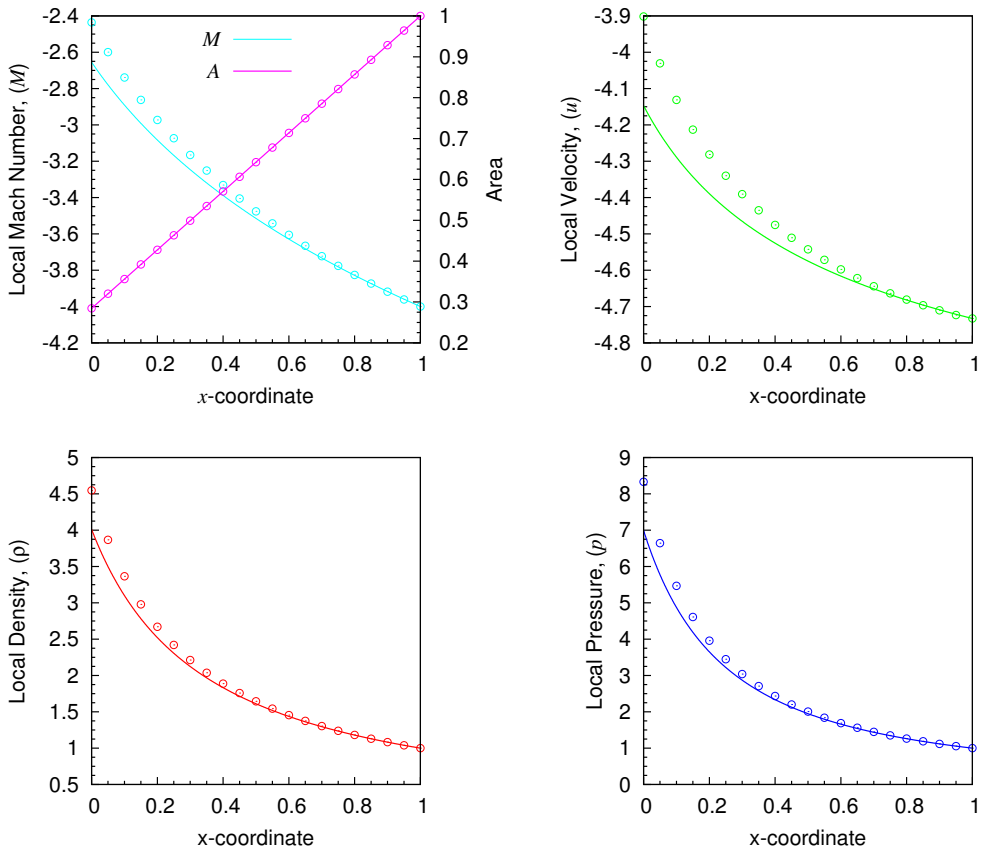

Figure G.5: Comparison between lifting isentrope (approximate) with Asterix (accurate). $\hat{a} = -10.0$, $m_\infty = -(3 \to 4)$.

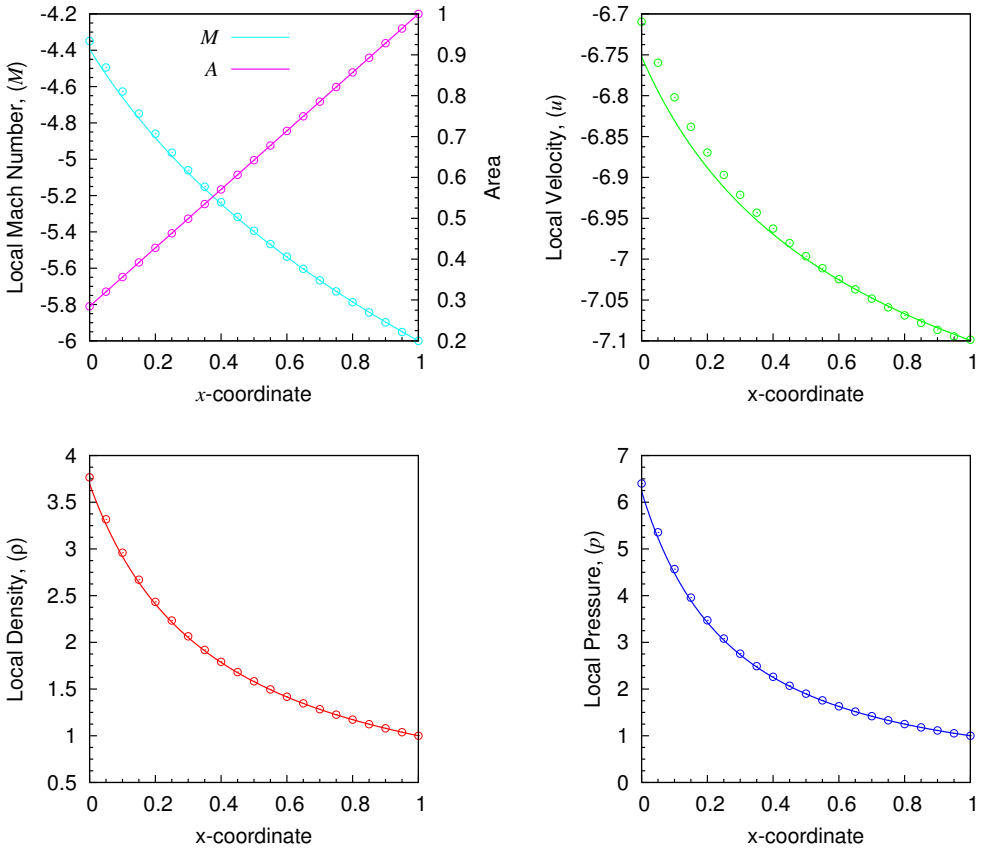

Figure G.6: Comparison between lifting isentrope (approximate) with Asterix (accurate). $\hat{a} = -10.0$, $m_\infty = -(3 \to 6)$.

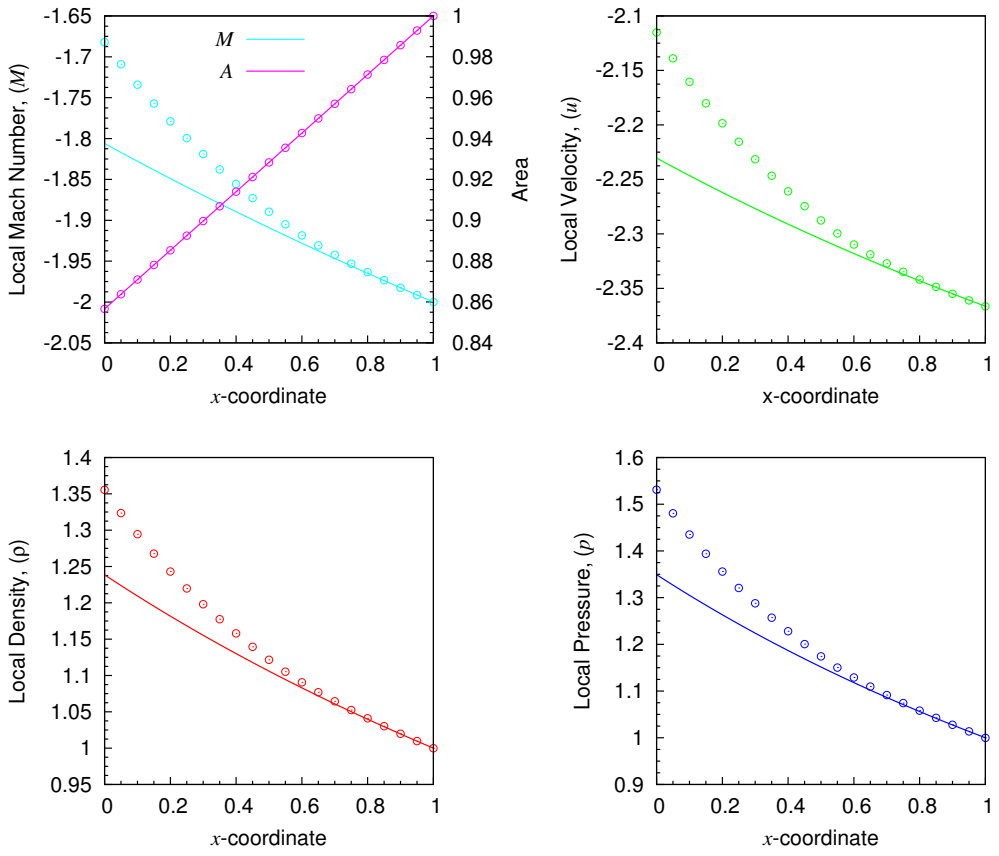

Figure G.7: Comparison between lifting isentrope (approximate) with Asterix (accurate). $\hat{a} = -1.0$, $m_\infty = -(1.5 \to 2)$.

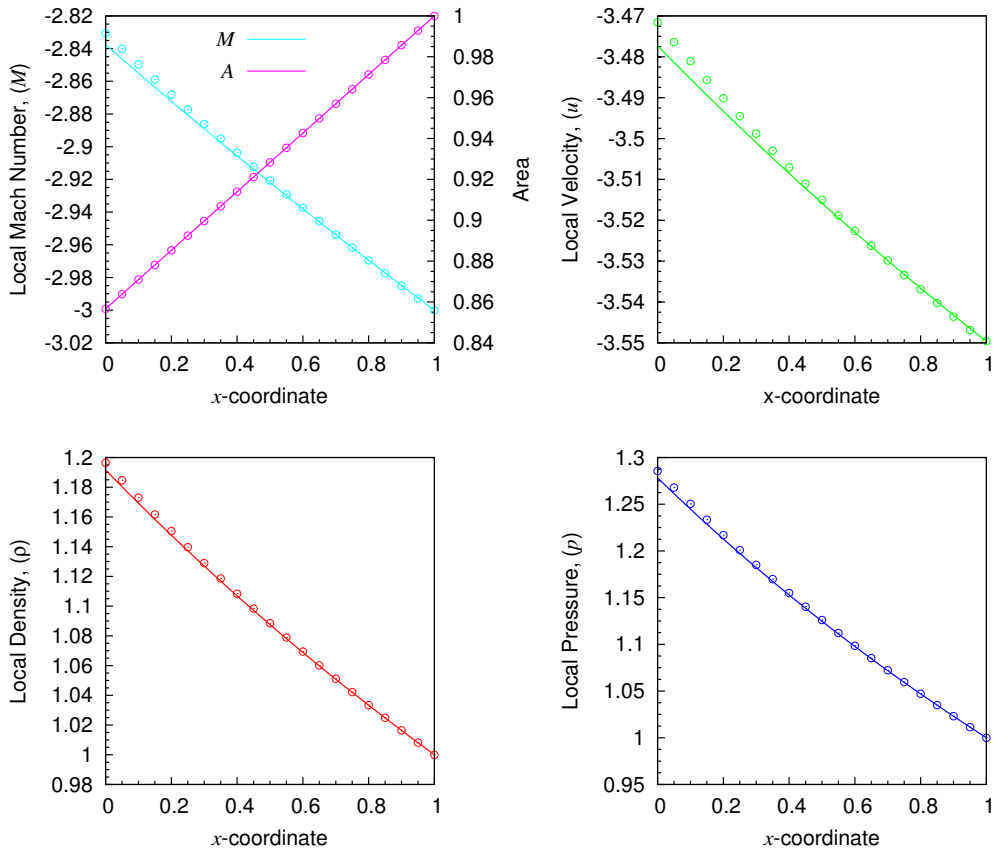

Figure G.8: Comparison between lifting isentrope (approximate) with Asterix (accurate). $\hat{a} = -1.0$, $m_\infty = -(1.5 \to 3)$.

Appendix H

Empirical Modifications to CCW$^+$

This appendix contains some of the cases reported in Chapter 7, where it has been found that CCW$^+$ may be modified in some simple way to allow better agreement with the more accurate solution of the full Euler equations solved using Asterix[1]. These approximations are unjustified in general, and no explanation has been found for the improved accuracy. These results are reported here for future reference, and are presented in the spirit of an approximate model modified by empirical observation. The reader should refer to §7.5 for more details on each figure.

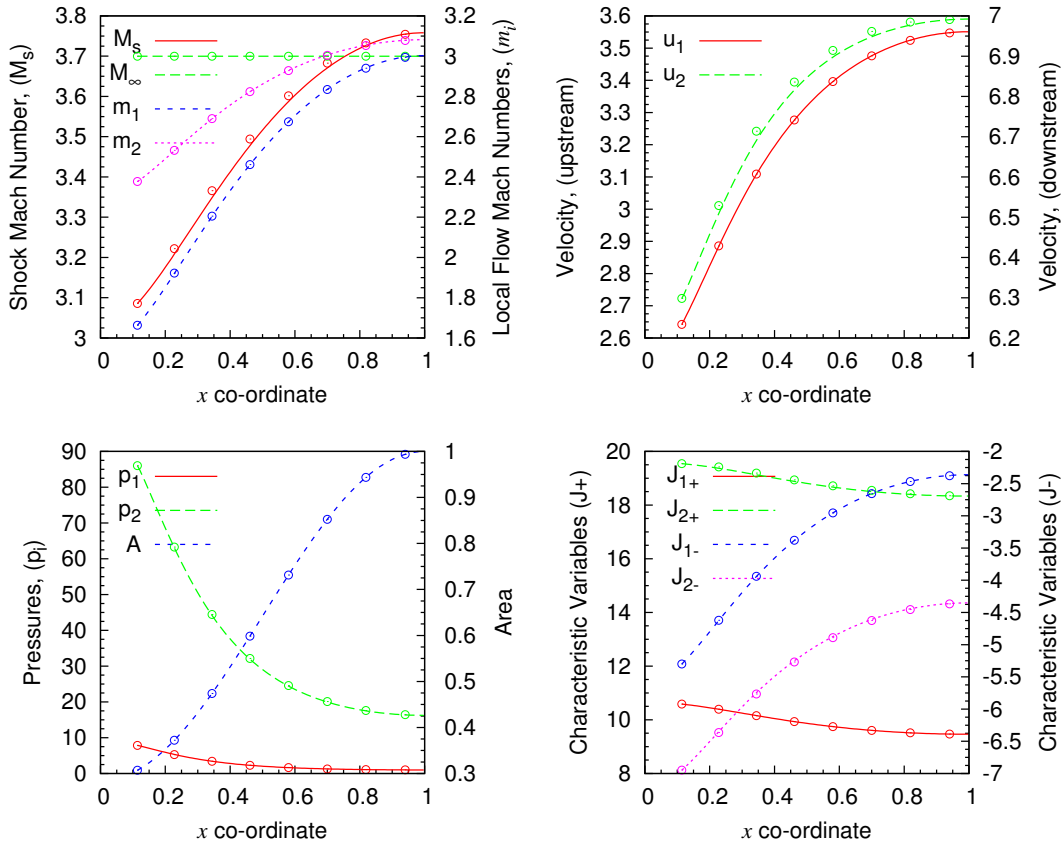

Figure H.1: Case II: a left moving diverging channel encounters a right facing shock wave, $M_s \simeq 3$; comparison between modified CCW$^+$ (solid) and CFD (circles); non-uniform, non-quiescent gas ahead of shock, no body force present ($f = 0$); m_∞ refers to $m(x = L) = const$; Smooth geometry model: M_D3, $IoS = 0.1$. The agreement is considered excellent.

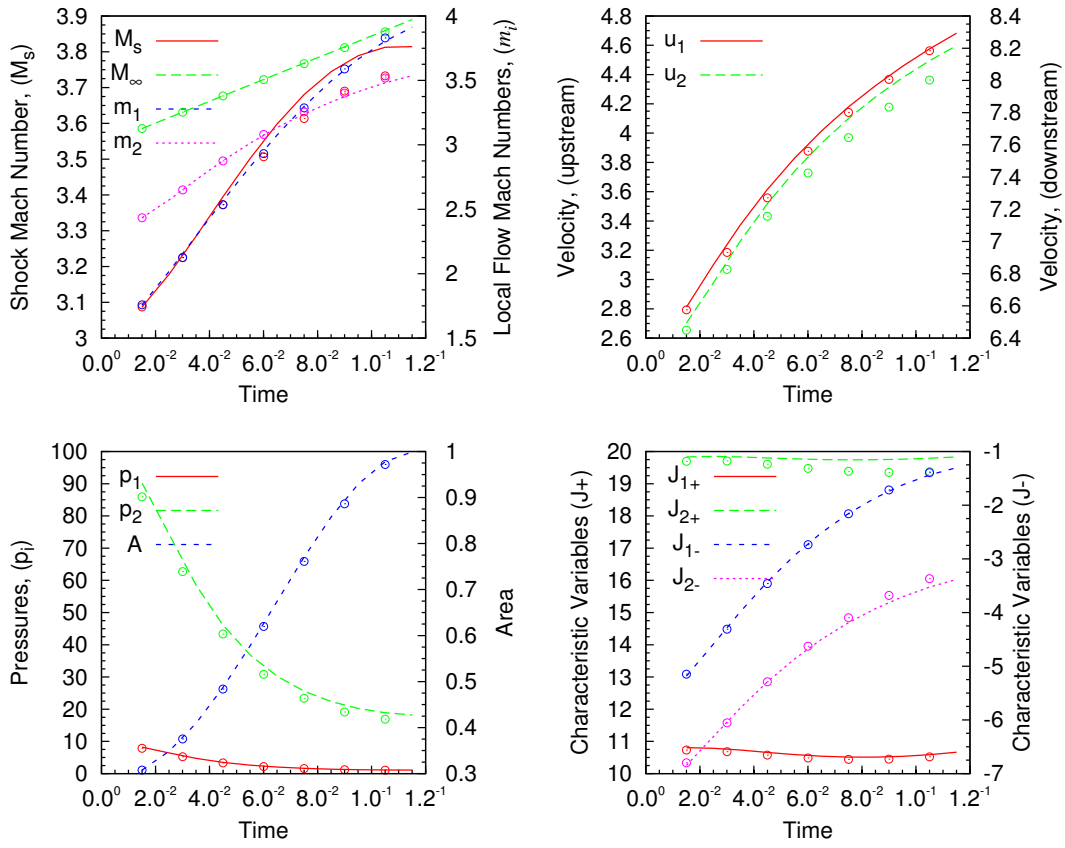

Figure H.2: Case II: a left moving diverging channel encounters a right facing shock wave, $M_s \simeq 3$; comparison between modified CCW$^+$ (solid) and CFD (circles); non-uniform, non-quiescent gas ahead of shock, non-zero body force present ($f = 10$); m_∞ refers to $m(x = L) = const$; Smooth geometry model: M_D3, $IoS = 0.1$. The agreement is considered good; the key discrepancy appears in J_{2^-} and J_{2^+} in the lower-right subplot.

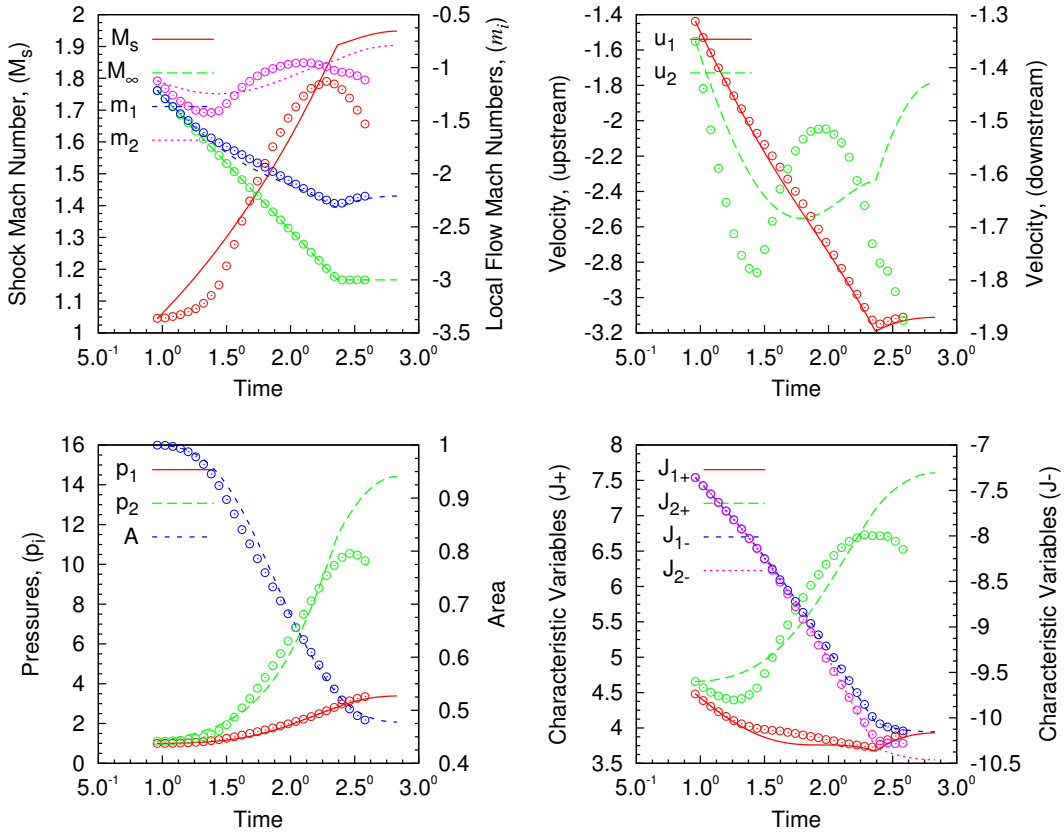

Figure H.3: Case VII: Accelerative starting scenario. Intake starts. Comparison between modified CCW$^+$ ($f = 0$ in b_1 term) and the full solution of the quasi-one-dimensional governing equations obtained using Asterix. While CCW$^+$ is not singular and it is able to predict the correct net outcome for this case, the solution must still be considered poor (or fair at best) in terms of agreement with the more accurate result from Asterix.

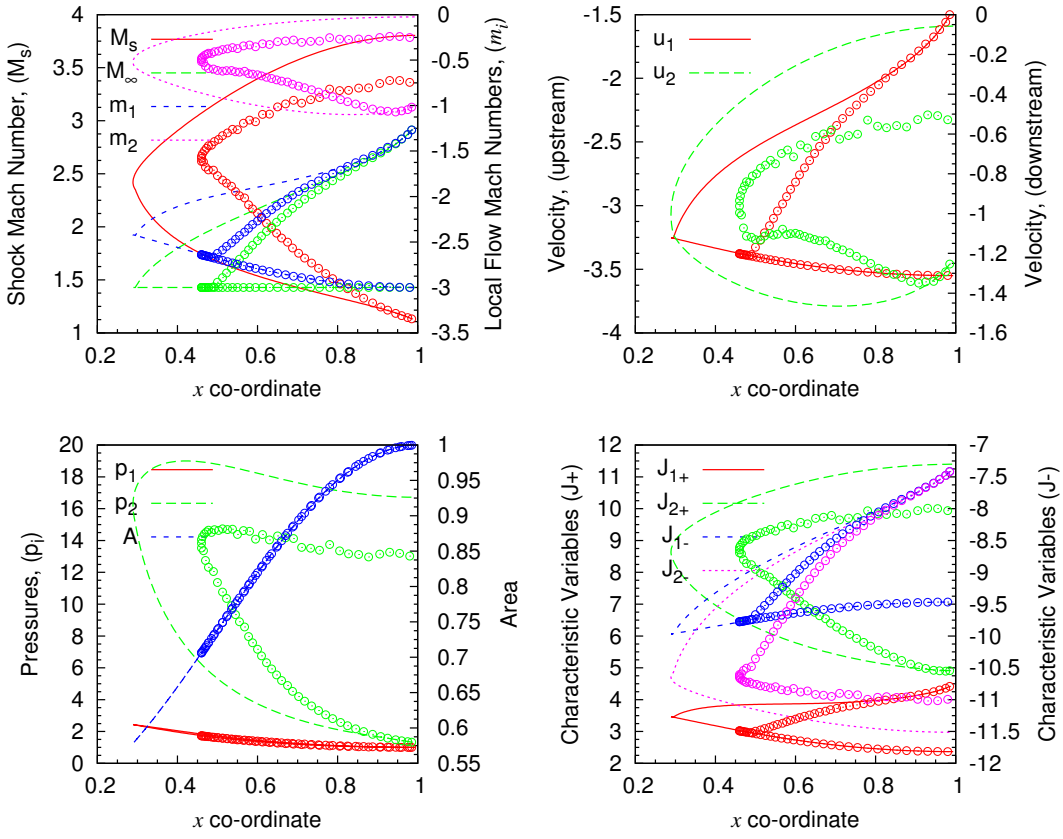

Figure H.4: Case VII: Accelerative starting scenario. Intake fails to start. Comparison between modified CCW$^+$ ($f = 0$ in b_1 term) and the full solution of the quasi-one-dimensional governing equations obtained using Asterix. While CCW$^+$ is not singular and it is able to predict the correct net outcome for this case, the solution must still be considered poor (or fair at best) in terms of agreement with the more accurate result from Asterix.

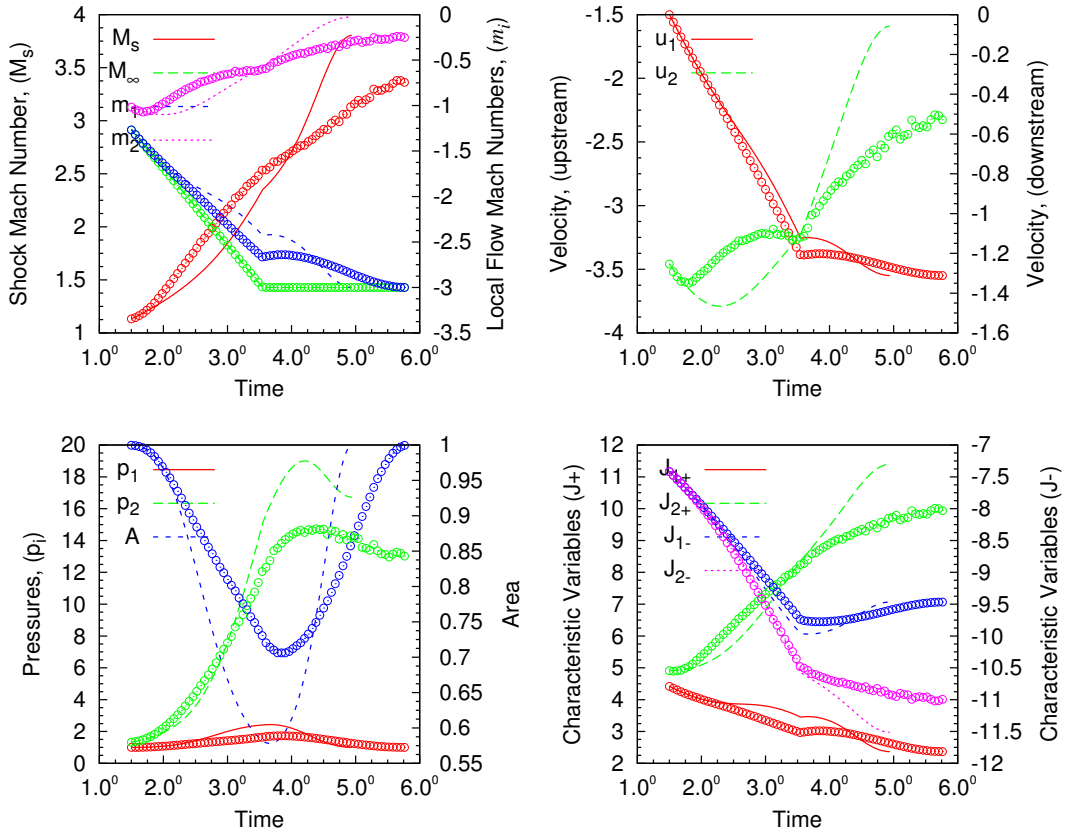

Figure H.5: Case VII: Accelerative starting scenario. Intake fails to start. Comparison between modified CCW$^+$ ($f = 0$ in b_1 term) and the full solution of the quasi-one-dimensional governing equations obtained using Asterix. While CCW$^+$ is not singular and it is able to predict the correct net outcome for this case, the solution must still be considered poor (or fair at best) in terms of agreement with the more accurate result from Asterix.

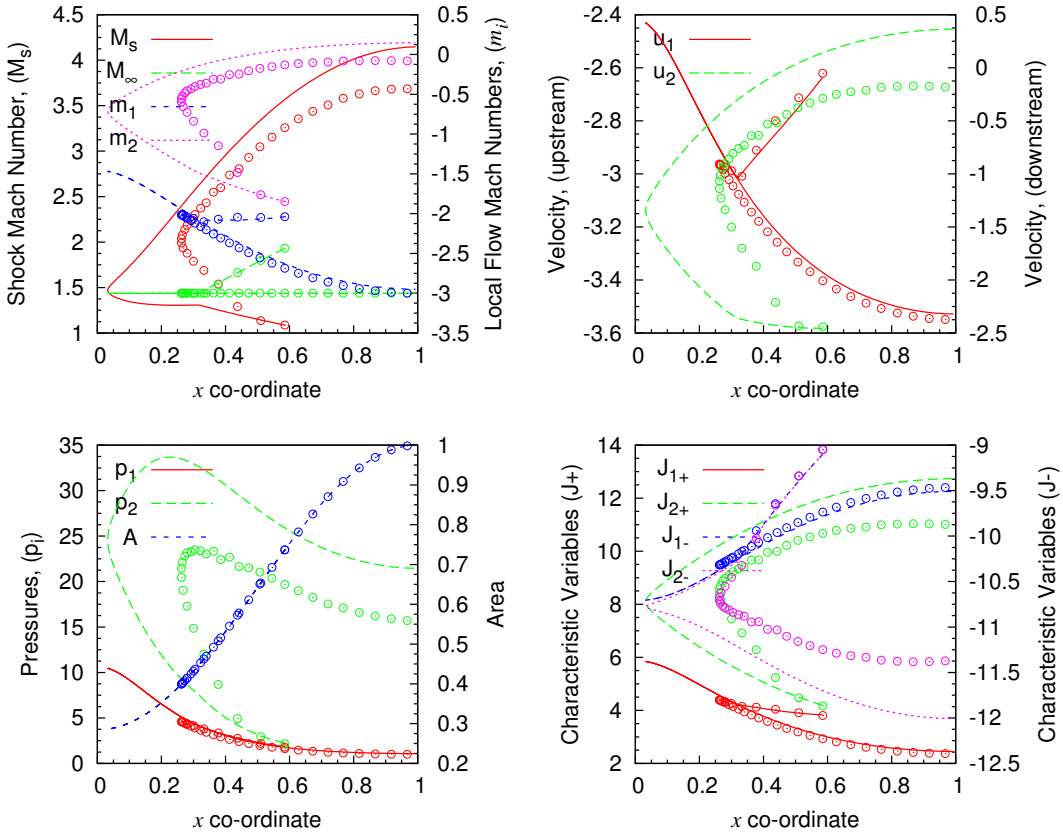

Figure H.6: Case VII: Accelerative starting scenario ($M_D = 3$, $IoS = 0.1$). Intake fails to start ($f = -3$). Comparison between modified CCW$^+$ ($f = 0$ in b_1 term) and the full solution of the quasi-one-dimensional governing equations obtained using Asterix. CCW$^+$ is not singular and it is able to predict the correct net outcome for this case. Similar scenario run for $f = -3.5$ shows both CCW$^+$ and Asterix predict started intake. While the net outcome is predicted correctly, the solution details are not in good agreement for that case.

Appendix I

Forms of the Euler Equations

I.1 Notation

For convenience, the useful forms of the Euler equations are compiled here from various standard reference texts, including[2,68,104,134,137]; the various forms have been transformed to use a consistent notation and it is hoped that this will save repeated labour.

I.1.1 Physical Variables

x–spatial coordinate; t–temporal coordinate; p–static pressure; ρ–static density; T–static temp; e–specific energy (sum of internal and kinetic parts); c–speed of sound; R–specific gas constant (286.9 J/kg K for air); c_v and c_p are specific heat at constant volume and at constant pressure, respectively; γ–adiabatic constant (1.4 for air); s–specific entropy; $A = A(x)$–channel area; f specific force; h–specific enthalpy; u–fluid velocity, relative to the channel; u_s–shock wave velocity, relative to the channel; M_s–Shock wave Mach number; m_1–Mach number upstream of a wave

(signed quantity); m_2–Mach number downstream of a wave (signed quantity).

I.1.2 Partial Differentials

The following notation appears commonly in the literature. Subscripts are preferred in this work for economy of writing, except where confusion may arise (*e.g.*, in the context where A_t is typically used to denote throat area, either $(A)_t$ or $\partial_t A$ is the preferred choice).

$$()_t \equiv \partial_t() \equiv \frac{\partial}{\partial t}() \tag{I.1}$$

$$()_x \equiv \partial_x() \equiv \frac{\partial}{\partial x}() \tag{I.2}$$

I.1.3 Useful Linear Operators

The following differential operators are helpful in transforming between the various forms while simultaneously maintaining consistent notation among the set of equations.

$$\mathbf{D}\,() \equiv ()_t + u\,()_x \tag{I.3}$$

$$\mathbf{D}_+\,() \equiv ()_t + (u+c)\,()_x \tag{I.4}$$

$$= \mathbf{D}\,() + c\,()_x \tag{I.5}$$

$$\mathbf{D}_-\,() \equiv ()_t + (u-c)\,()_x \tag{I.6}$$

$$= \mathbf{D}\,() - c\,()_x \tag{I.7}$$

$$\mathbf{D}\,() = \frac{\mathbf{D}_+\,() + \mathbf{D}_-\,()}{2} \tag{I.8}$$

$$()_x = \frac{\mathbf{D}_+\,() - \mathbf{D}_-\,()}{2c} \tag{I.9}$$

$$\mathbf{D}_\sigma\,() \equiv ()_t + u_s\,()_x \tag{I.10}$$

$$= ()_t + \frac{u_s}{2c}(\mathbf{D}_+\,() - \mathbf{D}_-\,()) \tag{I.11}$$

$$= \mathbf{D}\,() + (u_s - u)\,()_x \tag{I.12}$$

$$= \mathbf{D}_\pm\,() + (u_s - (u \pm c))\,()_x \tag{I.13}$$

$$= \frac{u_s - (u-c)}{2c}\mathbf{D}_+\,() - \frac{u_s - (u+c)}{2c}\mathbf{D}_-\,() \tag{I.14}$$

Lastly, $[()]_a^b$ is used for jump conditions from a to b, *e.g.*, across a shock wave.

I.2 Weak/Integral Form

The integral form of the conservation laws can be found in many standard reference texts, including[137].

$$\frac{\partial}{\partial t}\int_\Omega U\,\mathrm{d}\Omega + \oint_{\mathrm{d}\Omega} \vec{F}\cdot\mathrm{d}\vec{n} = \int_\Omega Q\,\mathrm{d}\Omega \tag{I.15}$$

$$U = \begin{bmatrix} \rho \\ \rho\vec{u} \\ \rho e \end{bmatrix},\ \vec{F} = U\vec{u} + p\begin{bmatrix} 0 \\ \overline{I} \\ \vec{u} \end{bmatrix},\ Q = \begin{bmatrix} 0 \\ \rho\vec{f} \\ \rho\vec{f}\cdot\vec{u} \end{bmatrix}, \tag{I.16}$$

where the conserved quantities are in U and their fluxes in $\vec{F}$, directed outward along the normal $\vec{n}$ at the bounding surface of the control volume Ω. $\overline{I}$ is the identity matrix, of rank k in k-dimensional space.

I.3 Strong/Differential Form

The differential form of the conservation laws can be found in many standard reference texts, including[137].

$$(\rho A)_t + (\rho u A)_x = 0 \tag{I.17}$$

$$(\rho u A)_t + \left(\rho u^2 A + pA\right)_x = pA_x + \rho A f \tag{I.18}$$

$$(\rho e A)_t + ((\rho e + p) u A)_x = \rho A u f \tag{I.19}$$

I.4 Thermodynamic Relations

The following formulae are very useful in transforming the governing equations into suitable forms; these can be found in many standard references, including[104].

$$p = \rho R T \tag{I.20}$$

$$= \rho(\gamma - 1)(e - u^2/2) \tag{I.21}$$

$$c^2 = \left|\frac{\partial p}{\partial \rho}\right|_s \tag{I.22}$$

$$= \gamma p/\rho \tag{I.23}$$

$$= \gamma RT \tag{I.24}$$

$$= \gamma(\gamma - 1)(e - u^2/2) \tag{I.25}$$

$$\frac{1}{\rho} = \left|\frac{\partial h}{\partial p}\right|_s \tag{I.26}$$

$$T = \frac{c^2}{\gamma R} \tag{I.27}$$

$$= \frac{h}{C_p} \tag{I.28}$$

$$\gamma = c_p/c_v \tag{I.29}$$

$$R = c_p - c_v \tag{I.30}$$

$$c_p = \frac{\gamma R}{\gamma - 1} \tag{I.31}$$

$$c_v = \frac{R}{\gamma - 1} \tag{I.32}$$

$$h = c_p T \tag{I.33}$$

$$= e - u^2/2 + p/\rho \tag{I.34}$$

$$e = c_v T + u^2/2 \tag{I.35}$$
$$= \frac{1}{\gamma - 1}\frac{p}{\rho} + u^2/2 \tag{I.36}$$

$$s - s_{\text{ref}} = c_p \ln T/T_{\text{ref}} - R \ln p/p_{\text{ref}} \tag{I.37}$$
$$= c_v \ln T/T_{\text{ref}} - R \ln \rho/\rho_{\text{ref}} \tag{I.38}$$
$$= c_v \ln p/p_{\text{ref}} - c_p \ln \rho/\rho_{\text{ref}} \tag{I.39}$$
$$= c_v \ln \frac{p/p_{\text{ref}}}{(\rho/\rho_{\text{ref}})^\gamma} \tag{I.40}$$

$$\mathrm{d}\left(\ln p\right) = \frac{2\gamma}{\gamma - 1}\mathrm{d}\left(\ln c\right) - \frac{1}{R}\mathrm{d}\left(s\right) \tag{I.41}$$
$$\mathrm{d}\left(\ln \rho\right) = \frac{2}{\gamma - 1}\mathrm{d}\left(\ln c\right) - \frac{1}{R}\mathrm{d}\left(s\right) \tag{I.42}$$

$$T\mathrm{d}\left(s\right) = \mathrm{d}\left(h\right) - \frac{1}{\rho}\,\mathrm{d}\left(p\right) \tag{I.43}$$
$$= \mathrm{d}\left(e\right) - u\,\mathrm{d}\left(u\right) + p\,\mathrm{d}\left(1/\rho\right) \tag{I.44}$$
$$= \mathrm{d}\left(e\right) - u\,\mathrm{d}\left(u\right) - \frac{p}{\rho^2}\,\mathrm{d}\left(\rho\right) \tag{I.45}$$
$$= \mathrm{d}\left(e\right) - u\,\mathrm{d}\left(u\right) - \frac{c^2}{\gamma\rho}\,\mathrm{d}\left(\rho\right) \tag{I.46}$$

I.5 Substantial Derivatives

Eulerian derivatives for the common sets of variables useful in practical calculations are included in the following subsections. These can also be used to obtain the characteristic relations listed in the sections further below.

I.5.1 Set I: $\{\rho, u, e\}$

Simplified case for: $A = A(x)$, so that $\partial_t A = 0$, otherwise, replace uA_x/A with $\mathbf{D}(\ln A)$; for isentropic flow $\mathbf{D}(s) = 0$, the energy equation follows from (I.46); the flow need not be homentropic ($s_x \neq 0$).

$$\mathbf{D}(\rho) = -\rho(u_x + uA_x/A) \tag{I.47}$$

$$\mathbf{D}(u) = f - p_x/\rho \tag{I.48}$$

$$\mathbf{D}(e) = u\,\mathbf{D}(u) + \frac{p}{\rho^2}\,\mathbf{D}(\rho) \tag{I.49}$$

Replacing p_x in the momentum equation using (I.21),

$$\mathbf{D}(u) = f - (\gamma - 1)\left[(e - u^2/2)\rho_x/\rho + (e_x - uu_x)\right] \tag{I.50}$$

and substituting this result into the energy equation,

$$\mathbf{D}(e) = u(f - p_x/\rho) - (u_x + uA_x/A)p/\rho \tag{I.51}$$

$$= u\left[f - (\gamma - 1)\left\{(e - u^2/2)\,(\ln \rho uA)_x + (e_x - uu_x)\right\}\right] \tag{I.52}$$

I.5.2 Set II: $\{\rho, u, p\}$

Simplified case for: $A = A(x)$, so that $\partial_t A = 0$, otherwise, replace uA_x/A with $\mathbf{D}(\ln A)$; isentropic flow $\mathbf{D}(s) = 0$, need not be homentropic ($s_x \neq 0$).

$$\mathbf{D}(\rho) = -\rho(u_x + uA_x/A) \tag{I.53}$$

$$\mathbf{D}(u) = f - p_x/\rho \tag{I.54}$$

$$\mathbf{D}(p) = c^2\,\mathbf{D}(\rho) \tag{I.55}$$

$$= -\gamma p(u_x + uA_x/A) \tag{I.56}$$

$$= -\rho c^2(u_x + uA_x/A) \tag{I.57}$$

I.5.3 Set III: $\{u, c, s\}$

Simplified case for: $A = A(x)$, so that $\partial_t A = 0$, otherwise, replace uA_x/A with $\mathbf{D}(\ln A)$; isentropic flow $\mathbf{D}(s) = 0$, need not be homentropic ($s_x \neq 0$).

$$\mathbf{D}(u) = f - 2cc_x/(\gamma - 1) + c^2 s_x/\gamma R \tag{I.58}$$

$$\mathbf{D}(c) = \frac{\gamma}{2c}\left(\frac{\rho\mathbf{D}(p) - p\mathbf{D}(\rho)}{\rho^2}\right) \tag{I.59}$$

$$= -\frac{(\gamma - 1)c}{2}(u_x + uA_x/A) \tag{I.60}$$

$$\mathbf{D}(s) = 0 \tag{I.61}$$

I.5.4 Set IV: $\{\rho, u, h\}$

Simplified case for: $A = A(x)$, so that $\partial_t A = 0$, otherwise, replace uA_x/A with $\mathbf{D}(\ln A)$; isentropic flow $\mathbf{D}(s) = 0$, need not be homentropic ($s_x \neq 0$).

$$\mathbf{D}(\rho) = -\rho(u_x + uA_x/A) \tag{I.62}$$

$$\mathbf{D}(u) = f - p_x/\rho \tag{I.63}$$

$$\mathbf{D}(h) = \mathbf{D}(p)/\rho \tag{I.64}$$

$$= -(\gamma p/\rho)(u_x + uA_x/A) \tag{I.65}$$

$$= -c^2(u_x + uA_x/A) \tag{I.66}$$

I.6 Steady-State Differential Relations

Simplified case for: $A = A(x)$, so that $\partial_t A = 0$; steady-state $\partial_t\{\rho, u, p, h, s\} = 0$; for the steady case, $\mathbf{D}(s) = 0$ leads to homentropic flow ($s_x = 0$).

$$\frac{\rho_x}{\rho} + \frac{u_x}{u} + \frac{A_x}{A} = 0 \tag{I.67}$$

$$\frac{p_x}{\rho u^2} + \frac{u_x}{u} = \frac{f}{u^2} \tag{I.68}$$

$$h_x + \frac{1}{2}(u^2)_x = f \tag{I.69}$$

For the non-homogeneous case, $f \neq 0$, the above equations provide coupled differential relations for flow quantities in terms of the prescribed geometry. This is used in the derivation of formulae listed in Appendix F, where exact solutions are compared with Asterix.

For $f = 0$, the homogeneous form of the equations leads to the classical one-dimensional isentropic relations in integrated form, which provide closed form

solutions. For example the classical area-Mach number relation $M = M(A)$ is obtained directly from (F.6). With that result, the remaining relations can be integrated in closed form as $\rho = \rho(M, A)$, etc.

I.7 Steady-State Integrated Relations

The *local* ratio of static to total temperature, for adiabatic flow *in the absence of body forces* [see Eqs. (F.4) and (F.6)], is given in terms of local flow Mach number by[104] pp. 4, Eqs. 43–46:

$$\frac{T_i}{T_t} = f(\gamma, m_i) = \left(1 + \frac{\gamma - 1}{2} m_i^2\right)^{-1} \tag{I.70}$$

For speed of sound (in adiabatic flow):

$$\frac{c_i}{c_t} = \left(\frac{T_i}{T_t}\right)^{\frac{1}{2}} \tag{I.71}$$

Similarly, for pressure and density (in homentropic flow):

$$\frac{p_i}{p_t} = \left(\frac{T_i}{T_t}\right)^{\frac{\gamma}{\gamma-1}} \tag{I.72}$$

$$\frac{\rho_i}{\rho_t} = \left(\frac{T_i}{T_t}\right)^{\frac{1}{\gamma-1}} \tag{I.73}$$

Combined with continuity ($\rho_i m_i c_i A_i = const$), the sonic area-Mach number relation (in isentropic flow) is obtained as[104] pp. 6, Eq. 80:

$$\frac{A_s}{A_i} = m_i \left(\frac{T_i/T_t}{T_s/T_t}\right)^{\frac{1}{2}\frac{\gamma+1}{\gamma-1}}, \tag{I.74}$$

where, T_s is the sonic temperature evaluated with $m_i = m_{\text{sonic}} = 1$ in (I.70).

The above formulae are often used to relate two different states connected by an homentropic process. For example, $(A_1/A_\infty) = (A_1/A_s) \times (A_s/A_\infty)$:

$$\begin{aligned} \frac{A_1}{A_\infty} &= \frac{f(m_1)}{f(m_\infty)} \\ &= \frac{m_\infty}{m_1} \left(\frac{T_\infty/T_t}{T_1/T_t} \right)^{\frac{1}{2}\frac{\gamma+1}{\gamma-1}} . \end{aligned} \tag{I.75}$$

I.8 Common Characteristic Forms

The Euler equations are used in the CCW literature mostly in characteristic form. However, there is a great variety of notation, variables and assumptions among the cited literature. The most commonly used variables lead to the following sets.

I.8.1 Set I: $\{\rho, u, p\}$

For C_+ characteristic direction, replace $\pm$ with $+$. Similarly, for C_-, replace $\pm$ with $-$.

$$C_\pm : \qquad \mathbf{D}_\pm (p) \pm \sqrt{\gamma p \rho}\, \mathbf{D}_\pm (u) = -\frac{\gamma p u}{A} A_x \pm \sqrt{\gamma p \rho} f \tag{I.76}$$

$$C_0 : \qquad \mathbf{D} (p) - \frac{\gamma p}{\rho} \mathbf{D} (\rho) = 0 \tag{I.77}$$

Dividing by ρc^2, and bringing area term on the left hand side, it gives:

$$C_\pm : \qquad \frac{1}{c} \mathbf{D}_\pm (u) \pm \frac{1}{\gamma p} \mathbf{D}_\pm (p) \pm \frac{m}{m \pm 1} \frac{\mathbf{D}_\pm (A)}{A} = \frac{f}{c} \tag{I.78}$$

$$C_0 : \qquad \mathbf{D} (p) - c^2 \mathbf{D} (\rho) = 0 \tag{I.79}$$

where area differential is to be evaluated using $\mathbf{D}_{\pm}(A) = (u \pm c)\partial_x(A)$.

I.8.2 Set II: $\{\rho, c, u, p\}$

The two equations above (I.76) commonly appear in the shock dynamics literature, where they are used as a starting point for establishing the characteristic rule (*i.e.*, direct application of the following equations is made in direction of the shock wave)[122] Ch. 8,[123] Ch. 6:

$$C_{\pm}: \qquad \mathbf{D}_{\pm}(u) \pm \frac{1}{\rho c}\mathbf{D}_{\pm}(p) \pm \frac{cu}{u \pm c}\mathbf{D}_{\pm}(\ln A) = f \tag{I.80}$$

$$C_0: \qquad \mathbf{D}(p) - c^2\,\mathbf{D}(\rho) = 0 \tag{I.81}$$

Note, the above form of the equations is not recommended for numerical calculations. Strictly speaking, (I.80) is incorrect because the area term is differentiated without an important caveat. The transformation made to obtain this form is physically invalid when $\mathbf{D}_{\pm}(\ln A) = 0$, or $u \pm c = 0$, *cf.*, (I.88).

I.8.3 Set III: $\{J_{\pm}, s\}$

Perhaps the most aesthetically pleasing form is that in which the left hand side bears the closest resemblance to Riemann's original work[109–111]. In any case, herein it is the mathematically preferred form.

$$C_{\pm}: \quad \mathbf{D}_{\pm}(J_{\pm}) = -\left(\pm\frac{cu}{A}A_x\right) + \frac{c^2}{\gamma R}s_x + f \tag{I.82}$$

$$= -\left(\pm\frac{\gamma-1}{8}\left[J^2\right]_-^+\frac{A_x}{A}\right) + \left(\frac{\gamma-1}{4}\left[J\right]_-^+\right)^2\frac{1}{\gamma R}s_x + f \tag{I.83}$$

$$C_0: \qquad \mathbf{D}(s) = 0 \tag{I.84}$$

The above relations determine how the characteristic variables (or Riemann's generalized non-invariants) must evolve in the presence of non-uniformities; here, the non-homogeneities include: (i) geometrical effects ($A_x \neq 0$); (ii) non-homentropic effects ($s_x \neq 0$); and (iii) forces accelerating the fluid. Note that the first two equation give time rate of change of velocity (or acceleration or force per unit mass) experienced by the fluid along special trajectories. The special trajectories are the characteristic directions along which wave-like disturbances propagate; this is the hyperbolic nature of the Euler equations.

$$J_{\pm} \equiv u \pm \frac{2}{\gamma - 1} c \tag{I.85}$$

Note, the first two equations (I.82) may be transformed using the operators of §I.1.3, to the following equivalent forms (ignoring, for a moment, the difference stemming from a more general provision for $\partial_t A$):

$$C_{\pm}: \quad \mathbf{D}_{\pm}(J_{\pm}) = -\left(\pm \frac{cu}{A} A_x\right) \pm \frac{c}{\gamma R} \mathbf{D}_{\pm}(s) + f \tag{I.86}$$

$$= - \pm c\, \mathbf{D}(\ln A) \pm \frac{c}{\gamma R} \mathbf{D}_{\pm}(s) + f \tag{I.87}$$

$$= - \pm c\, (\mathbf{D}_{\pm}(\ln A) - \pm c (\ln A)_x) \pm \frac{c}{\gamma R} \mathbf{D}_{\pm}(s) + f \tag{I.88}$$

For the case of a vertical $C_{\pm}$ curve in the wave diagram, *i.e.*, $u \pm c = 0$, Eqs. I.88 and I.80 do not agree. The former recovers the correct expression of Eqs. I.82 (let $\partial_t A = 0$), while the later does not. *Practical use of that expression, in calculations with non-trivial flow ahead of the shock wave, may lead at best to loss in precision, and at worst to a division by zero.*

The incorrect form has lead some researchers to incorrectly conclude the behaviour of these equations under certain circumstances as describing the familiar flow choking phenomenon. The common interpretation, surrounding the singu-

larity, attempts to use (improperly) a steady-state physical concept in a truly unsteady situation.

I.9 Rankine-Hugoniot Relations

Useful jump relations from [104] are stated below for convenience, which appear in various forms in the CCW literature. These are valid for both left- and right-facing shock waves.

Note: simplified case of perfect gas; $\pm$ signs correspond to right- and left-facing waves, respectively; $\nu_i \equiv u_s - u_i$; The basic conditions are: $[\rho\nu]_1^2 = 0$, $[\rho\nu^2 + p]_1^2 = 0$, and $[h + \nu^2/2]_1^2 = 0$; $M_s \equiv \pm(u_s - u_1)/c_1 > 1$.

The pressure ratio across a shock wave is given by [104]:

$$\xi \equiv \frac{p_2}{p_1} = f(g, M_s) \tag{I.89}$$

$$= 1 + \frac{2\gamma}{\gamma+1}(M_s^2 - 1) \tag{I.90}$$

$$\frac{\partial}{\partial M_s}\left(\frac{p_2}{p_1}\right) = \frac{4\gamma M_s}{\gamma+1} \tag{I.91}$$

The density ratio across a shock wave is given by [104]:

$$\frac{\rho_1}{\rho_2} = f(g, M_s) \tag{I.92}$$

$$= \frac{\gamma-1}{\gamma+1} + \frac{2}{\gamma+1}\frac{1}{M_s^2} \tag{I.93}$$

$$\frac{\partial}{\partial M_s}\left(\frac{\rho_1}{\rho_2}\right) = -\frac{4}{\gamma+1}\frac{1}{M_s^3} \tag{I.94}$$

The ratio of speeds of sound across a shock wave is given by:

$$\left(\frac{c_2}{c_1}\right)^2 = f(\gamma, M_s) \tag{I.95}$$

$$= \frac{p_2}{p_1}\frac{\rho_1}{\rho_2} \tag{I.96}$$

$$\frac{\partial}{\partial M_s}\left(\frac{c_2}{c_1}\right) = \frac{2}{\gamma+1}\left(\frac{c_2}{c_1}\right)^{-1}\left(\gamma M_s \frac{\rho_1}{\rho_2} - \frac{1}{M_s^3}\frac{p_2}{p_1}\right) \tag{I.97}$$

In terms of Riemann variables for the speeds of sound across the shock, the following relations are useful:

$$c_1 = \frac{\gamma-1}{4}\left[J_1\right]_-^+ \tag{I.98}$$

$$c_2 = \frac{\gamma-1}{4}\left[J_2\right]_-^+ \tag{I.99}$$

$$\frac{c_2}{c_1} = \frac{\left[J_2\right]_-^+}{\left[J_1\right]_-^+} \tag{I.100}$$

The ratio of total pressures is a function of γ and M_s only, and is used further below in the computation of entropy jump across the wave[104]:

$$\ln\left(\frac{p_{t_1}}{p_{t_2}}\right) = f(\gamma, M_s) \tag{I.101}$$

$$= \frac{1}{\gamma-1}\left[\ln\left(\frac{p_2}{p_1}\right) + \gamma \ln\left(\frac{\rho_1}{\rho_2}\right)\right] \tag{I.102}$$

For the change in velocities across a shock wave, the following relations are

useful:

$$u_1 = \frac{1}{2}\left(J_{1^+} + J_{1^-}\right) \tag{I.103}$$

$$u_2 = \frac{1}{2}\left(J_{2^+} + J_{2^-}\right) \tag{I.104}$$

$$[u]_1^2 = \frac{1}{2}([J_+]_1^2 + [J_-]_1^2) \tag{I.105}$$

$$\frac{u_2}{u_1} = \frac{J_{2^+} + J_{2^-}}{J_{1^+} + J_{1^-}} \tag{I.106}$$

$$[u]_1^2 = f(\gamma, c_1, M_s) \tag{I.107}$$

$$= \pm\frac{2c_1}{\gamma+1}\left(M_s - \frac{1}{M_s}\right) \tag{I.108}$$

The change in entropy is given by[104]:

$$[s]_1^2 = f(\gamma, R, M_s) \tag{I.109}$$

$$= R\ln\left(\frac{p_{t_1}}{p_{t_2}}\right) \tag{I.110}$$

$$\frac{\partial}{\partial M_s}\left([s]_1^2\right) = \frac{4\gamma R}{\gamma^2-1}\left(M_s\left(\frac{p_2}{p_1}\right)^{-1} - \frac{1}{M_s^3}\left(\frac{\rho_1}{\rho_2}\right)^{-1}\right) \tag{I.111}$$

I.9.1 Shock Velocity & Mach Number Relations

Simplified case for perfect gas; $\pm$ signs correspond to *right-* and *left-facing* waves, respectively; $(\{p_2/p_1, \rho_2/\rho_1, c_2/c_1, \gamma, M_s\} \geq 1)$.

$$u_2 = u_1 \pm \frac{2c_1}{\gamma + 1}\left(M_s - \frac{1}{M_s}\right) \tag{I.112}$$

$$u_s = u_1 \pm M_s\, c_1 \tag{I.113}$$

$$m_1 = u_1/c_1 \tag{I.114}$$

$$m_2 = u_2/c_2 \tag{I.115}$$

$$M_s^2 = \frac{1}{2\gamma}\left[(\gamma + 1)\frac{p_2}{p_1} + (\gamma - 1)\right] \tag{I.116}$$

$$\mu \equiv \frac{u_s - u_2}{c_2} = \sqrt{\frac{(\gamma - 1)M_s^2 + 2}{2\gamma M_s^2 - (\gamma - 1)}} \tag{I.117}$$

N.B. By definition, for a *right-facing* wave, the flow enters the wave from the right side. Also note that a right-facing shock may move either to the left or to the right; *thus, the apparent direction of motion is independent of the facedness.* Additionally, two independent observers agree on the *facedness* if and only if they share a proper sense of direction, *e.g.*, if x is positive rightward or leftward for both. This is true, even when the wave may appear to move leftward relative to the first observer, and rightward relative to the second observer.